Addis Ababa University

College of Natural and Computational Sciences

School of Earth Science

Remote Sensing and Geoinformatics stream

M.Sc. thesis on

DETECTION OF GEOTHERMAL ANOMALIES USING LANDSAT 8 THERMAL INFRARED DATA IN TULU MOYE GEOTHERMAL PROSPECT, MAIN ETHIOPIA RIFT



By

Yosef Mengistu Darge

(GSR\1400/07)

A Thesis Submitted to the School of Graduate Studies of Addis Ababa University Presented in Partial Fulfilment of the Requirements for the Degree of Masters of Science in Remote Sensing and Geoinformatics.

Addis Ababa University

June 2016



Addis Ababa University

College of Natural and Computational Sciences

School of Earth Sciences

Remote Sensing and Geoinformatics Stream

M.Sc. thesis on:

DETECTION OF GEOTHERMAL ANOMALIES USING LANDSAT 8 THERMAL INFRARED DATA IN TULU MOYE GEOTHERMAL PROSPECT, MAIN ETHIOPIA RIFT

This is to certify that this thesis prepared by **Yosef Mengistu Darge** entitled: " ***DETECTION OF GEOTHERMAL ANOMALIES USING LANDSAT 8 THERMAL INFRARED DATA IN TULU MOYE GEOTHERMAL PROSPECT, MAIN ETHIOPIA RIFT*** " and submitted in partial fulfillment of the requirements for the Degree of Master of Science (Remote Sensing and Geoinformatics) compiles with the regulations of the University and meets the accepted standards with respect to originality and quality.

Approved by board of examiners:

Dr. Seifu Kebede	_____	_____
Chairman	Signature	Date
Dr. Binyam Tesfaw	_____	_____
Advisor	Signature	Date
Dr. Ameha Atnafu	_____	_____
Co-advisor	Signature	Date
Dr. K.V. Suryabahagvan	_____	_____
Examiner	Signature	Date
Prof. Gezahegn Yirgu	_____	_____
Examiner	Signature	Date

Acknowledgements

I would like to take this ample opportunity to acknowledge the personnel and organizations that directly or indirectly involve and support me to accomplish this research.

First, I would like to express my sincere gratitude and acknowledgement with due respect to my advisor Dr. Benyam Tesfaw and Dr. Ameha Atinafu for their guidance and supports. This research would not been possible to go in right direction and may not have the look that it has right now without their comments, feedbacks and suggestions.

I owe a great deal to colleagues, students friends and members of my family who have helped me to successfully complete the research work, and who, through their own research, comments and questions have encouraged, supported and enlightened me. Many thanks goes to Information Network Security Agency (INSA), Geological Survey of Ethiopia (GSE) and National Meteorological Agency (NMA) for giving me all the necessary data for my research work. I also thank INSA workers for their help and endless comments on my thesis. It would not been completed the way it has to be without their technical support.

Last but not least, thank you to all School of Earth Science instructors and lab assistants' for giving me the knowledge that I cannot find anywhere else within two years of my stay at Addis Ababa University (AAU). It enlightened me with great knowledge of Earth Science and showed me what a great place this science have in solving problems of world and our country Ethiopia with its capabilities and techniques. This research is a complete combination of almost every lesson I have learnt at this School.

Table of Contents

Acknowledgements i
Table of Contents ii
List of tables iv
List of Figures v
List of Acronyms vi
ABSTRACT vii
1. General Background 1
1.1 Introduction 1
1.2 Statement of the Problem 5
1.3 Objective of the Study 5
1.3.1 General Objective 5
1.3.2 Specific Objective 6
1.4 Research Questions 6
1.5 Significance of the Study 6
1.6 Scope of the study 7
2. Literature Review 8
2.1 Theoretical Background 8
2.1.1 The Earth and its Atmosphere 8
2.1.2 Active Geothermal Regions 9
2.1.3 Mechanism of Geothermal Anomaly 10
2.1.4 Tulu Moye Geothermal Prospect 11
2.1.5 Hydrothermal Geothermal Resource 13
2.1.6 Exploration Strategies and Techniques 14
2.1.7 Remote sensing 16
2.1.8 Remotely Sensed Thermal Infrared 18
2.2 Previous Work 21
3. Materials and Methods 29
3.1 Geographic Setting 29
3.1.1 Location of Study Area 29
3.1.2 General Geology of Ethiopian Rift 30
3.1.3 Geology of Study Area 31
3.1.4 Climate and Vegetation 36
3.1.5 Soil 37
3.1.6 Population 37
3.1.7 Physiography and Drainage 38

3.2 Materials....38
3.2.1 Primary Data Source....38
3.2.2 Secondary Data Source....39
3.3 Methods....40
3.3.1 Preprocessing....43
3.3.2 Retrieval of Normalized Difference Vegetation Index (NDVI)....45
3.3.3 Estimation of Fractional Vegetation Cover (FVC)....45
3.3.4 Estimation of Land Surface Emissivity (LSE)....46
3.3.5 Sensor Brightness Temperature....47
3.3.6 Land Surface Temperature Calculation....48
3.3.7 Geothermal Anomaly Detection....49
4. Results and Discussion....50
4.1 Radiometric Calibration....50
4.2 Atmospheric Correction....53
4.3 Normalized Difference Vegetation Index (NDVI)....56
4.4 Fractional Vegetation Cover (FVC)....58
4.5 Land Surface Emissivity (LSE)....60
4.6 Sensor Brightness Temperature....61
4.7 Land Surface Temperature (LST)....62
4.8 Land Surface Temperature Anomaly Detection....63
4.9 Validation of Land Surface Temperature Anomalies....64
4.10 False Geothermal Anomalies Detection....67
4.11 Heat Source Analysis....68
4.12 Geological Analysis....68
4.13 Identification of Geothermal Areas....71
4.14 Validation....71
4.15 Discussion....72
5. Conclusion and Recommendations....77
5.1 Conclusion....77
5.2 Recommendation....78
Reference....79
Appendices....85

List of Tables

Table 1: Landsat 8 characteristics....17

Table 2: Principal applications of the Landsat 8 bands. Source: United State of Geological Survey (USGS). 18

Table 3: Types of materials and software used....39

Table 4: LANDSAT 8 Radiance Scale Factors 44

Table 5: Emissivity value of vegetation and soil....47

Table 6: Thermal constant value of K1 and K2....48

Table 7: Split-Window Coefficient values. source: Skokovic et al., 2014....49

Table 8: 6S atmospheric correction coefficient 54

Table 9: NDVI histogram values of study area 57

Table 10: Cavity effect Value of band 10 and 11 59

Table 11: Statistical comparison between Landsat 8 and MODIS LST 65

List of Figures

Figure 1: Location of Geothermal Prospect areas in Ethiopia. Source: Geological Survey Ethiopia (GSE).....3
Figure 2: Schematic model of a hydrothermal geothermal system, after White, D.E., 1973.....14
Figure 3: The Electromagnetic spectrum after Thomas M. Lillesand and Ralph W.Kiefer, 1994.16
Figure 4: The thermal infrared wavelength domain, typical absorption bands induced by gasses and water, and atmospheric transmittance (atmospheric windows) (Figure courtesy of Rudolf)...19
Figure 5: Blackbody radiation curves at different selected temperatures, as derived from Eq.1...20
Figure 6: Location map of the study area. 29
Figure 7: Geological map of Study Area. Extracted from Geological maps of Tulu Moye in scale 1: 50,000 and 1:20,000. 33
Figure 8: Mean monthly rainfall of metrological stations in 2014.....36
Figure 9: Soil map of Study Area. Source: Food and Agriculture Organization (FAO).....37
Figure 10: Methodology flow chart.....42
Figure 11: Radiance map of study area for band 4(A) and 5 (B) 51
Figure 12: Radiance map of study area for band 10 (A) and 11 (B). 53
Figure 13: Reflectance map of study area for Band 4 (A) and 5 (A). 56
Figure 14: NDVI map of study area. 58
Figure 15: The percentage of the vertical projection of vegetation canopy map of study area.....59
Figure 16: Mean of Land surface emissivity map of study area. 60
Figure 17: Top of Atmosphere Brightness Temperature map for band 10 (A) and 11 (B).....62
Figure 18: Mean of Land Surface Temperature map of Study area. 63
Figure 19: LST Anomaly map of Study area. 64
Figure 20: Resampled Landsat 8 LST (A) and Original MODIS (MOD11A1) (B) of 1 km spatial resolution. 66
Figure 21: Artificial thermal influences map of Study Area. 67
Figure 22: Three dimensional topographic image of study area marked with nine thermal anomalous areas.....70
Figure 23: Geothermal anomaly image of study area.....70
Figure 24: Validation map between known hydrothermal manifestation and LST Anomalies. 72
Figure 25: Six known identified geothermal area 74
Figure 26: Hydrothermal manifestation map.....75

List of Acronyms

6S	Second Simulation of the Satellite signal in the Solar Spectrum
CSA	Central Statistics Agency
DEM	Digital Elevation Model
EARS	East African Rift System
EMR	Electromagnetic radiation
ETM+	Enhanced Thematic Mapper
FAO	Food and Agriculture Organization
FLIR	Forward Looking Infrared
FVC	Fractional Vegetation Cover
GIS	Geographical Information System
GPS	Global Positioning System
GTP	Growth and Transformation Plan
GSE	Geological Survey of Ethiopia
LSE	Land Surface Emissivity
LST	Land Surface Temperature
LUT	Look-Up-Table
MER	Main Ethiopian Rift
MODIS	Moderate Resolution Imaging Spectroradiometer
NDVI	Normalized Difference Vegetation Index
NMA	National Meteorological Agency
OLI	Operational Land Imager
RMSE	Root Mean Square Error
RS	Remote Sensing
SC	Single Channel
SDZFZ	Silti Debre Zeit Fault Zones
SRTM	Shuttle Radar Topographic Mission
SW	Split Window
TIR	Thermal Infrared
TM	Thematic Mapper
TOA	Top of the Atmospheric
USGS	United State Geological Survey

ABSTRACT

Despite there is large geothermal potential along Ethiopian Rift Valley in the country, the risky nature of the business was impeding development of the geothermal power industry till now. To find all possible geothermal target location using ground survey is very difficult. So that, it needs cost effective method for exploration strategies and techniques of detection geothermal area. Thermal infrared (TIR) remote sensing is an important and easy technique in the exploration of geothermal resources. In this study, a geothermal survey is conducted in Tulu Moye area of Oromia region, in Ethiopia using TIR data from Landsat-8 Sensor. The data is identified as path 168 and row 054 from United State of Geological Survey (USGS) website. It was obtained on October 17, 2014. Based on radiometric calibration, atmospheric correction with 6S model and land surface emissivity calculation with NDVI threshold method, a simple but efficient split window (SW) algorithm with acceptable precision is applied to retrieve the Land Surface Temperature (LST) of study area. LST result shown that it varied from 292.23 to 315.88 Degree Kelvin (^{o}K). The highest LST were traced in barren lands and wastelands of study area. LST comparison between MODIS and Landsat 8 has a maximum difference of 1.47 ^{o}K. The LST anomalous areas with temperature about 3–9 ^{o}K higher than background area are discovered. Six geothermal areas are identified and three promising areas are found to the west of Tulu Moye area and warrant further ground exploration with the discussion of geothermal mechanism and the further analysis of regional geologic structure. Auxiliary data and analysis tools were used to exclude the non-geothermal influences. The research reveals that the distribution of geothermal areas is consistent with the fault development in study area. Magmatism contributes abundant thermal source to study area and the faults provide thermal channels for heat transfer from interior earth to land surface and facilitate the present of geothermal anomalies. Finally, TIR remote sensing is a cost-effective technique to detect LST anomalies. Combining TIR remote sensing with geological analysis and the understanding of geothermal mechanism is an accurate and efficient approach to geothermal area detection

Key words: Geothermal Energy; LST Anomalies; Heat Source; Fault; Thermal data.

1. General Background

1.1 Introduction

Geothermal energy is one of the renewable energy that can be used as alternatives to increasingly scarce fossil energy, which is commonly used by people to support their life, is exhaustible (Siahaan et al., 2011). On Earth, human activities are changing the natural greenhouse. Over the last century the burning of fossil fuels like coal and oil has increased the concentration of atmospheric carbon dioxide (CO_2). This happens because the coal or oil burning process combines carbon with oxygen in the air to make CO_2. To a lesser extent, the clearing of land for agriculture, industry, and other human activities have increased concentrations of greenhouse gases. The consequences of changing the natural atmospheric greenhouse are difficult to predict, but certain effects seem likely: On average, Earth will become warmer. Some regions may welcome warmer temperatures, but others may not. Warmer conditions will probably lead to more evaporation and precipitation overall, but individual regions will vary, some becoming wetter and others dryer. As a result, it will warm the oceans and partially melt glaciers and other ice, increasing sea level and affect the makeup of agricultural sector. Which is a threat throughout the world. The existence of heat trapping greenhouse affects the Earth's atmosphere. To minimize the effect, varies nations have developing renewable energy source with low carbon emissions. Its exploration and development currently new interest as nation to lessen its dependence on foreign oil sources. Those alternatives energy resources are clean geothermal, hydroelectric, wind, and solar energy as well.

Geothermal is the energy stored underground as hot water/steam (Ronald, 2005). Its renewable and environmentally benign nature along with its multipurpose applications makes it one of the favored energy resources in modern energy. According to Siahaan et al., (2011), this clean energy is considered more secure because it does not require a big space for the purposes of exploration and exploitation. Besides Geothermal energy produces vapor which can be mixed as well to the air. This energy occur in regions of anomalously high crustal heat flow that may be related to the presence of young igneous bodies or hot rocks located deeper in the crust (Ronald, 2005). This elevated geothermal heat is normally transferred to the surface by the convection of ground waters that forms hydrothermal systems: surface waters circulate to depth where they are heated and rise to the surface via a subterranean ‘plumbing system’ of closely spaced fractures or other zones of permeable rock. If rising hot waters reach the surface then characteristic geothermal features such as hot springs, fumaroles, geysers, and mud pots may form.

Ethiopia started a long-term geothermal exploration undertaking in 1969. Over the years a good inventory of the possible resource areas has been built up and a number of the more important sites have been explored in the Ethiopian Rift Valley (Figure 1). Of these areas, about sixteen are judged to have potential for high temperature steam suited to electricity generation. The geothermal potential in Ethiopia for power generation exceeds 5,000 Mega Watt (MW) (MoWE, 2011).

Three major geothermal prospect areas were distinguished in Ethiopia Rift: Lake District in the Ethiopian Rift, Tendaho and Dalol area in the Danakil depression (UNDP, 1973). Exploration work peaked during the early to mid-1980s when exploration drilling was carried out at the Aluto-Langano geothermal field (Lakes District). In the Aluto-Langano geothermal field, varies deep exploratory wells were drilled, and four are found to be potentially productive with a maximum geothermal reservoir temperature of about 350 ºC (Degree Centigrade) (Peter and Teklemariam, 2010). The 7.2 MW net capacity pilot plant installed at the Aluto- Langano has faced operational difficulties that are essentially due the technical problems and lack of the appropriate field and plant management skills. The rehabilitation is complete and the plant currently generates 5 MW.

Other Geothermal resource identified by earlier exploration in Dubti area, Tendaho. Its detailed geoscientific studies (geology, geochemistry and geophysics) followed by the drilling of temperature gradient wells were carried out in different years. Currently, well testing and reservoir engineering studies and geochemical monitoring of the shallow geothermal reservoir is in progress towards the objective of carrying out the feasibility study followed by installation of small scale pilot power plant using the existing shallow productive wells (Peter and Teklemariam, 2010).

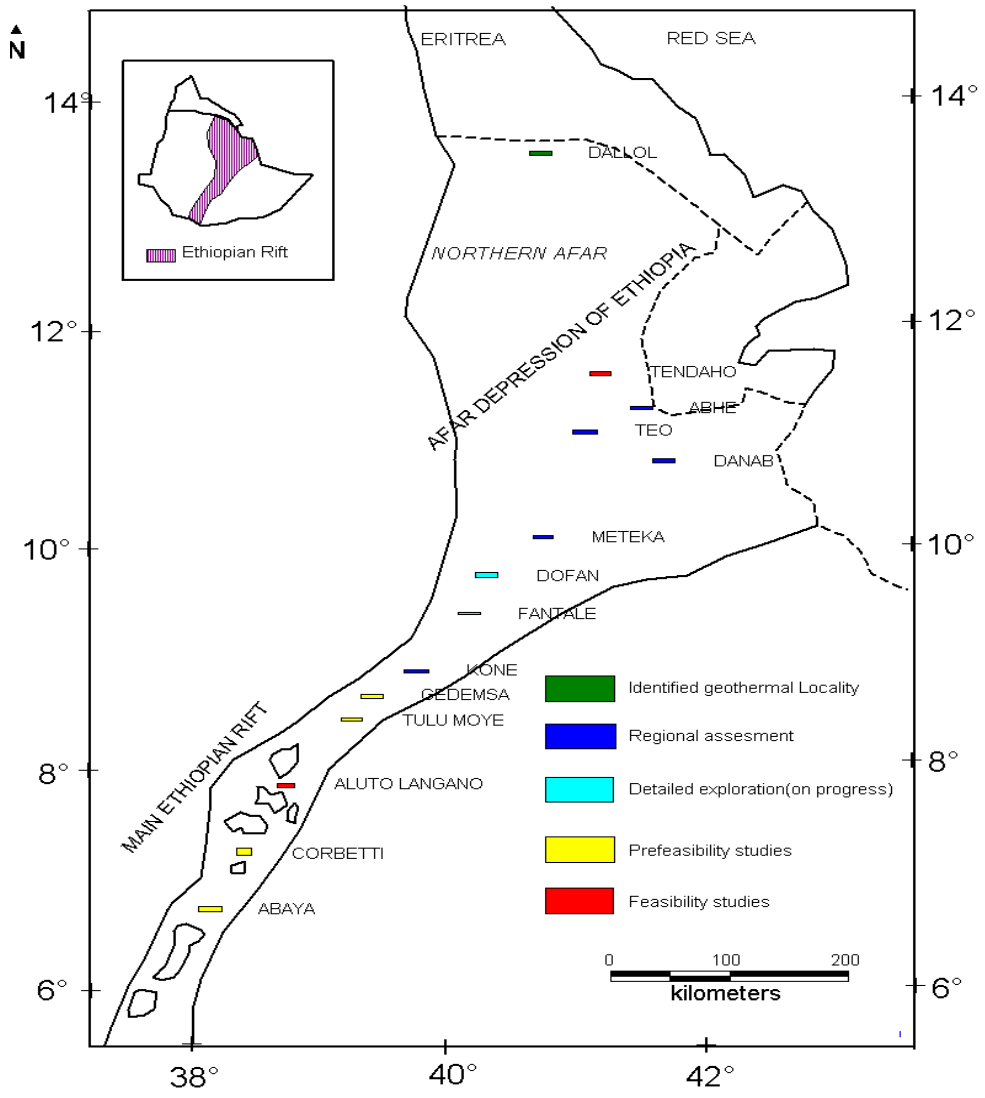

Figure 1: Location of Geothermal Prospect areas in Ethiopia. Source: Geological Survey Ethiopia (GSE)

Other geothermal prospect areas in the Ethiopian Rift Valley are at various stages of exploration that vary from reconnaissance to detailed geoscientific studies including drilling of temperature gradient (TG) wells. These include:

i. Tulu-Moye and Corbetti (Detailed geoscientific including drilling of TG wells)
ii. Abaya, Dofan and Fantale (Detailed geoscientific studies)
iii. Teo, Danab, Kone and others (Reconnaissance investigations)

Tulu Moye is one of the lakes district geothermal prospect, which is located about 200 km south east of part of Addis Ababa, the Main Ethiopia Rift (MER). The main hydrothermal manifestations are weak fumaroles, active steaming grounds and altered grounds. In this area, exploration and

geoscientific study have been done several times. It confirmed the existence of potential geothermal reservoirs with high temperature. Now a days, the area has been given a priority for further geoscientific investigations like detailed surface hydrothermal alteration, geological mapping and geophysical investigations carried out.

This paper demonstrate the effectiveness of satellite remote sensing infrared data for detecting geothermal anomaly in Tulu Moye area. Thermal Infrared (TIR) remote sensing data is used to map and quantify temperature anomalies associated with surface geothermal features such as, fumaroles, and steaming ground, which comes from the subsurface of the area reach the ground by conduction and convection (Claudia and Stefan, 2013). In order to achieve the objective of the research different methodology and approaches are followed. The methodology would be using of Landsat 8 satellite data which have carries two-sensor payload: the Operational Land Imager (OLI) and the Thermal Infrared Sensor (TIRS), those are helps to detect potential geothermal area.

In the pre- processing operation, radiometric calibration is applied based on Landsat 8 data user handbook. Top of the Atmospheric (TOA) radiances were converted to TOA brightness temperatures using Planck's equation. Atmospheric correction using 6S (Second Simulation of the Satellite signal in the Solar Spectrum-Vector) model was applied to minimize the effect of gases, molecules and particles in the atmosphere. Land Surface Emissivity (LSE) was estimated using (Normalized Difference Vegetation Index) NDVI threshold method. LSE is important parameter to calculate LST (Land Surface Temperature). Finally, Split window algorithm was applied for LST extraction, which is helps to detect geothermal anomaly. Further detail interpretation used to exclude false anomaly form geothermal area with the help of geological structure, heat source analysis and thematic map, and then field verification have been applied.

Collection of review literature and organization of secondary data from all possible source. Conducted a reconnaissance field survey and consultation with local community living nearby study areas and the local leaders. These approached have been used as a cost-effective tool for geothermal exploration over large areas for further exploration using ground-based surveys (Claudia and Stefan, 2013).

1.2 Statement of the Problem

Ethiopia energy sector is dominated by traditional biomass fuel which is greater than 80% such as firewood, agricultural waste and animal dung. Modern energy demands are met mainly by hydro (3%) and petroleum (6%) that contributes to about 9% of the total energy supply (MoWE, 2011). Ethiopia, like other African nations, suffers from insufficient of energy source. This situation has created depletion forest resources of the country that cause land degradation and loss of agricultural soil fertility, and affect economic growth. Currently, government of Ethiopia is developing alternative energy source such as wind, solar and hydropower. Those are less expensive than geothermal energy, which is more costly. Despite the country's large potential along rift valley, however, the risky nature of the business was impeding development of the geothermal-power industry till now. So that, it needs cost effective method for exploration strategies and techniques of detection geothermal area.

Over the years study, an inventory of the possible resource areas within the Ethiopian Rift system are much larger number of reflected in surface hydrothermal manifestations. It covers an area of about 150,000 square kilometers (km^2) that is close to 12% of the total land area (MoWE, 2011). To find target location of all potential area in the nation, it needs further exploration using ground-based surveys. This work is very tough and technologically challenging, it takes time, money and large number of qualified geothermal expertise. Such kind of methods will be a bottleneck to going forward in geothermal energy development sector, poor country like Ethiopia, can hardly afford. Tulu Moye Geothermal prospect is covered 572 km^2 with difficult topography structure and lack of accessibility will be constraint to select all appropriate target location. Therefore, Landsat 8 TIR remote sensing data can acquired freely from United State Geological Survey (USGS). It provides a unique tool and easy approach for mapping the surface expressions of geothermal activity.

1.3 Objective of the Study

1.3.1 General Objective

The main objective of this research is to explore and select subsequent potential geothermal target area for further exploration in Tulu Moye using rapid and cost effective tools of Thermal Infrared (TIR) Remote Sensing Approach.

1.3.2 Specific Objective

- To retrieve actual Land Surface Reflectance using 6S model.
- Mapping of Normalized Difference Vegetation Index (NDVI)
- Estimation of Fraction Vegetation Coverage (FVC) using Landsat 8 imagery.
- To retrieve Land Surface Emissivity from Visible Near-Infrared (VNIR) data.
- To retrieve Land Surface Temperature from Landsat 8 thermal bands.
- Validation of the Landsat 8 LST by comparing it with the MODIS (Moderate Resolution Imaging Spectroradiometer) LST product.
- Interpretation and detection of geothermal surface temperature anomalies.

1.4 Research Questions

To reach the above objectives the following questions need to be answered

- How viable is the Landsat 8 TIRS Remote Sensing Approach for detecting potential geothermal area?
- What parameters are needed to retrieve LST and how can they be obtained?
- How to detect geothermal surface temperature anomalies present in the surface using TIR data?
- Are Landsat 8 LST retrieved correlated with MODIS LST product at 1km pixels resolution?

1.5 Significance of the Study

Ethiopia has embarked on a multi-billion dollar energy sector development programme to become one of Africa's major exporters of electricity. Country Growth and Transformation Plan (GTP) has ambitious goal to develop its geothermal energy resources to boost electricity supply to all Ethiopians and increasingly become a regional power hub. Now a days, governmental, international investor and private organization have also shown an interest in investing in geothermal power in different site along the rift valley to meet its expanding power generation ambitions.

The area along rift valley have been identified as potential geothermal power area, but Country has been utilizing less than 1 percent of its total thermal power potential (MoWE, 2011). If significantly increasing developing thermal electricity across Ethiopia, it needs better means and approaches to find best targets for the first few deep wells.

The outcome generated from this research believed to provide detail information about scientific theory and methods for scientific community and concerned body which are responsible for exploration such as governmental body, local and international investor. How to use as a cost-effective tool to explore large areas for geothermal potential and pinpoint smaller target areas for further ground exploration

1.6 Scope of the study

The scope of the study is to detect geothermal Land surface temperature anomaly and comparing it with previously studied papers that related with geothermal resource exploration in one of geothermal prospect area of Tulu Moye.

2. Literature Review

2.1 Theoretical Background

2.1.1 The Earth and its Atmosphere

In the early twentieth century, a young German scientist named Alfred Wegener, His theory was motivated by the observation that the continents, particularly South America and Africa, seemed to be pieces of a global jig-saw puzzle that had somehow been pulled apart (Asrat, 2006). He reasoned that all land masses were once connected in a gigantic supercontinent he named "Pangaea". The northern part of Pangea is commonly called Laurasia and the southern part Gondwanaland. A single supercontinent that broke apart to form the modern continents is called the theory of continental drift. He posited that the now separated continents floated and drifted through a highly viscous sea floor. This part of his theory was later proved incorrect but the basic notion of drifting continents was right. Wegener's problem was in identifying correctly the forces that ripped apart the pieces and in fact keeps them moving.

Other theory which is accepted, that new land was being created on either side of the mid-Atlantic ridge, the so-called "sea-floor spreading" phenomenon (Asrat, 2006). This theory states that the ocean floor has been continually pulled apart along great cracks or belt of weakness. Convection current operating in the upper mantel cause sea floor spreading. These current rise under the oceanic ridge system and then spread laterally from the ridge, carrying the oceanic crust with them. As a result, fault blocks, dropped grabens from median valley on the ridge crest. Magma rises from below the ridge crest, comes to the surface, and erupt as submarine lava flow at Iceland. Earth scientists were able to confirm the movement of the vast plates that constitute the crust of the earth. Continents are part of the crust and have been in constant motion since the beginning of the earth some 4.5 billion years ago.

Today, there is no controversy over the theory of plate tectonics. Detailed structure of the inner earth surface has much uncertainty. Research on Exploring and characterizing the earth's atmosphere has gone several times. Some projects aimed at probing the depth the earth. According to Lee (1978, as cited in Ronald, 2005), in 1909 Croatian scientist Mohorovicic (1857-1936) had observed. It aimed to drill through the thinnest part of oceanic crust (about 5 km thickness) to enter the mantle. He deduced that this represented a boundary between the generally solid crust and the generally molten mantle. However, Project Moho was terminated in 1966 due to lack of fund.

From 1984-1988, they were drilled and the deepest measurement taken at 5822 feet (ft), and indicated a temperature of roughly 290 ^{O}C. Currently there are various countries have Scientific Drilling Program to give insight into earth processes and to test geologic models.

Since the temperature at the base of the crust is about 1100 ^{O}C, temperature gradient between the surface (assuming a surface at 10 ^{O}C) and the bottom of the crust is 31.1 ^{O}C/km (Ronald, 2005). This is usually taken as the normal conductive temperature gradient. Good geothermal prospects occur where the thermal gradient is several times greater than normal. The rate of natural heat flow per unit area is called the normal heat flux; it is roughly 1.2×10^{-6} cal/cm^2 s, in non-thermal areas of the earth.

2.1.2 Active Geothermal Regions

When a plate comes under compression, it can relieve the stress by folding, by cracking and thrusting one piece upon the next, by cracking and trenching beneath the next, and by thickening (Asrat, 2006). These forces can develop at a convergent plate boundary, bending and fracturing rocks in the tectonically active region. In some cases the forces deform rocks tens or even hundreds of kilometers from the plate boundary. Trenching or subduction is one of the most important mechanisms that give rise to high-temperature geothermal regions. When a plate is subjected to tension, it can relieve the stress by cracking open and rifting, by cracking in several places leading to down-dropping, and by thinning. Most of such Earth' activity occur at a divergent boundary, two plates move apart, or separate. A rift valley develops in a continental rift zone because continental crust stretches, fractures, and sinks as it is pulled apart. Continental rifting is now taking place along a zone called the East African rift. All of these responses to tension lead to anomalous geothermal regions that may be conducive to exploitation (Ronald, 2005).

The Great East African Rift System (EARS) is one of the major tectonic structures of the earth that extends for about 6500 km from the Middle East (Dead Sea-Jordan Valley) in the North to Mozambique in the south. This system consists of three main arms: the Red Sea Rift; the Gulf of Aden Rift; and the East African Rift which develops through Eritrea, Ethiopia, Kenya, Tanzania, Zambia, Malawi and northern Mozambique floored by a thinned continental crust (Manfred, 2005). The EARS is composed of two rift trends; the eastern and western branches. The western branch develops from Uganda throughout lake Tanganyika, where it joins the Eastern branch, following the border between Rwanda and Zaire. The western branch is, however, much less active in terms of tectonics and volcanism although both branches are seismically and tectonically active today.

The East African Rift is one of the most important zones of the world where the heat energy of the interior of the Earth escapes to the surface in the form of volcanic eruptions, earthquakes and the upward transport of heat by hot springs and natural vapor emanations (fumaroles). The eastern branch, that forms the Ethiopian and Kenyan rifts, possesses, by far, the most extensive geothermal resource base in Africa and one of the most extensive in the world. Countries such as Djibouti, Uganda, Eritrea and other countries in southeastern Africa have lesser but still important resource bases.

A past several years, possible resource inventory areas within the Ethiopian sector of the East African Rift system, as reflected in surface hydrothermal manifestations has been developed. The highland regions of the country was not completed the inventory works but the rift system has been well covered. About 120 localities within the rift system that are believed to have independent heating and circulation systems, about two dozen are judged to have potential for high enthalpy resource development, including for electricity generation (Teklemariam and Kebede, 2010).

2.1.3 Mechanism of Geothermal Anomaly

Land surface temperature is mainly generated from solar radiation which accounts for a throughout heating of land surface and the Earth's interior heat which is responsible for a localized temperature increase. The understanding of surface energy balance and underground heat transfer will contribute to the identification of geothermal areas caused by Earth's interior heat. At land surface, temperature is the result of balanced surface energy radiation Zhang (1999, as cited in Qin et al., 2011)
In general, the surface energy balance can be simply expressed Monteith (1973, as cited in Qin et al., 2011)

$$Q_d = H + \lambda E + G \ldots\ldots\ldots\ldots\ldots\ldots\ldots\ldots\ldots\ldots\ldots\ldots\ldots\ldots Eq.1$$

where Q_d is the net radiation received by land surface; H denotes the sensible heat flux between the land surface and the lower atmosphere; λE stands for the latent heat flux in the phase transition of water between the underlying surface and the atmosphere; G is the soil heat flux characterizing the thermal exchanges among different depths of soil. For local area the sensible heat flux H and latent heat flux λE can be assumed unchanged, then soil heat flux (G) is a major factor affecting the balance of surface energy Guo (2002, as cited in Qin et al., 2011) . In the lithosphere, the heat is mainly transferred in thermal conduction (Rudnick et al., 1998). This process can be described by the following equation:

$$\nabla(K\,\nabla \mathrm{T}) = -\mathrm{A} \ldots\ldots\ldots\ldots\ldots\ldots\ldots\ldots\ldots\ldots \mathrm{Eq.}\,2$$

where T stands for temperature, K denotes the rock thermal conductivity, and A is the radiogenic heat production of rocks. For local area, heat flow is dominated by rock thermal conductivity K, which is mainly affected by rock's physical and chemical properties Li (1992, as cited in Qin et al., 2011) such as the mineral components, the rock porosity and the fracture filler. Thermal Convection is another important form of underground heat transfer. It exists in the upwelling of underground thermal materials, such as hot water, heated gases, even the up-surging magma along the rock cracks.

2.1.4 Tulu Moye Geothermal Prospect

Tulu Moye geothermal prospect is located in the main Ethiopia rift, which is a part of great African rift valley. Volcanism in the Tulu Moye area involved the extrusion of peralkaline felsic lava associated with young tensional and transverse tectonic features dating from 0.1 to 1.2 million years (Di Paola, 1970). This suggests the existence of a deep seated magma chamber with a long residence time. During 1998-2000, various geological, geochemical and geophysical surveys are conducted in the exploration stage of a geothermal prospect area in Tulu Moye, it confirmed the existence of potential geothermal reservoirs with a temperature in excess of 200 ^{0}C (Ayele et al., 2002) and delineated target areas for further deep exploration. Based on geological, geochemical, and geophysical studies including shallow temperature gradient surveys (150-200 m), in the year of 1998-2000 in the prospective of Tulu Moye-Gedemsa area have reached to the following conclusions (Ayele et al., 2002):

- The widespread occurrence of steaming grounds and hydrothermalized surface, the presence of highly differentiated intermediate to silicic rocks (rhyolitic, ignimbritic etc.), the existence of numerous active faults and phreatic explosion crater indicate the existence of an active heat source possibly a shallow magmatic chamber.
- The basalts are found to be highly fractured and collumunarly jointed characterized by high permeability. Therefore, this unit could serve as a reservoir rock for this geothermal system. Nazareth group ignimbrite, outcropping to the east of the studied area, is affected by transverse faults and could possibly serve as a reservoir rock. The presence of numerous faults and open fissures create secondary permeability. This could possibly be channels for the precipitation of meteoric water.

- The overlying Quaternary volcanics with a general thickness of 200 m and intercalated lacustrine deposits could serve as impervious layer.
- The structural and morphological features of the studied area have indicated that the main recharge of the Tulu Moye Geothermal prospect area could possibly be from the eastern and western escarpment of the rift. The fractured created as a result of intersection of several faults, mostly observed in the east and northeast of the study area could serve as channel of precipitation of meteoric water into the deep geothermal reservoir.
- The study of alteration minerals has indicated the occurrence of both acid sulfate and alkaline type of alteration. The wide distribution of chalcedony deposits in the studied area could possibly indicate a deep reservoir temperature in excess of 150 ^{0}C.
- All thermal waters are bicarbonate types waters and these water system is low enthalpy system.
- The localities south and southeast of Bite village are included within relatively high resistivity zone (50-250 Ohm-m). This zone covers the range of volcanic complex of Jima, Dima and Adano mountains. Locality such as east and northeast of Bite, south of Hamude and northwest of Tulu Moye and Mt. Werdi have relatively low resistivity (< 30 Ohm-m).
- Wide zones of low resistivity laying between the Hamude village in the north and volcano-tectonic complex of jima, Dima, Adano and Moye mountains in the south. Those areas are tectonically affected region with a widespread of alteration products.
- From measured TG wells it can be seen that anomalously high temperatures were registered in all wells. However, TG-1(near Mt. Kechkechi) and TG-4 (near Mt. Dima) wells show high thermal gradients (66 ^{0}C/100 m in TG-1 and 40 ^{0}C/ 100 m in TG-4).

Geological Survey of Ethiopia used to understand the hydrothermal alteration process using XRD analysis. These study analyses suggest the mineral assemblages of kaolinite, tlidimyte which correspond temperature less than 100 °C in an acidic environment; smectite and albite in alkaline (near neutral pH) environment (Tadesse, 2001).

Now a days, the area has been given a priority for further geoscientific investigations like anomaly detection, detailed surface hydrothermal alteration geological mapping and geophysical investigations carried out in the Tulu Moye area.

2.1.5 Hydrothermal Geothermal Resource

A geothermal resource requires fluid, heat, and permeability to generate electricity. Conventional hydrothermal resources contain all three components naturally. These geothermal systems can occur in widely diverse geologic settings, sometimes without clear surface manifestations of the underlying resource (Solomon, 2012).

According to White (1978, as cited in Ronald, 2005), the conceptual model of a hydrothermal geothermal system, which is shown in Figure 2. Water recharge results from meteoric groundwater or rain (point A) and percolating through faults and fractures deep into the formation where it comes in contact with heated rocks. The permeable layer offers a path of lower resistance (point B) and the magmatic body is the heat source leading to convection, as the liquid heats it becomes less dense and tends to rise within the formation. If it encounters a major fault (point C) it will ascend toward the surface, losing pressure as it rises until it reaches the boiling point for its temperature (point D). There it flashes into steam which emerges as a fumarole, a hot spring, a mud pot, or a steam-heated pool associated with the formation of silica and various alteration mineral assemblages (point E).

The intent of a geothermal development project is to locate such systems and Produce them by means of strategically drilled wells, it provides commercially electric power generation. If any one of the five features listed as needed for a viable hydrothermal resource is lacking, the field generally will not be worth exploiting.

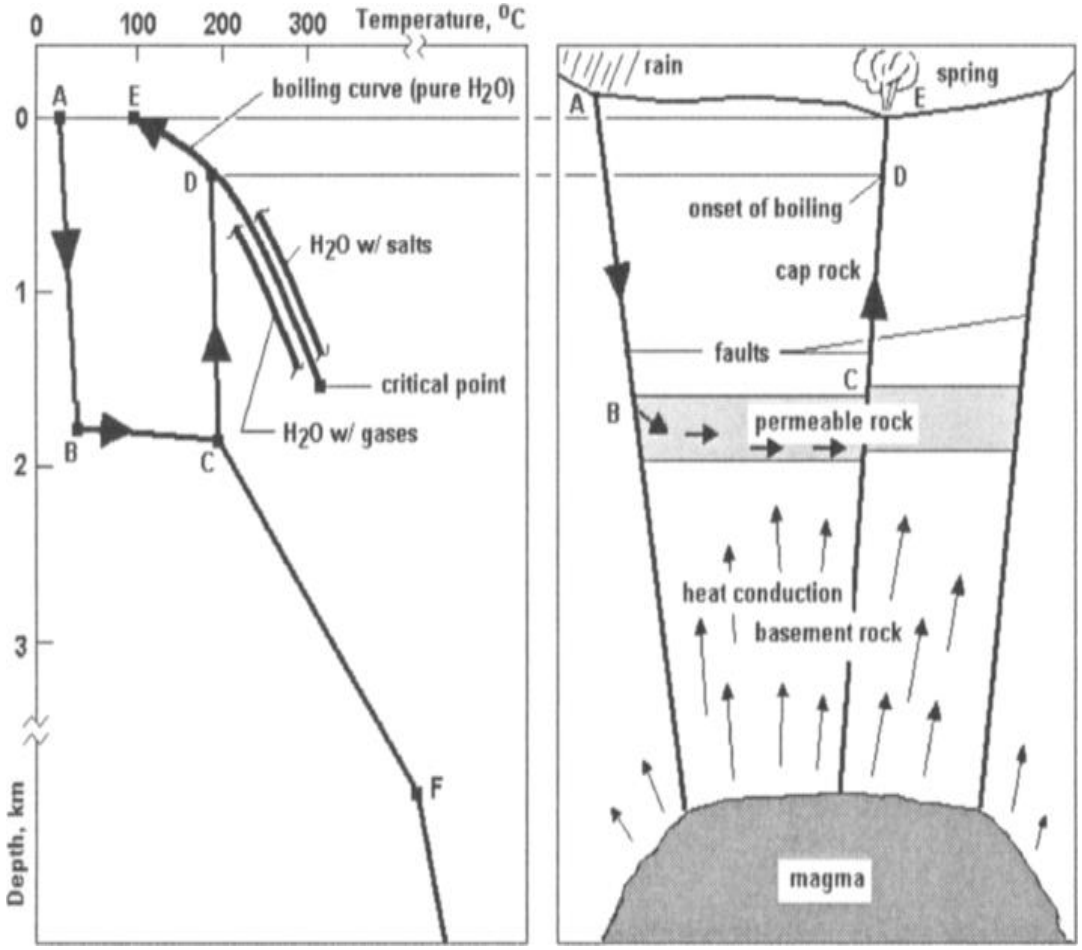

Figure 2: Schematic model of a hydrothermal geothermal system, after White, D.E., 1973

2.1.6 Exploration Strategies and Techniques

Literature survey

Literature survey is likely that someone at some time has taken a look at whatever site is now under consideration. With the use of the Internet, or with other means, it is an easy matter to search the existing literature for prior studies.

There are a databases for most geothermal prospects in Ethiopia. GSE provides information on geothermal manifestation and several other data on all wells and springs with temperatures. There is also a compilation of geochemical information for the fluids at each of steaming ground, springs and wells. With this type of information in hand, the remaining phases can be planned more effectively.

Remote sensing survey

Remote sensing survey in the prospective site can yield the following information that are structural nature of the field, Locations of thermal anomalies and manifestations, Geographic benchmarks to

guide later ground surveys and Geologic mapping. It is an initial reconnaissance survey often using airborne or spaceborne remote sensing in combination with literature study at regional scale results in a selection of a prospective area (Van der Meer et al., 2014).

The various contributions of remote sensing to geothermal research can be grouped under the headings: surface deformation, gaseous emissions, structural analysis, mineral mapping, surface temperature mapping, heat flux mapping and geobotany.

This paper demonstrating the use of TIR data to map surface temperature anomalies. TIR survey can detect very small temperature anomalies, of the order of 0.05-0.5 ^{0}C over areas of up to hundreds of square kilometers. A rise of 0.5 ^{0}C over the normal background would be the result of a heat flux about 50 times greater than the normal heat flux (Ronald, 2005).

Ground Survey

The physical and chemical properties of the geofluid under production conditions are important in deciding on the feasibility of a power project. It may be difficult to obtain this information without drilling wells, but a good exploration program should give a reasonable estimate for these properties. It is conducted "on the ground" and aims at detecting and characterizing the some of the following information:

- A hydrogeological survey aims to reconstruct the water circulation system trying to relate surface manifestations of geothermal activity (e.g., hot springs, steam vents, fumaroles, etc.) to fault/fracture systems, variation in lithology etc. (Van der Meer et al., 2014).
- Used to develop geothermometers that provide an estimate of the temperature of deep reservoirs (Arnorsson et al.,2006).
- It provide information about subsurface lithology and active seismic surveys as well as (passive) seismic tomography and provide information about subsurface structure and identification of warmer and cooler regions(Lees, 2007).

The aim is to better understand the behavior of a geothermal reservoir, to find the most suitable and productive reservoir, to estimate reservoir volume and recoverable heat, to identify zones of high permeability, to locate drilling locations, and to forecast future well and reservoir behavior. The ultimate exploration tool is the drilling of deep wells based on the findings of the scientific surveys.

2.1.7 Remote sensing

Remote sensing is the instrumentation, techniques and methods to observe the earth surface at a distance and to interpret the image or numerical value obtained in order to acquire meaningful information of particular object on earth (Henk and Jan, 1993). Acquired information usually stored as image data. The characteristics measured by sensor depends on reflected and emitted energy by earth surface. This energy in the form of Electromagnetic radiation (EMR).

All EMR has fundamental properties and behaves in predictable ways according to the basics of wave theory. Two characteristics of electromagnetic radiation are particularly important for understanding remote sensing. These are the wavelength and frequency .Wavelength (λ) is defined as the distance between successive wave crusts. Frequency (V) is the number of cycles of a wave passing a fixed point over a specific period of time.

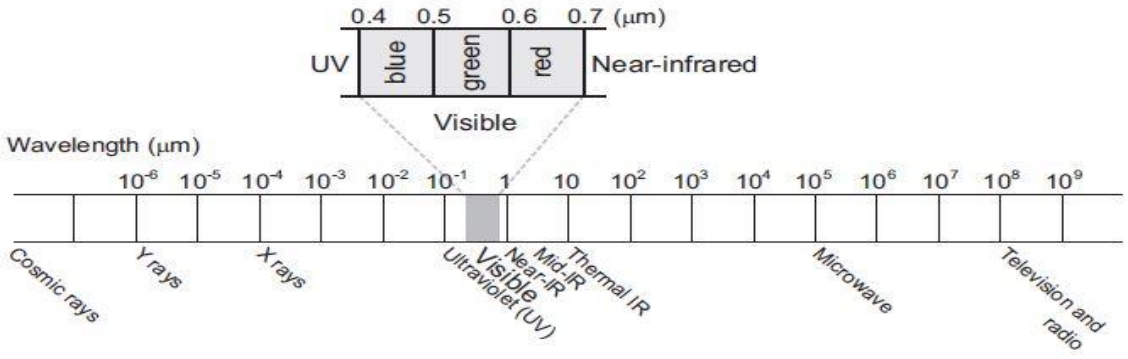

Figure 3: The Electromagnetic spectrum after Thomas M. Lillesand and Ralph W.Kiefer, 1994

All matters with a certain temperature radiates electromagnetic waves of various wavelengths. Figure 3 shows the total range of wavelength is commonly referred to as the electromagnetic spectrum. It extends from gamma rays to radio waves.

Remote sensing operates in several region of the electromagnetic (EM) spectrum. Visible region of spectrum is relatively small portion in the EM spectrum. It is important in the visual interpretation and analysis. Remote sensing are used thermal infrared and microwave region. Thermal infrared gives information about surface temperature. Microwave can provide information on the surface roughness and the properties of the surface such as water content. In remote sensing, observation of the earth is carried out using the remote sensing satellites with their remote sensor. Remote sensing satellites are characterized by their altitude, orbit and sensor.

The Landsat program is the oldest earth observation program. It started in 1972 with the Landsat 1 satellite carrying the MSS multispectral sensor. After 1982, the thematic Mapper (TM) replaced the MSS sensor. In April 1999 Landsat 7 was launched carrying the ETM+ scanner. Now a days, it has got Scan Line Corrector (SLC) failed, but it is operational till now. The Landsat Data Continuity Mission (named Landsat 8) launched from Vandenberg Air Force Base in California on February 11, 2013. It has carries two-sensor payload: the OLI and TIRS (Table 1).

Table 1: Landsat 8 characteristics

System	Landsat-8	
Orbit	705 km,98.2, sun-synchronous, 10:00AM crossing,	
Sensor	OLI, TIRS	
Swath width	185 km	
Revisit time	16 days	
Spectral bands	OLI	TIRS
	Band 1 Visible (0.43 - 0.45 µm) Band 2 Visible (0.450 - 0.51 µm) Band 3 Visible (0.53 - 0.59 µm) Band 4 Red (0.64 - 0.67 µm) Band 5 Near-Infrared (0.85 - 0.88 µm) Band 6 SWIR 1(1.57 - 1.65 µm) Band 7 SWIR 2 (2.11 - 2.29 µm) Band 8 Panchromatic (PAN) (0.50 - 0.68 µm) Band 9 Cirrus (1.36 - 1.38 µm)	Band 10 TIRS 1 (10.6 - 11.19 µm) 100 m Band 11 TIRS 2 (11.5 - 12.51 µm) 100 m
Spatial resolution	15m (band 8),30m (bands 1-7,9), 100m(band 10-11)	
Data achieved at	Earthexplorer.usgv.gov	

The application of Landsat 8 is a lot using each spectral band such as: land cover mapping, land use mapping, soil mapping, geological mapping, surface temperature mapping, mineral mapping, et cetera (Table 2).

Table 2: Principal applications of the Landsat 8 bands. Source: United State of Geological Survey (USGS).

Band	Wavelength Micrometres (μm)	Application
1-coastal aerosols	0.43-0.45	Coastal and aerosol studies.
2-blue	0.45-0.51	Bathymetric mapping, distinguishing soil from vegetation and deciduous from coniferous vegetation.
3-green	0.53-0.59	Emphasizes peak vegetation, which is useful for assessing plant vigor.
4-red	0.64-0.67	Discriminates vegetation slopes.
5-Near Infrared (NIR)	0.85-0.88	Emphasizes biomass content and shorelines.
6-Short-wave Infrared (SWIR) 1	1.57-1.65	Discriminates moisture content of soil and vegetation; penetrates thin clouds.
7-Short-wave Infrared (SWIR) 2	2.11 - 2.29	Improved moisture content of soil and vegetation and thin cloud penetration.
8-Panchromatic	0.50 - 0.68	15 meter resolution, sharper image definition.
9- Cirrus	1.36 - 1.38	Improved detection of cirrus cloud contamination.
10- TIRS 1	10.60 – 11.19	100 meter resolution, thermal mapping and estimated soil moisture. Resample (30 m)
11- TIRS 2	11.5 - 12.51	100 meter resolution, Improved thermal mapping and estimated soil moisture. Resample (30 m)

2.1.8 Remotely Sensed Thermal Infrared

There is no strict or physical definition of the thermal infrared domain. The thermal infrared wavelength domain extends from about 3 to 14 μm (Sabins, 1996). In this range thermal mapping of the earth's surface is possible due to atmospheric windows in the 3–5 μm range, as well as in the 8–14 μm range (Figure 4).

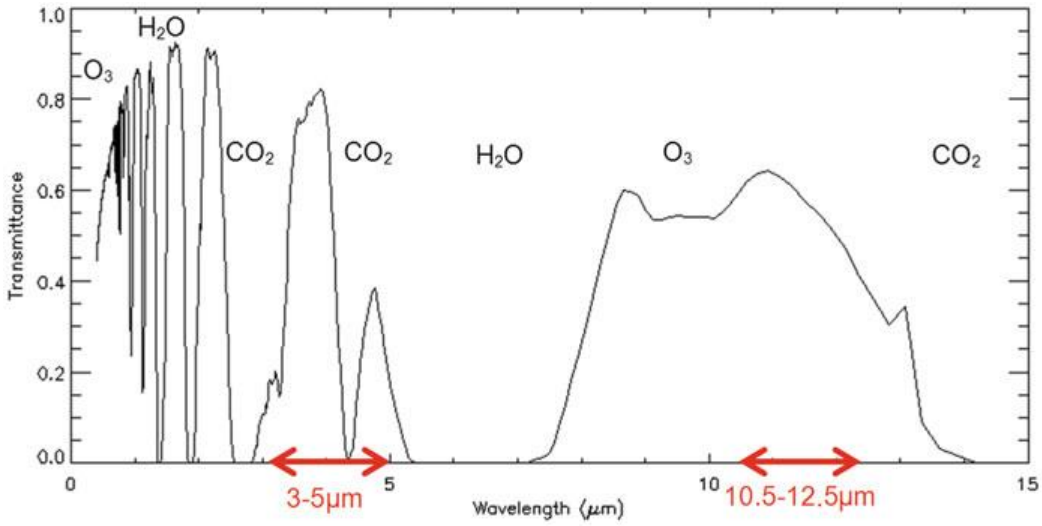

Figure 4: The thermal infrared wavelength domain, typical absorption bands induced by gasses and water, and atmospheric transmittance (atmospheric windows) (Figure courtesy of Rudolf)

Within the 8–14 μm range only a narrow absorption band of ozone, O3, exists, which is omitted by most sensors. Within the 3–5 μm range reflected sunlight can still slightly contaminate the (emitted) thermal signal, which has to be taken into account when analyzing daytime 3–5 μm TIR imagery.

However, different authors define the TIR domain slightly differently. According to Thomas and Ralph, (1994), the TIR domain ranges from 3 to 1,000 μm. The main characteristic common to all definitions is the fact that TIR remote sensing records emitted radiation, whereas multispectral remote sensing in the visible (VIS), and near infrared (NIR), domain records reflected radiation. Only within the shorter wavelength part of the TIR spectrum (<5 μm) can the thermal signal still be slightly disturbed by reflected radiation.

Planck's Law

Planck's blackbody radiation law, Planck's law for short, describes the electromagnetic radiation emitted by a blackbody at a given wavelen+

gth M_λ as a function of the blackbody's absolute temperature. Simply by specifying a certain wavelength in Equation 3, M_λ can be calculated from the body's temperature (figure 5).

$$M_\lambda = \frac{2\pi hc^2}{\lambda^2\left(e^{\frac{hc}{\lambda kT}}-1\right)} \ldots\ldots\ldots\ldots\ldots\ldots\ldots\ldots Eq.3$$

With: M_λ = Spectral radiant exitance [W m-2 μm-1]

h = Planck's constant [6.626×10^{-34} J s]

c = speed of light [2.9979246×10^{8} m s^{-1}]

k = Boltzmann constant [1.3806×10^{-23} j k^{-1}]

T = absolute Temperature [K]

λ = wavelength [μm]

The total energy a blackbody radiates and the wavelength of maximum emittance depend on the temperature of the blackbody and can be described by Stefan- Boltzmann's law and Wien's law.

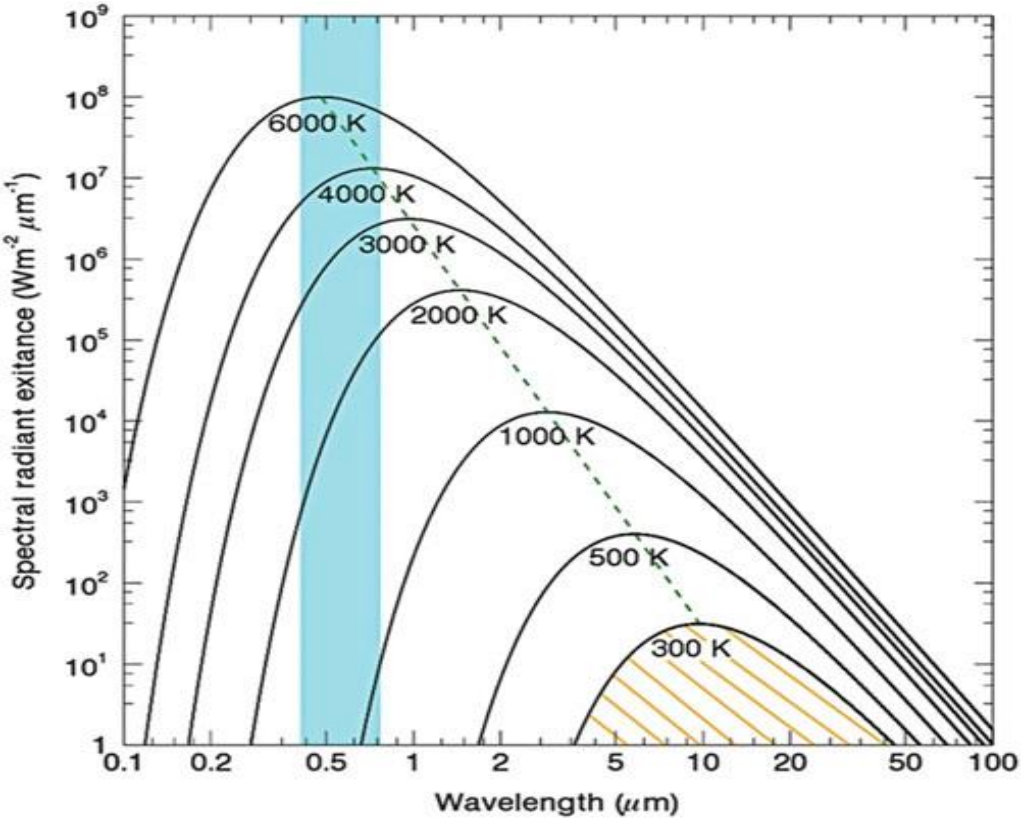

Figure 5: Blackbody radiation curves at different selected temperatures, as derived from Eq.1.

Stefan-Boltzmann Law

The Stefan-Boltzmann law (Equation 4) describes the total electromagnetic radiation emitted by a blackbody as a function of the absolute temperature of that blackbody (Walker, 2008). The emitted radiation corresponds to the area under the radiation curve (integral) as depicted in Figure 4.

$$T_{RadBB} = \sigma (T_{kit})^4 \quad \ldots\ldots\ldots\ldots\ldots\ldots\ldots Eq.4$$

T_{RadBB} = radiant flux of a blackbody [W/m2]

T = absolute kinetic temperature [K]

σ = Stefan-Boltzmann constant [5.6697×10^{-8} W m^{-2} K^{-4}]

This equation shows that the higher the temperature of the radiating object the greater the total amount of radiation (energy) it emits.

Wien's Displacement Law

Wien's law describes the wavelength at which maximum spectral radiant exitance occurs (Walker, 2008):

$$\lambda_{max} = \frac{A}{T} \ldots\ldots\ldots\ldots\ldots\ldots\ldots\ldots\ldots Eq.5$$

λ_{max} = wavelength of maximum spectral radiant exitance [μm]

A = Wien's constant [2897.8 μm K]

T = Absolute kinetic temperature Kelvin [K]

With increasing temperature of an object, its maximum exitance λ_{max} shifts to shorter wavelengths. This could be seen in Figure 5. With an average temperature of 5,778 K (5,505 ^{o}C), the sun has its peak emission in the Visible domain of the spectrum (roughly at green: 0.55 m), while a much colder object such as the earth has its peak of emission in the TIR.

Kirchhoff's Law

Due to emissivity below 1 for real materials, the radiance temperature, $T_{(rad)}$, measured by a sensor is always lower than the real kinetic (surface) temperature, $T_{(kin)}$, of an object.

$$T_{(rad)} = e^{\frac{1}{4}} \times T_{(kin)} \ldots\ldots\ldots\ldots\ldots\ldots\ldots Eq.6$$

This is a crucial fact for thermal data analysis, as it means that objects with exactly the same kinetic temperature can differ significantly in their radiant temperature. Depending on the variability of land cover surfaces (varying geologic surfaces, moisture conditions, amounts of vegetation cover, etc.) an image has to be corrected for the emissivity effect when aiming to retrieve kinetic pixel (object) temperatures.

2.2 Previous Work

Much of the published research on the use of TIR remote sensing for mapping surface temperature anomalies has focused on the use of airborne thermal imagery. Acquired pre-dawn broadband

thermal imagery (in the 8–14 μm wavelength region) in the region of Long Valley and the Salton Sea, California, USA to map surface geothermal anomalies (Hodder, 1970). Simple visual analysis and application of thresholds to the thermal data provided the basis for identification of hot waters at springs and heated ground overlying faults providing potential indicators of geothermal upwelling zones. Exploited pre-dawn airborne thermal imagery to map geothermal features in the Black Rock Desert area of Nevada, USA (Lee, 1978). The thermal data provided an effective method for inventorying known geothermal features and mapping many previously unreported hot springs and related fractures.

Utilized a GEOSCAN MkII aerial scanner to acquire 3 m spatial resolution, multispectral TIR data (six bands in the 8.4–11.6 μm wavelength region) during 1992 and 1993 for a 100 km^2 area covering the Waimangu-Waiotapu geothermal region with the aim of mapping and monitoring surface geothermal features (Mongillo, 1994). The acquired thermal data was empirically calibrated using in-situ measurements of non-geothermal water bodies and the resultant surface temperature data was visually interpreted. The results enabled mapping of all the known and many previously unidentified geothermal features including hot springs, hot ground, and thermal seeps into lakes. The results clearly outlined that geothermal features at the Waiotapu field occur along lineations providing strong evidence for a fault controlled upflow/outflow of geothermal fluids. Comparison of the results from different years indicates that a large hot spring appeared in the Waimangu geothermal field between the two survey dates, which demonstrates the potential of TIR data for monitoring temporal changes in geothermal surface features.

Airborne multispectral mid-wave (MWIR: 3.6–5.1 μm) and longwave-infrared (8.1–12.4 μm) data acquired with an ADS SpectraView and US Fish and Wildlife Service (USFWS) 'Firemapper' system respectively to map and monitor thermal features in the Norris Geyser Basin, Yellowstone National Park (Seielstad and Queen, 2009). The ~1–3 m spatial resolution data acquired during daytime and nighttime surveys in 2005 and 2006 were calibrated to surface kinetic temperature values with an empirical correction using in-situ temperature measurements. The TIR data enabled detailed mapping of surface geothermal phenomena in the Norris Geyser Basin including discrete features such as hot springs and geysers as well as 'background' areas of sinter and heated ground. (Seielstad and Queen, 2009) used the data to broadly delineate the geographic boundaries of the Norris Geyser Basin that was previously poorly defined. In addition, more detailed mapping of a series of sub-basins within the Norris Geyser Basin was also undertaken. For the 2005 data, snow

fall prior to the survey facilitated the mapping of geothermal ground that was snow free in contrast to the surrounding snow covered non-geothermal areas.

A study of Haselwimmer et al., (2011) ware acquired ~1 m spatial resolution airborne thermal imagery using broadband a FLIR (Forward Looking Infrared) system during fall and winter-time survey over Pilgrim Hot Springs located near Nome in Western Alaska. The mosaicked and calibrated data enabled the detailed mapping of known and previously unmapped geothermal features including hot springs and pools, thermally anomalous ground, and ice free-areas on the nearby Pilgrim River that indicated geothermal outflow at a distance from the known spring's site.

Although coarse spatial resolution satellite thermal sensors (60–90 m pixels), such as Landsat or ASTER, have limited potential for detailed mapping of discrete geothermal features a number of studies have exploited these datasets for broader scale detection of geothermal anomalies. These studies have commonly applied data processing techniques to enhance and detect what may be subtle surface temperature anomalies. At the resolution of satellite TIR data, pixels corresponding to geothermal areas normally record a mixture of emitted radiance from geothermal sources as well as from background non-geothermal surfaces. This acts to reduce the measured temperature of pixels corresponding to geothermal sources. When this is compounded by other environmental factors such as land surface type, topography, albedo, and thermal inertia then it can be difficult to locate geothermal anomalies with confidence.

According to Coolbaugh et al., (2007) Brady's Hot Springs, Nevada, USA, processed a day/night pair of ASTER scenes (acquired on the same date) to minimize the effects of diurnal heating. Applied corrections for albedo, topographic slope, and thermal inertia based upon a simplified heat energy model describing net surface radiation flux. The resultant processed image shows that background variations in temperature were reduced by 30–50 % whilst the intensity values of geothermal anomalies were retained. This made it easier to distinguish geothermal activity from false thermal anomalies associated with variations in topography, rock/soil types, and non-thermal springs.

The study of Kienholz et al., (2009) used multi-temporal Landsat thermal data to map geothermal anomalies on the Island of Akutan located on Alaska's Aleutian Arc. Twelve summertime cloud-free scenes were selected from the Landsat archive corresponding to acquisitions over Akutan Island between 1985 and 2008. The Landsat thermal bands were calibrated to surface kinetic temperature and an image stacking procedure was used to highlight persistent surface temperature anomalies

and subdue background transient temperature effects associated with local scene specific conditions. As some persistent temperature effects remained after stacking, the results were further classified based upon elevation, slope, vegetation type and geology. This processing strategy mapped the locations of the known fumarole field and thermal springs and also revealed three new distinct regions of surface thermal anomalies providing targets for field investigations.

The study Qin et al., (2011) on the Tengchong area (Yunnan province) in China using Landsat-7 Enhanced Thematic Mapper (ETM+) sensor. Based on radiometric calibration, atmospheric correction and emissivity calculation, a simple but efficient single channel algorithm with acceptable precision is applied to retrieve the land surface temperature (LST) of study area to detect anomalous surface temperature.

Radiometric calibration was applied to convert the Digital Number (DN) recorded by the remote sensor into the at-atmosphere radiance. Radiometric calibration was carried out according to Landsat 7 user Handbook. In this study Landsat 8 user Handbook were used to retrieve at-atmosphere radiance. Thus, atmospheric correction is required to retrieve the real surface parameters by removing the atmospheric effects, such as the absorption, upward emission and scattering of the radiation from the earth surface. 6S (Second Simulation of the Satellite Signal in the Solar Spectrum) model is a popular atmospheric correction model based on the simulation of the radiative transfer process to derive the at-surface reflectance with accredited precision (Martin, 2012). The model can simulate the solar radiation on the ground and in the atmosphere from 0.2 μm to 4.0 μm spectral range under a variety of conditions of both ground surface and atmosphere (Vermote et al., 1997b). Giving the radiance from the top of atmosphere (TOA), viewing geometry and the atmosphere related parameters the model can estimate the reflectance or radiance on the ground, and atmospheric absorption and scattering characteristics. These parameters can be used for atmospheric correction of satellite remote sensing data. Therefore, in this study, applied 6S model to remove the atmospheric effect from the Landsat 8 data of the forth band (red band) and fifth band (near infrared band).

Emissivity is a key variable in LST retrieval. There are two ways to obtain the emissivity: firstly, Look-Up-Table (LUT) method, in which the emissivity values are assigned to each class derived from conventional image classification; it is based on the use of conventional land cover classification information. This method assumes that similarly classified land covers exhibit very similar LSE. The key point of this method is to properly classify the land surface and then to assign the emissivity from classification-based look-up tables. It is accurate for most classes, especially

for high-resolution remotely sensed data (pure pixel). The accuracy of the LUT method is greatly hindered by mixed pixel issues and depends on the precision of classification. Landsat 8 data is 30 m spatial resolution, it can acquire varies types of features in single pixel. Therefore, LUT method is not better option for medium and low resolution datasets. Another better mothed is pixel level emissivity, is called NDVI Thresholds Methods. This approach is applied to calculate emissivity in this study. This method is based on a statistical relationship between the NDVI derived from the VNIR bands. NDVI computed from the atmosphere corrected red reflectance and near infrared reflectance from multispectral data.(Van de Griend and Owe, 1993) first reported a very high correlation between the LSE in the band covering from 8 to 14 µm and the logarithmic NDVI, that is,

$$\varepsilon = a + b\ln(NDVI) \dots\dots\dots\dots\dots Eq.7$$

Where a and b are the constants derived from the regression analysis. Although this method is a potentially powerful tool to estimate the LSE at a pixel scale directly from space because NDVI can be easily derived from the reflectances in VNIR bands, this type of relationship has been proven to be quite dependent on the area studied, which means the coefficients a and b obtained for one site cannot be applied to other sites (Van de Griend and Owe, 1993).

Considering the complexity of method proposed by (Valor and Caselles, 1996; Sobrino and Raissouni, 2000) reduced the complexity and formulated an operational NDVI threshold method to derive the LSE from space. This method assumes that:

1. The surface is only composed of soil and vegetation,
2. The emissivity of the bare soil can be linearly represented by the surface reflectivity in the red channel, and
3. The LSE changes linearly with respect to the fraction of vegetation in a pixel.

Therefore, the LSE of TIR channel i can be estimated using three linear functions corresponding to conditions in which a pixel is composed of full vegetation, of full soil, or of mixed soil/vegetation content, namely,

$$\varepsilon_{i=} \begin{cases} a_i + b_i \rho_{red} & NDVI < NDVI_s \\ \varepsilon_{vi} P_V + \varepsilon_{Si}(1 - P_V) + d\varepsilon_i & NDVI_s < NDVI < NDVI_v \end{cases} \quad \dots\dots\dots Eq.\ 8$$

$\varepsilon_{vi} + d\varepsilon_i$ NDVI > $NDVI_v$

Where a_i and b_i are the channel-dependent regression coefficients, is the reflectivity of the red channel, and $NDVI_s$ is the NDVI corresponding to the bare soil. ε_{vi} and ε_{Si} are the vegetation and soil emissivities in channel i, and j respectively. Both of them can be measured in the field (Rubio et al., 2003) or obtained from an emissivity database (Baldridge et al. 2009). P_V is the fraction of vegetation that can be derived either from the NDVI (Sobrino and Raissouni, 2000). Vegetation fraction is the percentage of the vertical projection of vegetation canopy (including leaves, stems, and branches) in per unit area. It can be derived from NDVI of study area (Carlson and Ripley, 1997): it is one of the most important parameter to estimate land surface emissivity. $d\varepsilon_i$ is the mean cavity effect and can take values of 0.02 and higher from numerical simulation (Valor and Caselles 1996), and $NDVI_v$ is the full vegetation NDVI. $NDVI_s$ and $NDVI_v$ can be estimated from the histogram for the entire scene (Sobrino et al., 2008).

Considering the landform of Tengchong area (Yunnan province) in China, the emissivity values was calculate based on NDVI threshold method. In this case, the study area is composed by a mixture of bare soil and vegetation, and the emissivity was calculated according to the following equation 9 (Sobrino et al., 2004). In this paper, NDVI threshold method was apply to drive emissivity from OLI sensor.

$$\varepsilon = mPv + n \dots\dots\dots\dots\dots\dots\dots\dots\dots Eq.9$$

Single Channel (SC) algorithm method was applied to detect geothermal anomaly area in Tengchong area (Yunnan province), China (Qin et al., 2011). SC algorithm proposed by Artis and Carnahan, (1982). The main goal of the single-channel method is to obtain an algorithm to retrieve LST from one thermal band of the sensor. SC requires the least amount of parameters for temperature retrieval compared to the mono-window algorithm (Qin et al., 2011) and the generalized single-channel method (Jiménez-Mu˜noz and Sobrino, 2003). The formula is as follows:

$$T_s = \frac{T_{sensor}}{1 + \left(\lambda \times {}^{T_{sensor}}/_{\rho}\right) \ln \varepsilon} \quad \dots\dots\dots\dots\dots Eq.10$$

Tsensor is at-sensor brightness temperature was carried out from spectral radiance of ETM+ Band 6 imagery to Kelvin according to derived formula (USGS, 2009).

The basis of the mono-channel technique (or split-window when it is applied in the region 10–12.5 μm) is that the atmospheric attenuation suffered by the surface emitted radiance is proportional to the difference between the at-sensor radiances measured simultaneously in two different thermal channels. Many papers have used this technique to extract sea/land surface temperature. This method is only applicable for the sensor with two or more thermal channels. For the sensor with two thermal channel, in the case of Landsat 8 data, split-window algorithm is preferred. A split-window algorithm for deriving LST from advanced very high resolution radiometer (AVHRR) channels 4 and 5 is proposed and validated with in situ measured temperatures. The proposed algorithm yields standard errors of temperature estimate between ±1.0 and ±1.5 K and no significant biases was observed (Cesar and Vicente, 1997). In addition, matched ground-measured temperatures from SURFRAD and GOES-8 data were used to evaluate the optimal algorithm, and the study of Yu et al., (2009) showed that this algorithm was capable of achieving the precision of 2.3 K.

A study of Jiménez-Muñoz et al., (2014) provide a complete set of split window coefficients that can be used to retrieve LST from thermal infrared sensors onboard the most popular remote-sensing satellites. The coefficients have been obtained by minimization from an extensive simulated database constructed from MODTRAN radiative transfer code calculations, emissivity spectra extracted from spectral libraries, and spectral response functions of the thermal bands considered. It analyzed the magnitude of the error on the LST retrieval and the contribution to the error of the different uncertainties. The validation and calibration of LST for Landsat-8 TIRS data have been done in 2014 using both SW and SC algorithm. As a result, retrieved ground based measurements and LST value with both algorithm has lower RMSE (Root Mean Square Error), It shows mean errors typically below 1.5 K for both SC and SW algorithms, with slightly better results for the SW algorithm than for the SC algorithm with increasing atmospheric water vapor contents (Skokovic et al., 2014).

A study of Qin et al., (2011), the LST anomalous areas with temperature about 4–10 K higher than background area are discovered. Four geothermal areas are identified with the discussion of geothermal mechanism and further analysis of regional geologic structure. However, the artificial thermal influences were not considered to exclude false anomaly. In this paper, artificial thermal influences would be considered.

3. Materials and Methods

3.1 Geographic Setting

3.1.1 Location of Study Area

Tulu Moye geothermal Prospect is located in the central Main Ethiopia Rift (MER). It is located in the northwest of Asela, region of Oromia. It is about 200 km south east part of Addis Ababa. It covers a large area that lies between 8.283^{0}N to 8.050^{0}N latitude and 38.976^{0}E to 39.268^{0}E Longitude covering a total area of more than about 572 km^2 (Figure 6). The most geothermal manifestation in the area located between 8.143^{0}N to 8.268^{0}N latitude and 39.041^{0}E to 39.20^{0}E longitude.

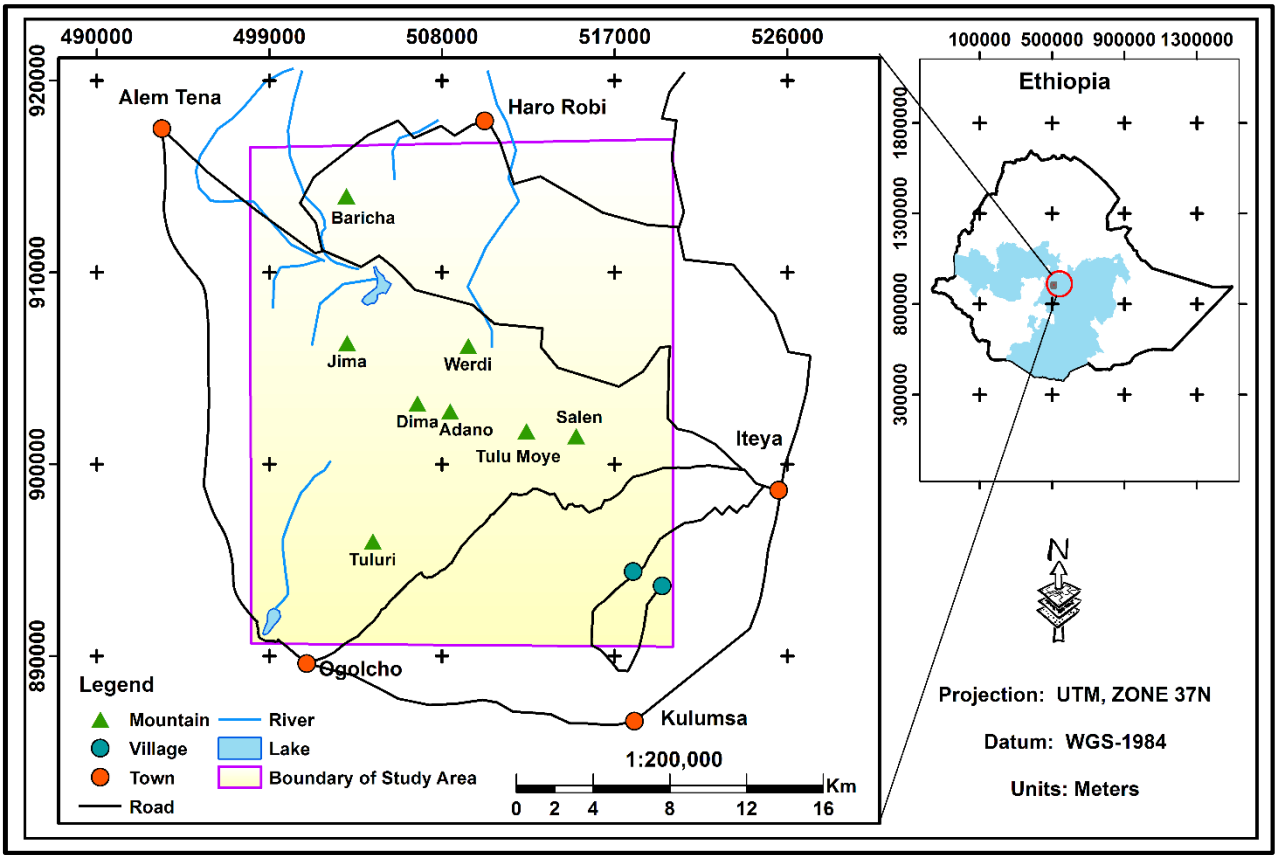

Figure 6: Location map of the study area.

The study area is bounded by two main Asphalted high Roads namely; Nazreth- Asella and Mojo-Ziway, both of them are helpful to reach the area. However, there are tree dry weather roads both crossing the area, one from Kulumsa through Olgocho to Meki; the other from Dera to Haro Robi, which has been useful to access important geologic outcrops, structures and representative sites for this study. The third one is from Kulumsa through Bite river to Alem Tena.

3.1.2 General Geology of Ethiopian Rift

MER is lying within 5º00’ and 9º00’N latitude and 37º00’ and 39º00’ E longitude Mohr (1967, as cited in Engdawork, 2007), as mentioned in figure 1. It is geographically divided in to three sub sectors: northern, central and southern sectors (WoldeGabriel et al., 1990) and bordered by the Ethiopian plateau to the west and Somalia plateau to the east. It has a very complicated geological evolution and tectonic history. Mohr (1967, as cited in Engdawork, 2007) its geometry is characterized by normal step faults with orientation ranging from NNE-SSW to NE-SW. The rift valley was the site of extensive volcanic activities during the Tertiary. During the Tertiary period, Ethiopian rift valley was the extensive volcanic activities. The rift valley was the site of extensive volcanic activities during the Tertiary. Volcanic rocks such as pantelleritic rhyolite, trachytes, ignimbrites and basalts are abundant within the rift floor and on the adjoining plateaus during Pliocene and Pleistocene age.

The oldest volcanic rocks, the plateau Trap Series, are exposed in the western escarpment and consist of basaltic lava with interbedded ignimbritic beds, overlain by massive rhyolites and intervening tuffs and basalts (Di Paola, 1972; Woldegebriel et al., 1990). The eastern margin, shield volcanoes (Chilalo, 4005 m; Kekha 4245 m; Badda, 4170 m). These consist of trachytes with subordinate basalt (WoldeGabriel et al., 1990; Bigazzi et al., 1993). Silicic pyroclasic materials cover most of the MER floor. Silicic pyroclasic materials cover most of the MER floor, mainly peralkaline rhyolitic ignimbrites interlayered with basalts and tuffs. Alkaline and peralkaline rhyolitic lava flows and domes associated with pumice and ash represent the late silicic volcanic events (Di Paola, 1972). These lavas were erupted from late Pliocene to middle Pleistocene. More recent volcanic unit outcrops along the Silti-Debre Zeit Fault Zones (SDZFZ) and the Wonji Fault Belt (WFB) (Di Paola, 1972; Kazmin et al., 1980); it is made up of basaltic lava flows associated with scoria cones. Young volcanoes and calderas, such as Bora Bericcio complex, the Aluto volcano and Corbetti calderas, are made up of rhyolitic lava flows, unwelded pumice flows and ashes.

The Precambrian rocks in Ethiopian Rift System, except in the northern Afar and at the extreme south of the Ethiopian Rift, are mostly covered by more recent Tertiary volcanic rocks and Mesozoic sediments Mohr (1967, as cited in Engdawork, 2007).

Generally, Ethiopian Rift divide volcanic product into six main tectonomagmatic chronozones since Eocene to Oligocene (WoldeGabriel et al., 1990). That are as follows: The description is adopted from this work as follows:

- ✓ **Kella Basalt**: this is the oldest volcanic unit in the central sector of MER and is found at Agereselam, Ambo and Kella. These rocks are dominated by basalt with localized rhyolite and sedimentary strata.
- ✓ **Shebele Trachyte**: the rocks of this unit are exposed along some deep canyons of Omo River and the Wabi Shebele. This group is dominated by intermediate and acidic volcanic rocks such as trachyte, phonolite, rhyolite and intercalated volcanoclastic strata.
- ✓ **Guraghe Basalt**: Basalts and subordinate silicic flows of this unit are found at Awasa, Guraghe and Omo river canyon. In Omo river canyon, these 10.6 Ma old basalts are underlain by several undated basalt flows and Middle Miocene Shebele trachytes. At Awasa and Guraghe, the base of correlative units is not exposed.
- ✓ **Butajira Ignimbrite**: Voluminous silicic pyroclastic material and subordinate basalt flows of this unit were erupted from the Awasa caldera, the Wegebta caldera complex and a major caldera probably buried beneath the Ziway- Langano- Abijata basin. Petrologically these groups of rhyolitic rocks are distinguished from those of the Quaternary Wonji Group as being transitional or mildly peralkaline while the Wonji Group is peralkaline.
- ✓ **Chilalo Trachyte**: This group includes the product of Pliocene centers of the eastern and western shoulder of the rift and compositionally correlative units from the Awasa caldera. It includes trachyte, silicic rocks and basalt that overlie units of either Shebele trachyte or Butajira Ignimbrite.
- ✓ **Wonji Group**: This group is generally confined to the WFB, along the entire MER and also includes the young basalts of SDZFZ. This group consists of the diverse Quaternary lava, pyroclastic rocks and volcanoclastic strata younger than 1.6 Ma.

3.1.3 Geology of Study Area

According to Ayele et al., (2002) made surface geology of Tulu Moye area can be presented in terms of stratigraphy, structural features and hydrothermal activity. The detail pictorial representation is shown in figure 7.

Stratigraphy

Obsidians (QTo): are common in the studied area and form thick viscous lava flows mainly porphyritic but there are also the non-porphyritic flows highly fractured and having high

permeability. There are aphyric to porphyritic varieties. The porphyritic variety has spherulitic (vitro-porphyritic) texture with phenocrysts of glagioclase (sanidine) and pyroxene (partially altered to clay) and groundmass is totally glass. They are outcropping mainly on the eastern side of the mapped area, around Mt. Gnaro and Mt.Jano following the NNE-SSW structure flowing over the basalt (QWb).

Trachytes (QTt): They form moderate domes, and are concentrated on the eastern part of the area. They found on the eastern and southern part of the study area and also near Bite lake. The rock has trachytic texture with phenocrysts of plagioclase (andesine) and olivine (idingsitized) and minor pyroxene (partially altered) and quartz. The Groundmass is dominantly plagioclase lath and opaque minerals (Fe-oxides).

Basalts (QWb): They cover relatively larger area. Mostly they are fresh and scoriaceous. There are different varieties of lavas. They are cover most of the north-eastern part of the area and some on the southern end of the area. They have aphanitic texture, and the major constituents are microphenocrysts of plagioclase, olivine and pyroxene, and the groundmass is dominated by plagioclase lath, olivine, pyroxene and iron oxide.

Pumice pyroclastics and poorly welded tuffs (Qtpu): They are mainly characterized by pumice breccia and sometimes by lithic breccia (obsidians and rhyolites). The pumice breccia fill valleys and flow over pre-existing topographic features (mostly they are concentrated in the center of the mapped area). This unit cover most of studied area especially western half of the area. It associated, at depth, with poorly welded pumiceous ignimbrite.

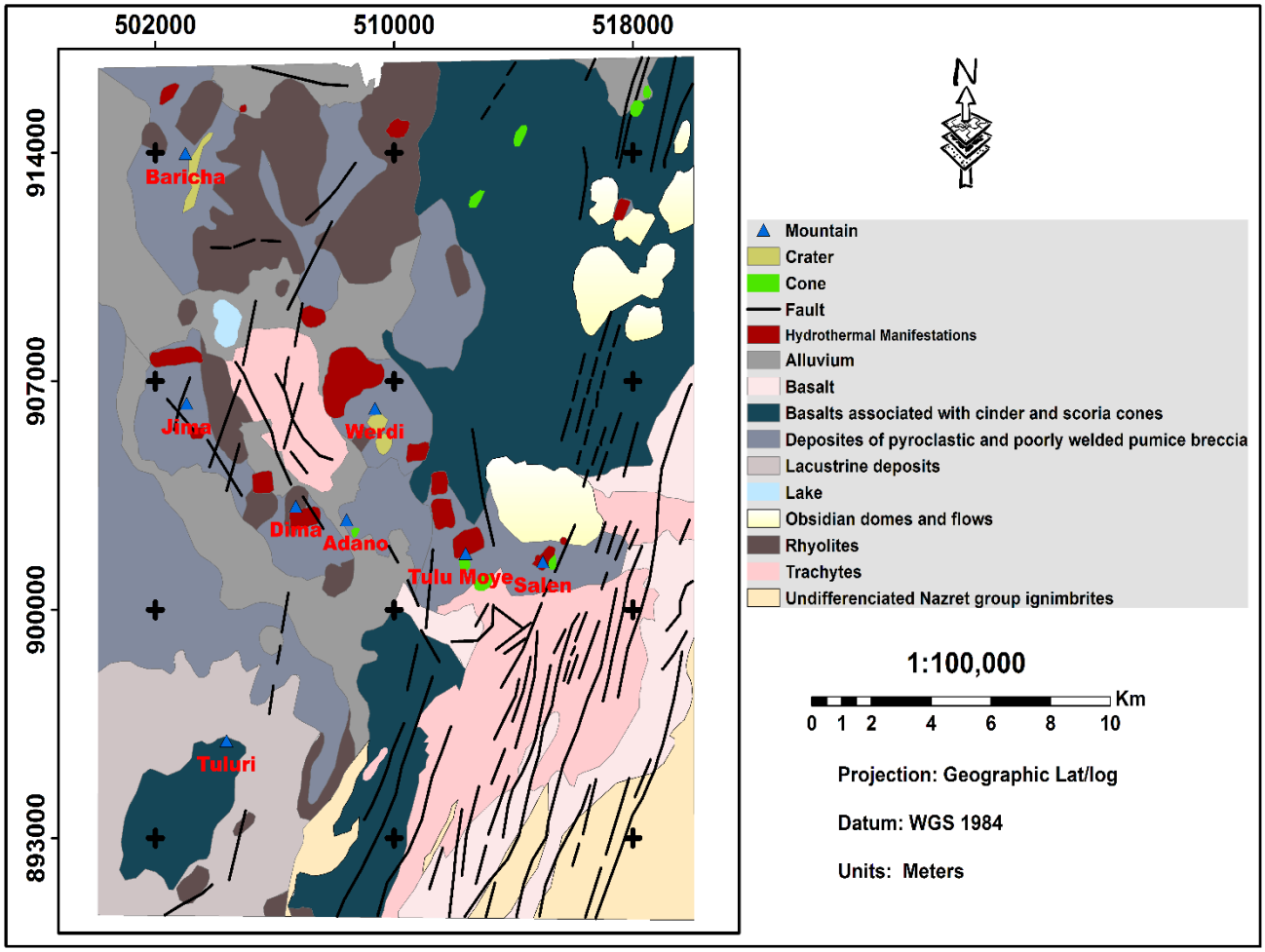

Figure 7: Geological map of Study Area. Extracted from Geological maps of Tulu Moye in scale 1: 50,000 and 1:20,000.

Rhyolites (QTr): In the study area there are numerous rhyolite center in the study area and in most cases they are fractured. They are concentrated in the center, northeast and north west of the associated with pumice breccia. Texturally, there arevariety of phenocrysts. Mojor constituent are phenocrysts of alkali feldspar (sandine) and microphenocysts of pyroxene (augite) quartz and amphibole (hornblende). Groundmass is mainly glass and sometimes opaque minerals, leucoxene and iron-oxides.

Older basalt (QWpb): They are mostly found in eastern and southern parts of the area. These are texturally fine-grained, sparsely porphyritic and porphyritic varieties. The Major constituent are plagioclase feldspars (labradorite-bytowanite), olivine (partially idingsitized) and pyroxene. The groundmass is mainly glass and plagioclase lath.

Older rhyolites (NQr): They are forming domes and in most cases are faulted. They are mainly exposed in the eastern part of the mapped area. They have porphyritic textured and sometimes aspheric. The major constituent are phenocrysts of alkali feldspars (sanidine) and pyroxene; and microphenocrysts of alkali-feldspar, quartz and pyroxene. The Groundmass is predominantly feldspars spherulites and iron-oxide (hematite). Ignimbrites of the nazret group (NQn) are exposed in the mapped area. They are poorly welded, top weathered but more or less fresh with different lithic fragments (pumice, rhyolite and basalt). They are mainly exposed on the eastern side of the area forming escarps (due to faulting). The major phenocrysts are sanidine, amphibole (hornblende) and microphenocrysts of hornblende, feldspar, quartz and iron oxide. The groundmass is mainly glass (sometimes there area fiammae).

Sedimentary Unit: these are cover mostly the lower depression of the rift. Exposed section of the unit contain fish ash, sand and clay. It shows alternate graded bedding (10 to 20 cm apart). It has been describe by many researcher ELC (1987, as cited in Ayele et al., 2002) that the sediment are wide spread in the central part of the Rift. They are considered to be 0.1 My old as this age suggested by Laury and Albritton (1975, as cited in Ayele et al., 2002).

Structural features

The Tulu Moye area is a part of rift system, is highly affected by the WFB Mohr (1967, as cited in Engdawork, 2007). WFB forms several segments of Quaternary volcanic-tectonic activities. Each segments of the axial zone is 80-120 km long and is displaced to the east for 10-30 km. This part of the segment which extends from the eastern shore of the lake Ziway up to Gedemisa caldera, consists of faults and open fractures trending NNE-SSE with 0.5 km spacing striking generally 20° north, and form horsts and grabens. Tulu Moye, including Bora, Berricha, and other volcanic complexes are in this segment.

The eastern part of tulu Moye is affected by NNE-SSE trending closely spaced normal swarms and open tensional fissures. This presently active axis of the rift structures. Mt. Bora and Berricha are characterized by NW-SE transverse normal faults. These transverse faults features intersect the NNE-SSW major faults.

Hydrothermal Activity

The distribution of hydrothermal manifestation is shown on figure 7. The study area is strongly affected by hydrothermal activity. The main hydrothermal manifestations in the area are weak

fumaroles, active steaming grounds and altered grounds. These manifestations area are mainly wide spread in the western and central part of the study area. They are aligned in NNW direction along the transverse faults. The manifestation extends from east of Tulu Moye to the south and north of Berecha volcanic complex. Most of the steaming and grounds are associated with weak fumarolic activity. There is a wide area of altered ground and steaming ground at the west central part, near Bite village having temperatures ranges from 70-80 ^{0}C. The Pyroclastic deposits are highly altered and changed to soft clay like material having various, whitish, brownish, reddish, and grey.

Based on their geographical distribution the hydrothermal activities around Tulu Moye are categorized in the following groups (Ayele et al., 2002).

Bekere Hydrothermal Field: Large hydrothermal altered area is found in the southern part of lake Koka at the adge of a rhylolite dome. It mainly follow NNW trending fault. It has weak fumaroles with temperature of up to 45 ^{0}C. The alteration product are various colored (whitish, reddish and yellowish) soft material.

Kechkechi Hydrothermal Field: There is an extensive area of hydrothermal altered zone around Kechkechi area (south of Bite village). It has active warm ground occurs and further climbing the hill there are chalcedony cover a large area. Fracture in highly fractured pumiceous ignimbrite exposure are sealed by silica. The chalcedony deposit mainly covers the top of the recent fall and flows. Mostly there are silicified fragments scattered.

Eleda Hydrothermal Field: It is located at Elada area (east of Bite village).it has very extensive area of fossil hydrothermal manifestation, which mostly follows the NNW trending structure zone. Surficial alteration include reddish and whitish clay materials.

Werdi Hydrothermal Field: Most of the werdi area has an extensive area of altered zone. The alteration zone is mostly warm ground and low pressure fumaroles at the foot hill and on top of volcano. The fumaroles range in temperature from 45 to 60 ^{0}C. The northwestern part of the volcano, the foothill region and the southeastern part of the volcano are mainly affected by the hydrothermal activity. There are silica (mainly chancedony), which cuts the rhyolite flow predominantly following the NNW strike direction.

Dima Hydrothermal Field: Around Dima area (south of Bite village), on top of a rhyolite dome there is small area of warm ground allighned along a NNE-SSW direction. Weak fumaroles occur with temperature close to 50 ^{0}C. East of Dima volcano there is an area of altered ground with main

alteration products of whitish and reddish soft material. South of Dima there phreatic explosion crater and its products are scattered.

Janno Hydrothermal Field the area lies northeast of study area around jano and it is small area altered zone with warm ground of temperature up to 40 ^{0}C.

Mt. Moye Hydrothermal field: The area has two volcanoes namely Tulu Moye Danise and Tulu Moye Terro. The area has been affected by hydrothermal activity and there is an extensive area of thermal manifestation characterized by surficial alteration that mainly include reddish clay and sometimes-yellowish material. There are fumaroles (ranging in temperature up to 90 ^{o}C) and warm ground in the area. The fumaroles give a hissing sound and are powerful.

3.1.4 Climate and Vegetation

Based on the meteorological data collected from the meteorological stations at Ziway, Kulumsa and Awash Melkasa towns during 1989, the study area and its surrounding are categorized into three main climatic zones. Namely, Temperate zone (Woina Dega), Warm zone (Kola) and semi- desert (Kefil Bereha) zone (Tesfaye et al., 1992). Most of study area falls within the Woina Dega climatic zone, having mean annual daily temperature of about 20 ^{0}C temperature and the mean night temperature is around 10 ^{0}C. The area also receives rain fall during the rainy season mainly between June and September. Based on two metrological station at Ogelecho and Kulumsa from National Metrological Agency (NMA) of Ethiopia in 2014. The mean annual rain fall of about 716 mm/yr, are indicated in figure 8.

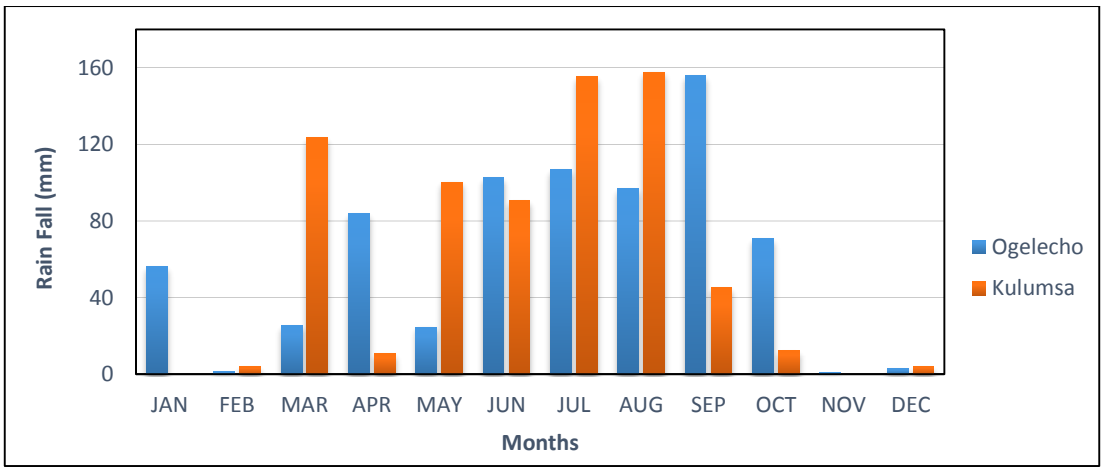

Figure 8: Mean monthly rainfall of metrological stations in 2014

The area is extensively deforested and the natural vegetation, where preserved, is covered mainly by shrubs, acacia and short bushes. There are thick vegetation on younger basalt and obsidian and scarce vegetation cover on pumice and ash falls and in gorges (Ayele et al., 2002).

3.1.5 Soil

According to FAO (Food and Agriculture Organization) in scale 1:5,000,000 digitized soil map of the World have three major types of soil in the study area. These are Lithosols, Eutric Nitosols and Haplic Xerosols. The detail pictorial representation of soil type is shown in the figure 9.

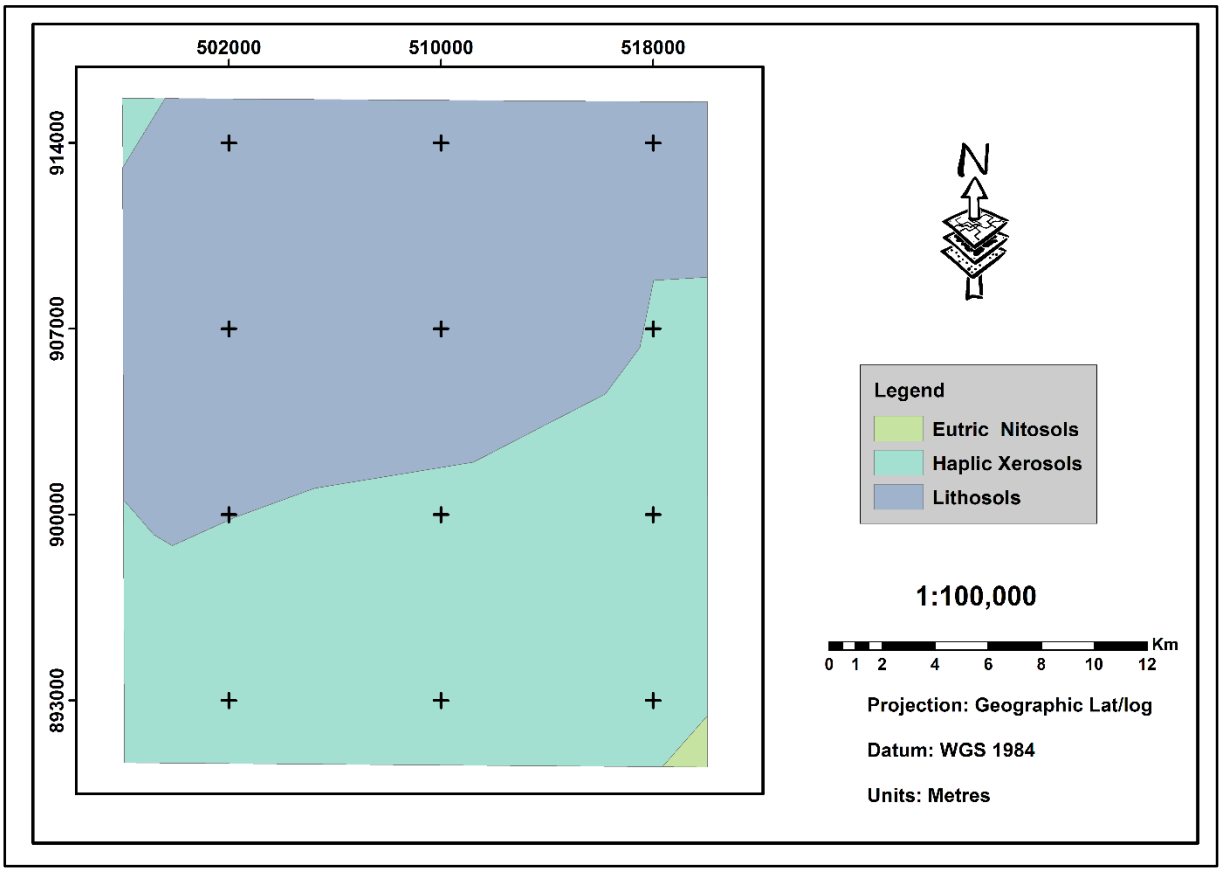

Figure 9: Soil map of Study Area. Source: Food and Agriculture Organization (FAO).

3.1.6 Population

The study area mainly consists of a number of villages, which area moderately populated. They depend on small-scale agriculture and cattle breeding. They are grow corn, teff, and beans. Ogolcho and Iteya town are closed to in the Study area. According to the recent population and housing censes report in a year 2007, a total population of surrounding towns Ogolcho and Iteya are 4,506 and 14,985 respectively (CSA, 2013).

3.1.7 Physiography and Drainage

The Tulu Moye geothermal prospect area is characterized by the occurrence of both mountainous and flat topography. Long and relatively narrow (1-5 m) extension fractures (Tesfaye Korme et al., 1997), brecciated lava flows, lava domes, cinder cones, crater and calderas are the most notable features within the study area. Three major volcanic centers (Tulu Moye, Bora and Berecha) represent the elevated topographies with altitude ranging from 2120-2266 m above sea level. However, Asela scarp and Chilalo of altitude about 4000 m is other topographical highs nearby the study area. Flat volcano sedimentary plains at an average altitude of 1700 m a.s.l (Above Sea Level) characterize the areas between the mountain ranges.

There are no perennial rivers crossing the area. However, wet season runoff from the mountains to the plains forms the seasonal lake called Bitte, in the central part of the area. The northern part of the area is actually bounded by Lake Koka. It is an artificial reservoir formed by awash river dam bounds the northern portion of the prospect.

3.2 Materials

3.2.1 Primary Data Source

The most popular form of primary raster data source used in Remote Sensing and GIS application is remotely sensed imagery (Lo and Yeung, 2002). Accordingly satellite images have been extensively utilized throughout this thesis as one of the most important primary data source. A Landsat 8 image for the study area is identified as path 168 and row 054. The data were obtained on October 17, 2014. According to two meteorological station at ogelecho and kulumsa, which are close to the study area. It receives moderate rain fall during October at the time of data acquisition as mentioned in figure 8. Date of data selection is considering the less heating influence from solar radiation on land surface. The daily level 3 LST product at 1km spatial resolution were used for validation of the Landsat-8 LST. It is conducted by comparing it with the MODIS LST product. In this work, version 5 of MODIS/Terra Land Surface Temperature and Emissivity (LST/E) - Daily L3 Global 1 km Grid products (MOD11A1) are downloaded from USGS.

The Shuttle Radar Topographic Mission (SRTM) data of NASA was the primary data used for slope and other topographic analysis. The data has a 30 meter resolution. In addition Ground Control Points (GCPs) were collect during field data gathering for the purpose of geo-referencing, image rectification and ground verification for the accuracy of geothermal anomaly detection. These and other location sensitive data was collected using Garmin 72 GPS satellite signal receiver.

3.2.2 Secondary Data Source

Topographic maps of the study area at the scale 1:50000 were obtained from the Ethiopian Mapping Agency (EMA). These maps were originally prepared from an aerial photo series acquired from 1986 and1987. In addition to this, Geological map of Tulu-Moye and Nazreth at scale of 1:50,000/1:20,000 and 1:250,000 respectively are used for mapping of geological and hydrothermal manifestation in the study area. Those data source was GSE.

Table 3: Types of materials and software used

S/N	Type	Description	Source
1	Maps	Topographic map of to the scale of 1:50,000	EMA
		Geological map of to the scale of 1:250,000	GSE
		Geological map of to the scale of 1:50,000	GSE
		Geological map of to the scale of 1:50,000	GSE
		Digital soil maps	FAO
		Study area, Towns and Wereda Shape files	CSA
2	Ancillary data	Location of Hydrothermal Manifestation Area.	GSE
		Collected GPS data (Hydrothermal Manifestation Area)	Field Survey / GSE
3	Image	Landsat 8 (30 meter Spatial Resolution)	USGS
		MODIS (1km Spatial Resolution)	https://lpdaac.usgs.gov/
		SRTM DEM (30 meter Spatial Resolution)	USGS
4	Software	ArcGIS 10.3, ERDAS IMAGINE 2014, ENVI 5.1, GPS Utilities	A.A.U, GIS Lab
5	Instruments	GPS (GARMIN 72), Digital Camera (12mp)	Rented

Rain fall of the study area was taken from NMA. Shapefiles of the study area and attribute data of road and its type, rivers and its type, existing town, and woreda boundary were taken from Central Statistics Agency (CSA) of Ethiopia. On the other hand, Digital Soil Map ware collected from Food and Agriculture Organization of United Nation. Other ancillary input data were used from different

government offices, field survey and observations, and focus group discussions which were undergone with geothermal explore experts.

Different materials and software have been used based on the relevance to different activities and processes towards the accomplishment of this study. Digital camera and GPS satellite receiver are among the materials used during field work for gathering primary date. In addition, topographic, geological, soil maps, satellite imagery and diverse ancillary data have been used. Generally, summary of materials used in this study are indicated in Table 3.

3.3 Methods

Finding Potential Geothermal area is very complicated phenomenon. It needs advanced technology, time and expertise. Because of these reasons, it could be very difficult for a private researcher to carry out the study under such time and financial constraints. However, in Geographical Information System (GIS) and remote sensing environment, there are some best alternative methods where an integrated remote sensing with thematic information to detect potential area and data visualization as well.

The major data considered from remotely sensed data is Landsat 8 thermal infrared. First, TIRS and OLI bands are applied radiometric calibration to convert the Digital Number (DN) recorded by the remote sensor into the at-atmosphere radiance. OLI bands are largely contaminated by the atmospheric conditions. Thus, atmospheric correction is required to retrieve the real surface parameters by removing the atmospheric effects, such as the absorption, upward emission and scattering of the radiation from the earth surface for radiance. Satellite TIRS sensors measure TOA radiances, which can then be converted to TOA brightness temperatures using Planck's equation.

The knowledge of surface emissivity is important in reducing the error in estimation of LST from satellite data. Emissivity measurement is obtained from NDVI Threshold based method. NDVI ware derived from atmospherically corrected band 4 and 5 data. This result used as an input to drive fractional vegetation cover. It is the most important parameter to measure surface emissivity from remotely sensed data.

Split Window (SW) Algorithm was used to map the land surface temperature of the area. And then, the comparison of measured radiance was applied with MODIS land surface temperature data to validate LST result of Landsat 8.

As field surveying is one of the most important constituent of primary data collection, field investigation was made twice throughout the research time. During the first visit Global Positioning System (GPS) records were gathered for Geo-referencing the toposheet. On the second field work sample points was collected for field verification. Finally ground verification was made for final Geothermal Map. Pictorially, the overall methods and procedure applied in this study are indicated in the flow chart presented in the Figure 10.

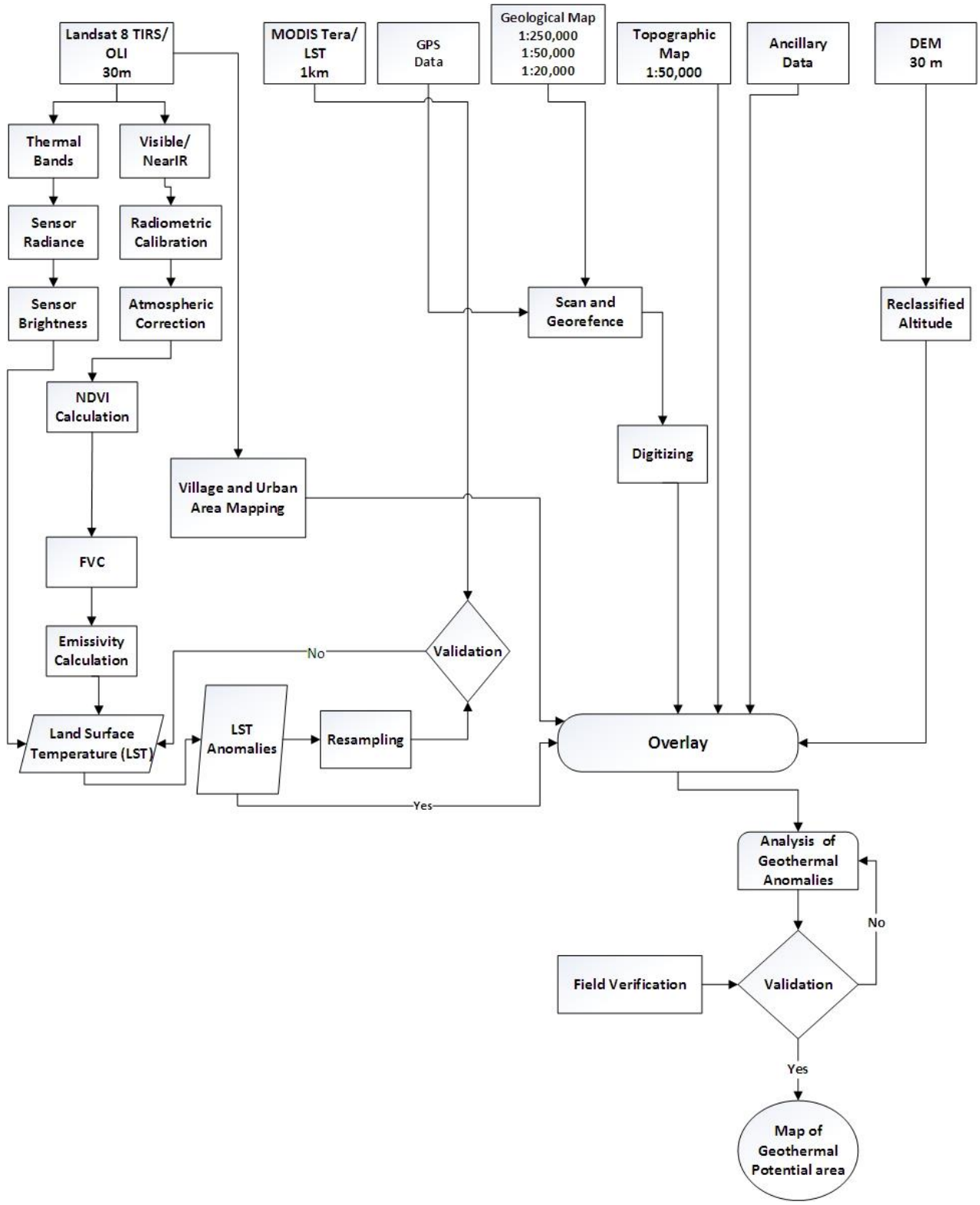

Figure 10: Methodology flow chart.

3.3.1 Preprocessing

Image data may have either radiometric or geometric or both type of distortion. These distortions could be caused by sensor and plate form errors during data acquisition. Therefore, before any analytical processing on satellite image, it has to be corrected for these distortions. This pre-processing operation is called image restoration or rectification (Thomas and Ralph, 1994). Atmospheric correction and radiometric calibration was made for red, near infrared and thermal infrared bands . Geometric correction already done by service provider of USGS for L1T data type which is orthorectified (Terrain corrected).

Radiometric Calibration

To begin with, radiometric calibration is applied to convert the DN recorded by the remote sensor into the at-atmosphere radiance. In this paper, radiometric calibration is carried out according the following standard LMin and LMax spectral radiance scaling factors equation (USGS, 2015). The following equation 11 developed by the USGS is generally used to compute the spectral radiance from DN value of OLI and TIRS data of Landsat 8: The Thermals of band 10 and 11 and visible to shortwave infrared bands of 4 and 5 data's stored as DN values were initially converted to spectral radiance values.

$$L_\lambda = M_L * Q_{cal} + A_L \ldots\ldots\ldots\ldots\ldots\ldots\ldots Eq.11$$

L_λ = Spectral radiance ((W/(m^2 * sr * μm)).

M_L = Radiance multiplicative scaling factor for the band (RADIANCE_MULT_BAND_n from the metadata).

AL = Radiance additive scaling factor for the band (RADIANCE_ADD_BAND_n from the metadata).

Qcal = Level 1 pixel value in DN.

The scene calibration data are usually available on the metadata file of each Landsat scene. The following table lists two sets of M_L and A_L for band 4, 5, 10 and 11 from metadata file of an image.

Table 4: LANDSAT 8 Radiance Scale Factors

Radiance Scaling Factors		
Band Number	M_L	AL
Band 4	0.010058	-50.28841
Band 5	0.006155	-30.77400
Band 10	0.0003342	0.1
Band 11	0.0003342	0.1

Atmospheric Correction

In the solar spectrum, sensors on meteorological or Earth remote sensing satellites measure the radiance reflected by the atmosphere-Earth surface system illuminated by the sun. This signal depends on the surface reflectance, but it is also perturbed by two atmospheric processes, the gaseous absorption and the scattering by molecules and aerosols. In the actual case, the signal is perturbed by the atmosphere. Only a fraction of the photons coming from the target reaches the satellite sensor, typically 80% at 0.85 μm and 50% at 0.45 μm, so that the target seems less reflecting. The missing photons are lost through two processes: absorption and scattering. Some photons are absorbed by aerosols or atmospheric gases other are scattered.

The at-atmosphere radiance is largely contaminated by the atmospheric conditions. Thus, atmospheric correction is required to retrieve the real surface parameters by removing the atmospheric effects, such as the absorption, upward emission and scattering of the radiation from the earth surface.

6S is the latest and sophisticated model with options for different satellite sensors (Vermote et al. 1997b). The model can simulate the solar radiation on the ground and in the atmosphere from 0.2 μm to 4.0 μm spectral range under a variety of conditions of both ground surface and atmosphere (Vermote et al., 1997b). Giving the radiance from TOA, viewing geometry and the atmosphere related parameters the model can estimate the reflectance or radiance on the ground, and atmospheric absorption and scattering characteristics. These parameters can be used for atmospheric correction of satellite remote sensing data.

The minimum data set needed to run the 6S model is the meteorological visibility, type of sensor, sun zenith and azimuth angles, date and time of image acquisition, and latitude-longitude of scene center. Those parameters has got from metadata file of an image.

In this study we have proceeded to correct the two multispectral bands by defining the geometry of the satellite observation, viewing angle and other necessary data set. Using the input data and the embedded features, the model produces variables to assess the surface reflectance. The true reflectance value ρλ is obtained from the model output by the following equation.

$$\rho_\lambda = \frac{y}{1+(x_c+y)} \dots\dots\dots\dots\dots\dots\dots Eq.12$$

$$y = (x_a + L_\lambda) + x_b \dots\dots\dots\dots Eq.13$$

where ρλ is the corrected reflectance, Xa, Xb, and Xc are the coefficients obtained from the model (Xa is the inverse of the transmittance, Xb is the scattering term of the atmosphere and, Xc is the reflectance of the atmosphere for isotropic light), and Lλ is the observed radiance (w/m2*sr*μm).

3.3.2 Retrieval of Normalized Difference Vegetation Index (NDVI)

Remote sensing phenology studies use data gathered by satellite sensors that measure wavelengths of light absorbed and reflected by green plants. Landsat 8 measure red and near-infrared light waves reflected by land surfaces. NDVI derived from the visible near-Infrared bands. NDVI is an indicator that describes the greenness — the relative density and health of vegetation. NDVI values range from +1.0 to -1.0, areas of barren rock, sand, or snow usually show very low NDVI values (for example, 0.1 or less) (Sobrino and Raissouni, 2000). Sparse vegetation such as shrubs and grasslands or senescing crops may result in moderate NDVI values (approximately 0.2 to 0.5). High NDVI values (approximately 0.6 to 0.9) correspond to dense vegetation such as that found in temperate and tropical forests or crops at their peak growth stage.

Atmospherically corrected OLI band 4 (red) and 5 (near-infrared) were layer stacked and NDVI was calculated using Algorithm shown in equation 14. This data used for input to drive fractional vegetation cover.

$$NDVI = \frac{NDVI\ 5 - NDVI\ 4}{NDVI\ 5 + NDVI\ 4} \dots\dots\dots\dots\dots\dots\dots Eq.14$$

3.3.3 Estimation of Fractional Vegetation Cover (FVC)

Vegetation Fraction is defined as the percentage of vegetation occupying the ground area in vertical projection in per unit area. It's a comprehensive quantitative index in forest management and vegetation community cover conditions, and it's also an important parameter in many remote

sensing models such as NDVI^{THM} method in emissivity study. It can be derived from NDVI according to equation 15 (Carlson and Ripley, 1997) (Sobrino and Raissouni, 2000). The proportion of vegetation cover, Pv, for each pixel through satellite data is calculated using the following formula.

$$Pv = \left(\frac{NDVI - NDVI_s}{NDVI_v - NDVI_s}\right)^2 \ldots\ldots\ldots\ldots\ldots\ldots\ldots\ldots \text{Eq. } 15$$

Based on NDVI image obtain from above, Pv is extracted from NDVIv and NDVIs. Where NDVIv and NDVIs represents the NDVI of vegetation and soil, respectively. Over particular areas, NDVIv and NDVIs values can be extracted from the NDVI histogram.

3.3.4 Estimation of Land Surface Emissivity (LSE)

Different approaches have been used to predict LSE from NDVI values (Van de Griend and Owe, 1993). In this paper used the NDVI^{THM} method, which is first introduced by and applied to Advanced Very High Resolution Radiometer (AVHRR) data (Sobrino and Raissouni, 2000), and later compared with other methods and adapted to other sensors, all possibility methods are mentioned in chapter 2. NDVI^{THM} uses certain NDVI values (thresholds) to distinguish between soil pixels (NDVI < NDVIs) and pixels of full vegetation (NDVI > NDVIv). For those pixels composed of soil and vegetation (mixed pixels, NDVIs ≤ NDVI ≤ NDVIv), the method uses the following simplified equation 16 in this study. Detail explanation of NDVI^{THM} method is found in chapter 2.

$$\varepsilon_\lambda = \varepsilon_{v\lambda} p_v + \varepsilon_{s\lambda}(1 - p_v) + c_\lambda \quad \ldots\ldots\ldots\ldots\ldots Eq. 16$$

where ε_v and ε_s are, respectively, the soil and vegetation emissivity, *P*V is the proportion of vegetation (also referred to as fractional vegetation cover, FVC), it was retrieved from NDVI according to above equation 4.5 and *C* is a term which takes into account the mean cavity effect due to surface roughness (*C* = 0 for flat surfaces). Using the geometrical model proposed (Sobrino et al., 2008). The cavity term for a mixed area and near-nadir view like the study area is given by:

$$C_\lambda = (1 - \varepsilon_s) * \varepsilon_{v\lambda} F'(1 - p_v) \ldots\ldots\ldots\ldots\ldots Eq. 17$$

Where C_λ is the contribution of multiple scattering caused by the internal geometric structure of the pixel for specific bands. F' is a geometrical factor ranging between zero and one, depending on the geometrical distribution of the surface. Since *F'* cannot be estimated from VNIR/TIR remote-

sensing data, a mean value is generally chosen (Sobrino and Raissouni, 2000). Whose mean value, assuming different geometrical distributions, is 0.55. Emissivity soil and vegetative values for band 10 and 11 of the corresponding bands are obtained from table 5 (Jiménez-Muñoz et al., 2014). After generating cavity effect for band 10 and 11, the mean cavity was obtained for each of bands from the cavity histogram. Its result used for input to calculate Emissivity.

Table 5: Emissivity value of vegetation and soil

Emissivity	Band 10	Band 11
E_s	0.971	0.977
E_v	0.987	0.989

LSE measure the inherent characteristic of earth surface. It measure its ability to convert thermal or heat energy into radiant energy. LSE estimation required emissivity of soil and vegetation of both Band 10 and 11 are given in Table 5. After generating LSE for both bands of TIR, the mean and difference LSE was obtained from as shown in equation 16 and 17 (Sobrino et al., 2008). Those two data sets are very important parameters to calculate LST.

$$\varepsilon_M = \frac{\varepsilon_{10} + \varepsilon_{11}}{2} \quad \ldots\ldots\ldots\ldots\ldots\ldots\ldots\ldots\ldots\ldots\ldots\ldots Eq.18$$

$$\Delta\varepsilon = \varepsilon_{10} - \varepsilon_{11} \quad \ldots\ldots\ldots\ldots\ldots\ldots\ldots\ldots\ldots\ldots\ldots\ldots Eq.19$$

Where ε_M – Mean LSE

$\Delta\varepsilon$ – LSE difference and ε_{10} and ε_{11} - LSE of band 10 and 11

3.3.5 Sensor Brightness Temperature

Brightness temperature (TB) is the microwave radiation radiance traveling upward from the top of Earth's atmosphere. The calibration process has been done for converting thermal DN values of thermal bands TIR (band 10 and 11) to TB. For finding TB of an area the TOA spectral radiance of ($L\lambda$) was needed which was calculated in above equation 18. TB for both the TIRs bands was calculated by adopting the following formula (USGS, 2015):

$$T = \frac{K2}{ln\left(\frac{K1}{L_\lambda} + 1\right)} \ldots\ldots\ldots\ldots\ldots\ldots\ldots Eq\ 20$$

Where, K1 and K2- thermal conversion constant and it varies for both TIR bands (table 6)

Lλ – Top of Atmospheric spectral radiance (Watts/(m^2 * sr * μm)).

T = Top of Atmosphere Brightness Temperature, in Kelvin.

Table 6: Thermal constant value of K1 and K2

Thermal Constant	Band 10	Band 11
K1	774.89	480.89
K2	1321.08	1201.14

3.3.6 Land Surface Temperature Calculation

The main difference between the new TIRS and previous TM/ETM+ sensors (apart from differences related to sensor design) is the presence of two TIR bands in the atmospheric window between 10 and 12 μm, which represents an advancement over the single thermal band present on TM and ETM+ sensors. Since the previous single band has been split into two TIR bands, the bandwidths of TIRS bands are narrower than the previous TM/ETM TIR band. The presence of two TIR bands opens the possibility to apply SW algorithms instead of SC algorithms for LST retrieval.

The SW technique uses two TIR bands typically located in the atmospheric window between 10 and 12 μm. The basis of the technique is that the radiance attenuation for atmospheric absorption is proportional to the radiance difference of simultaneous measurements at two different wavelengths, each of them being subject to different amounts of atmospheric absorption. The SW algorithm proposed in this letter is based on the mathematical structure proposed by Sobrino et al., (1996) and applied to different Earth Observation sensors (Sobrino et al., 2008).

The main advantages of this algorithm are the following: 1) It is a physics-based algorithm, since it is obtained from the radiative transfer equation (RTE) applied to two different bands; 2) it takes into account both emissivity and water vapor effects; 3) it includes both LST and Sea surface temperature (SST) cases; and 4) it is totally operational (Sobrino et al., 2008).

LST was calculated by applying a structured mathematical algorithm using ENVI 5.1 band math tool, SW algorithm. It uses brightness temperature of two bands of TIR, mean and difference in land surface emissivity for estimating LST of an area. The algorithm is shown in equation 22.

$$T_s = T_i + c_1(T_i - T_j) + c_2(T_i - T_j)^2 + c_0 + (c_3 + c_4 W)(1 - \varepsilon) + (c_5 + c_6 W)\Delta\varepsilon \dots\dots\dots\dots\dots Eq.22$$

Where T_S is LST in kelvin, T_i and T_j are the at-sensor brightness temperatures at the SW bands i and j (in kelvin), ε is the mean emissivity, $\varepsilon = 0.5(\varepsilon_i + \varepsilon_j)$, Δε is the emissivity difference, $\Delta\varepsilon = (\varepsilon_i - \varepsilon_j)$. W is the total atmospheric water vapor content (in grams per square centimeter), the value of water vapor (W) content was retrieved from 6s model. It can generate a value of W based on some input parameter such as metrological visibility, date, month and location of data acquisition. Its value is 4.12 g/cm^2. C_0−C_6 are the SW coefficients value from table 7.

Table 7: Split-Window Coefficient values. source: Skokovic et al., 2014

Constant	Value
C_0	-0.268
C_1	1.378
C_2	0.183
C_3	54.3
C_4	-2.238
C_5	-129.2
C_6	16.4

3.3.7 Geothermal Anomaly Detection

If one were to drill a very deep well from the surface into the earth and were to measure the temperature as a function of depth, one would find a fairly constant increase of about 3 ^{0}C for each 100 m of depth. This rate is typical in normal areas, but there are anomalous regions associated with volcanic or tectonic activity where the temperature gradients far exceed these normal values (Ronald, 2005). Good geothermal prospects occur where the thermal gradient is several times greater than normal. A rise of 0.5 ^{0}C over the normal background would be the result of a heat flux about 50 times greater than the normal heat flux (Ronald, 2005).

A study of Qin et al., (2011) detect geothermal anomalous area with temperature about 4-10 K higher than background area. In this study, Land Surface Temperature with higher value is selected for further heat source analysis, geological structure analysis and false anomaly detection were considered.

4. Results and Discussion

4.1 Radiometric Calibration

The result of the thermal infrared image of the band 4, 5, 10 and 11 in which converted to the radiance as shown in Figure 11 and Figure 12. The radiance computed for band 4 ranges from 10.93 to 173.82 with mean 38.99 and standard deviation 11.34. Radiance for band 5 ranges from 11.74 to 151.88 with mean 80.34 and standard deviation 12.99. For that of TIRS band 10 it ranges from 8.31 to 10.78 with a mean 9.56 and standard deviation 0.36. Finally, radiance computed for band 11 ranges from 7.73 to 9.51 with a mean 8.64 and standard deviation 0.25.

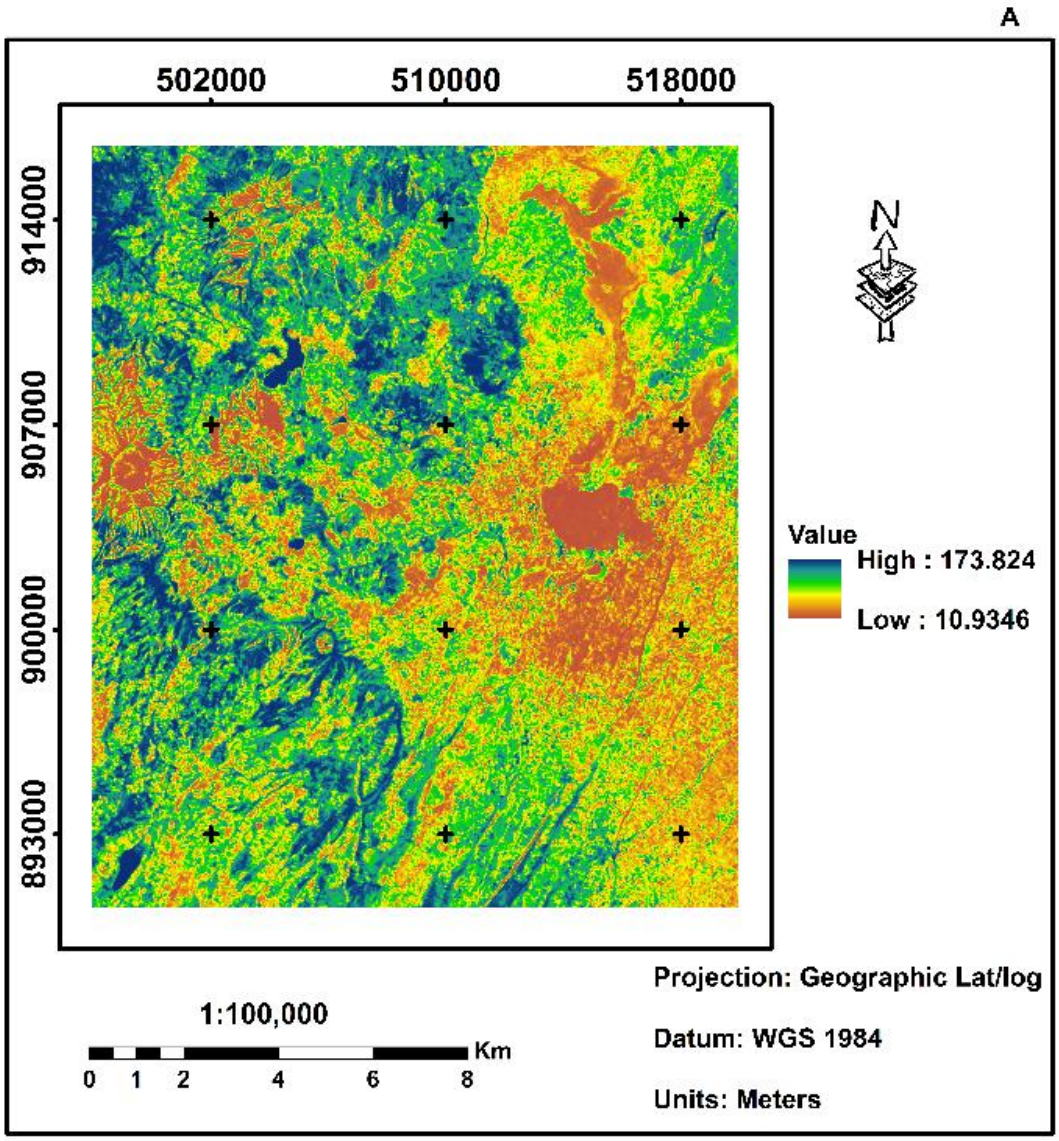

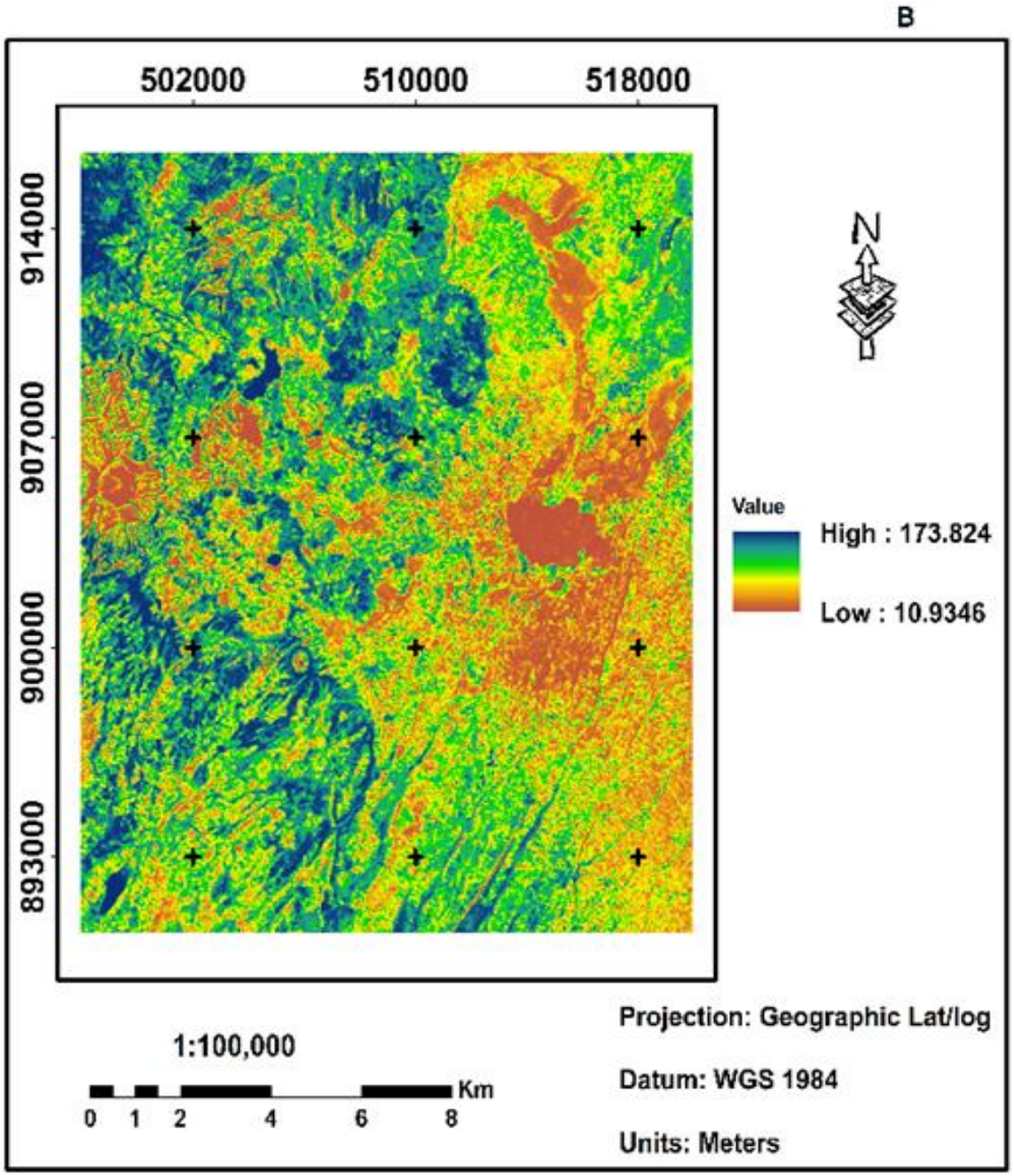

Figure 11: Radiance map of study area for band 4(A) and 5 (B)

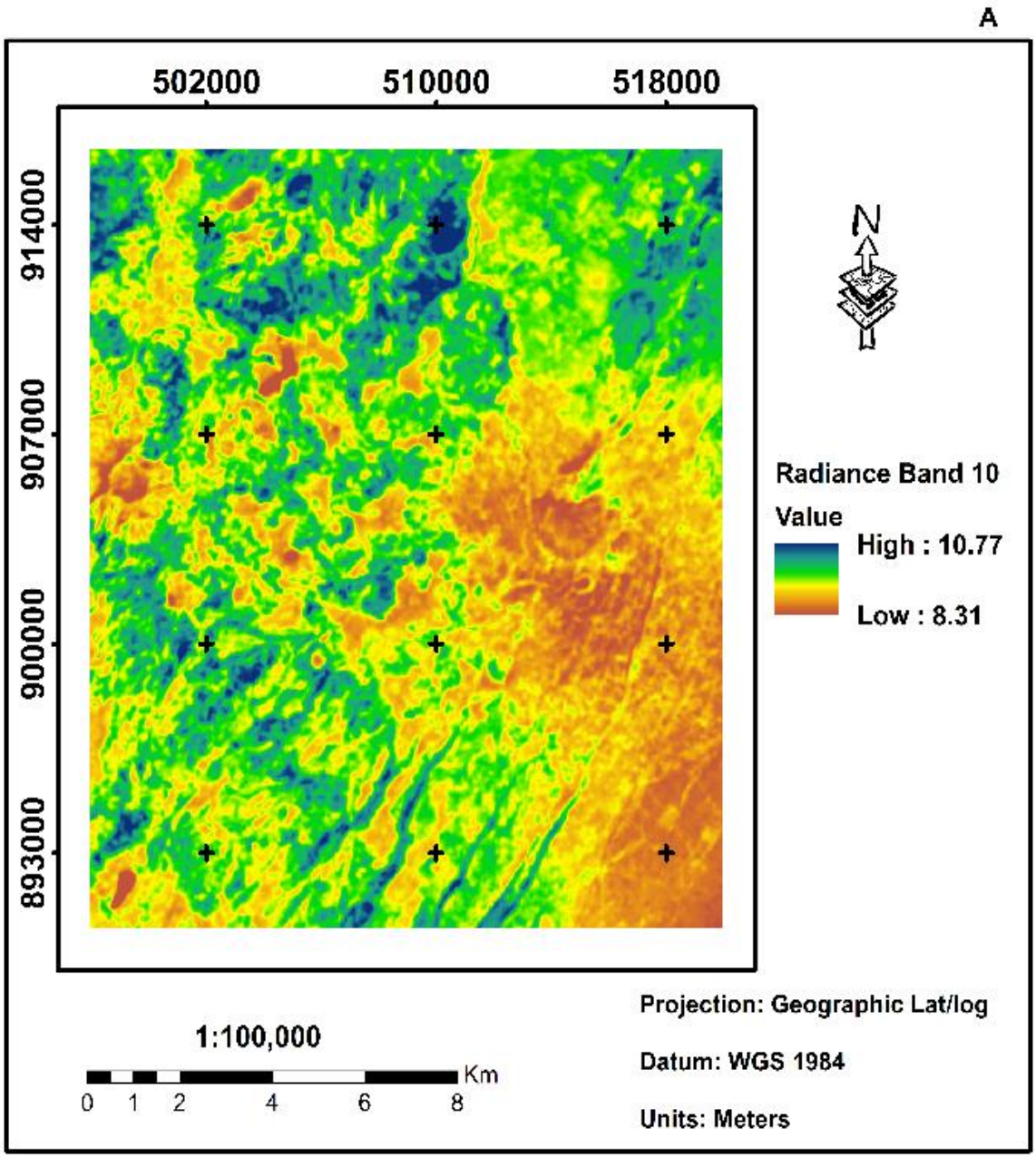
A
502000
510000
518000
914000
907000
900000
893000
N
Radiance Band 10
Value
High : 10.77
Low : 8.31
1:100,000
0 1 2 4 6 8
Km
Projection: Geographic Lat/log
Datum: WGS 1984
Units: Meters

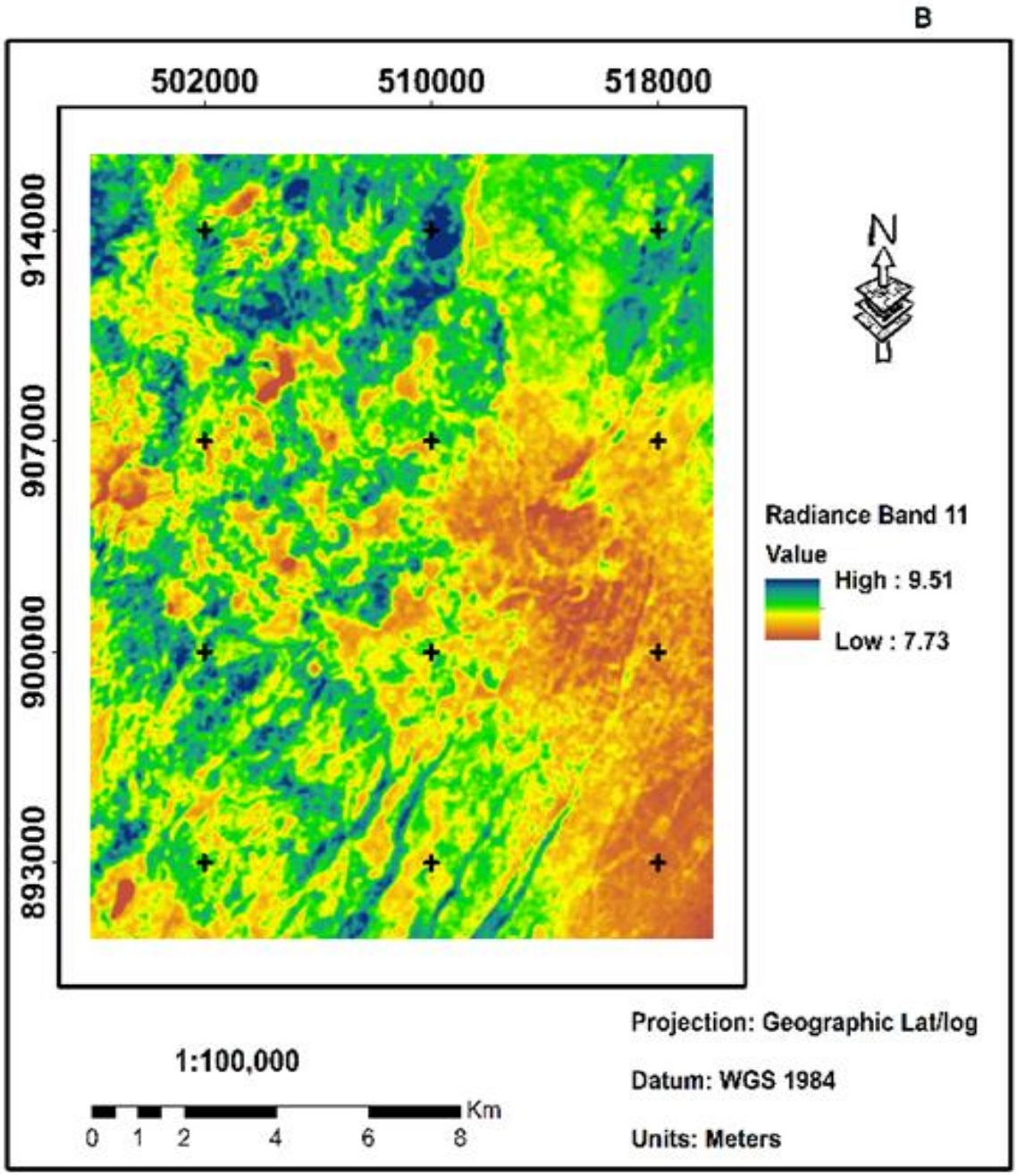

Figure 12: Radiance map of study area for band 10 (A) and 11 (B).

4.2 Atmospheric Correction

From 6S model, which is used to remove atmospheric problem, the Landsat 8 data of the forth band (red band) and fifth band (near infrared band) bands. Correction coefficient derived from 6S model results are listed in Table 8. ENVI 5.1 band math tool were used to convert radiance to reflectance, the result image has shown in figure 13. Computed result reflectance value for red band ranges from

0.001 to 0.468 with the mean of value 0.08. Result for near infrared ranges from 0.035 to 0.612 with the mean of value 0.08.

Table 8: 6S atmospheric correction coefficient

Bands	Coefficient of Xa	Coefficient of Xb	Coefficient of Xc
Band 4	0.00266	0.02783	0.07723
Band 5	0.00393	0.01242	0.04648

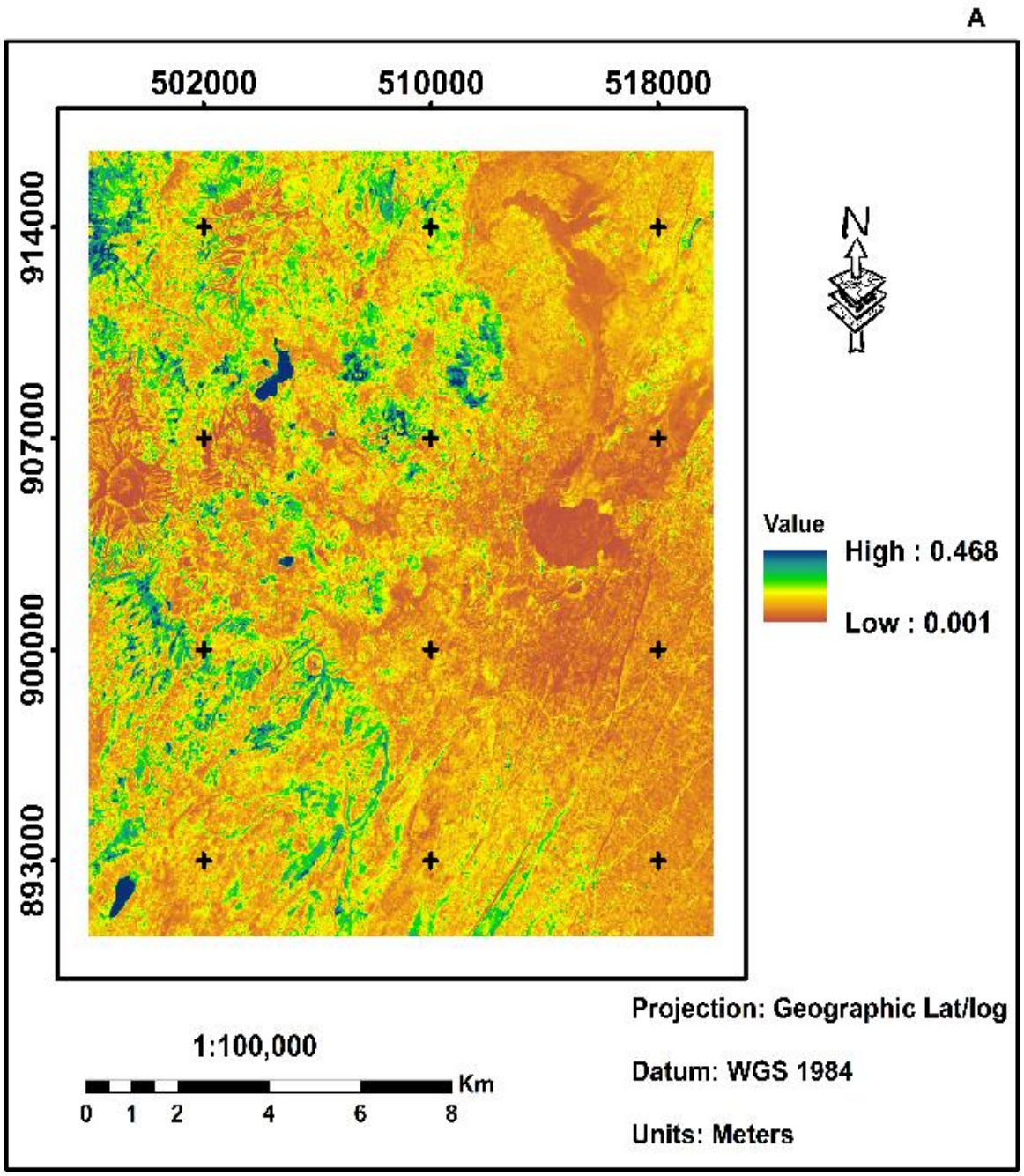
A
502000
510000
518000
914000
907000
900000
893000
N
Value
High : 0.468
Low : 0.001
1:100,000
0 1 2 4 6 8
Km
Projection: Geographic Lat/log
Datum: WGS 1984
Units: Meters

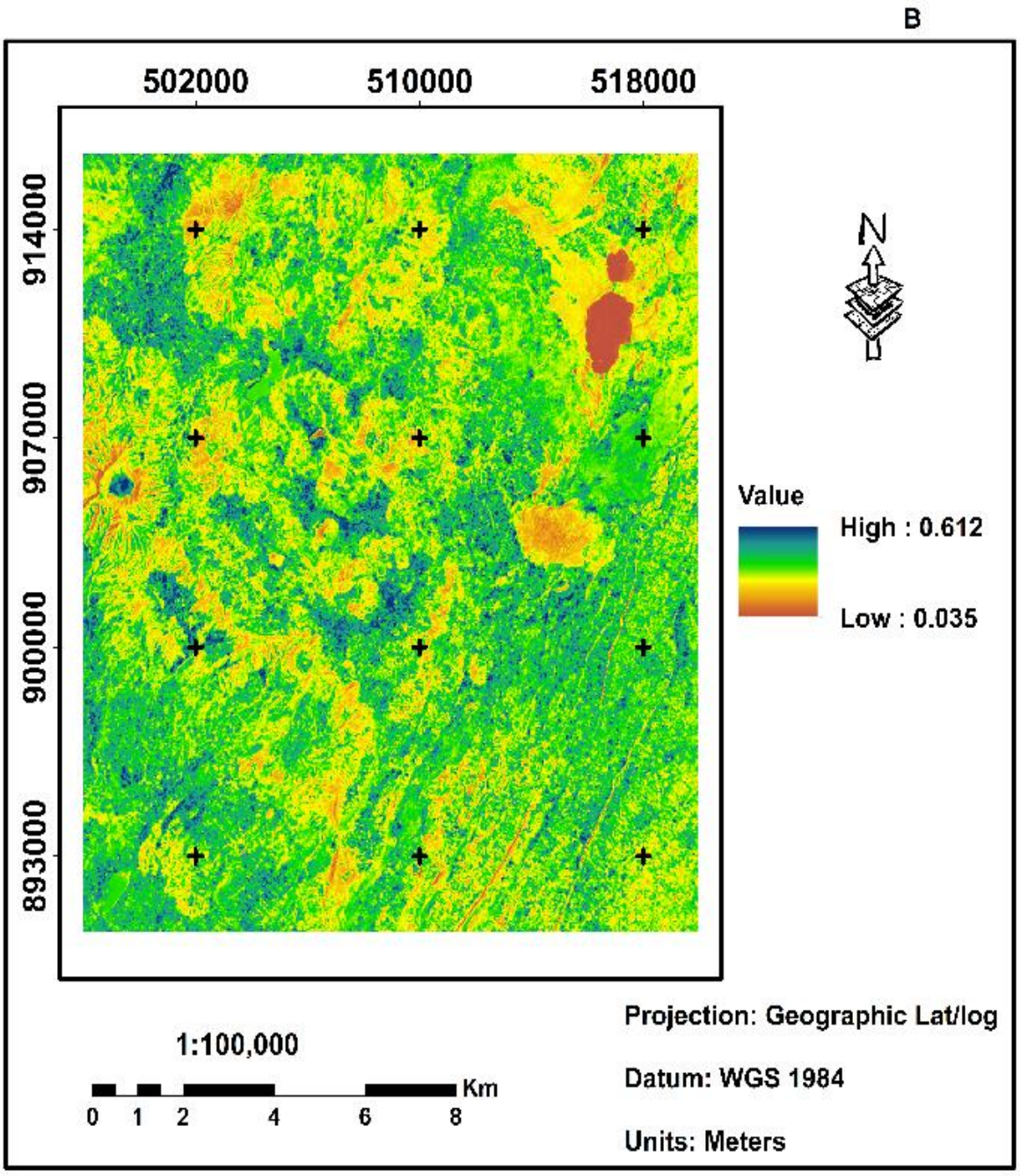

Figure 13: Reflectance map of study area for Band 4 (A) and 5 (A).

4.3 Normalized Difference Vegetation Index (NDVI)

The output value of NDVI ranged between -0.16 and 0.96 (Figure 14-A). The low value of NDVI represent by red color with no vegetation whereas area with water body have negative value. Whereas the higher value, represents as green color is highly vegetated area. The lowest positive value of study area are less vegetated soils. Because, refection from the soil is high, and produce low values in NIR band and high value in red band. NDVI with 0.9 (NDVIv) and NDVIs with 0.2

(NDVIs) extracted from NDVI histogram values (Table 9) were used for the analysis as the most important input to derived FVC.

Table 9: NDVI histogram values of study area

Band	Min NDVI	Max NDVI	Mean	SD	Approximate NDVIs	Approximate NDVIv
Band 1	-0.16	0.96	0.590918	0.139871	0.2	0.9

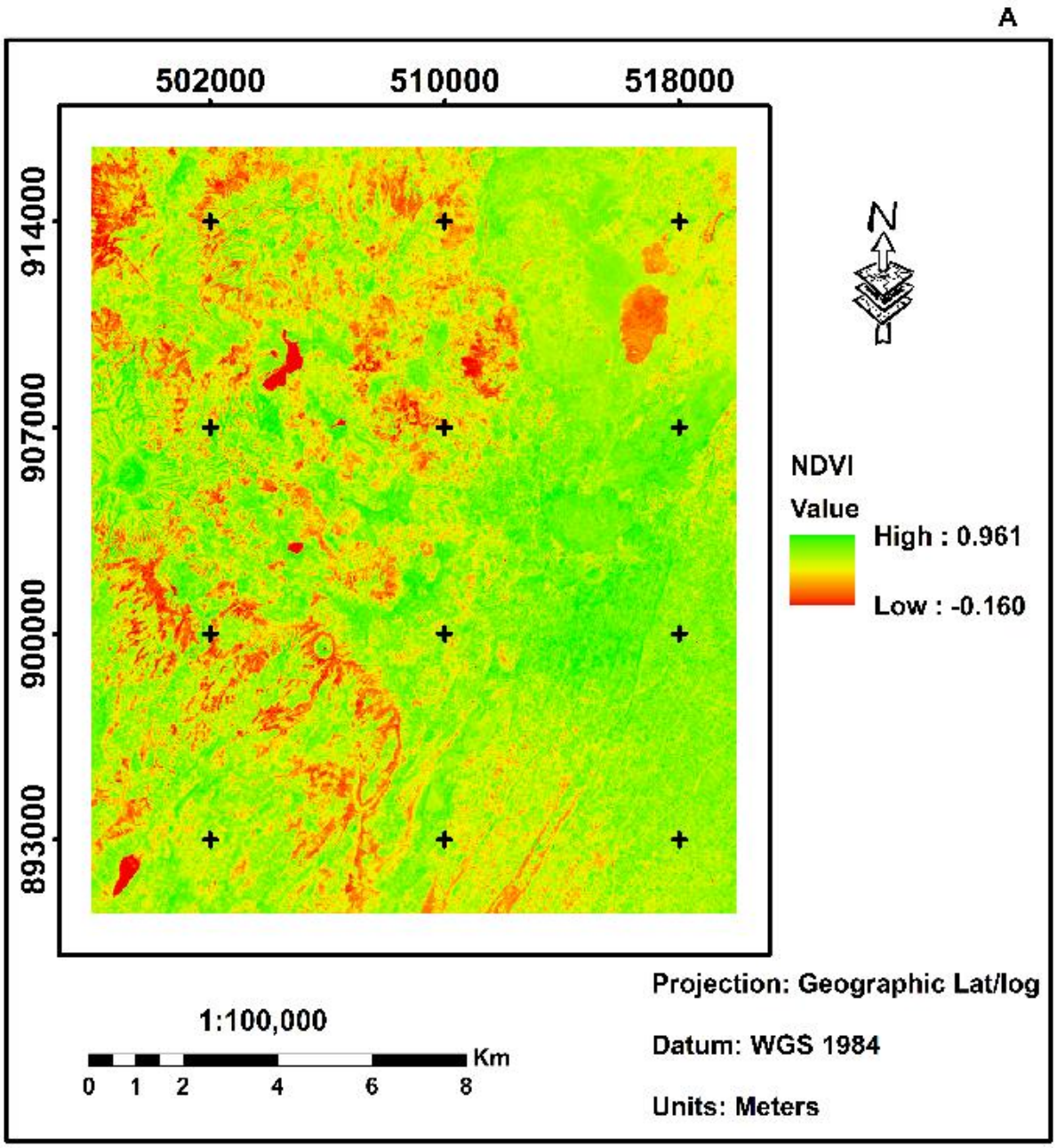

Figure 14: NDVI map of study area.

4.4 Fractional Vegetation Cover (FVC)

Vegetation fraction of the study area as shown in figure 15. It represent the area in terms of percentage in vertical projection of vegetation in per unit area. The result value range from 0 to 96 %. Zero means the area is covered by soil and 96 means the area is densely covered by vegetation/forest. Value in between 0 to 96 % represents the extent of vegetation occupying the

ground area in vertical projection. Vegetation coverage increase in the higher altitude, whereas the area of low altitude the vegetation coverage decreased.

Cavity effect into account due to the surface roughness. Estimated cavity effect for mixed area and near- nadir view is listed the following table.

Table 10: Cavity effect Value of band 10 and 11

Band	Min	Max	Mean
Band 10	0	0.016	0.011
Band 11	0	0.013	0.009

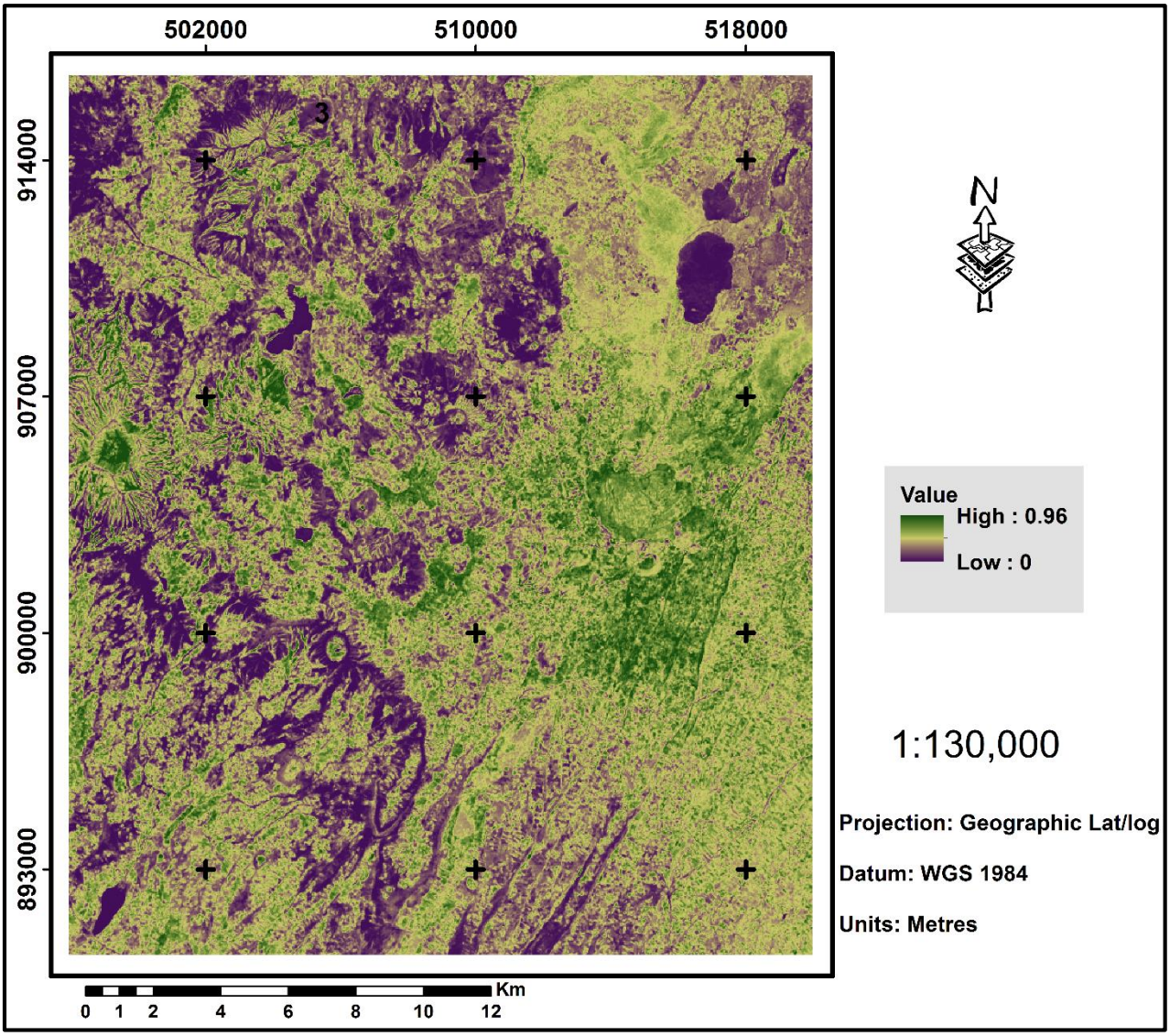

Figure 15: The percentage of the vertical projection of vegetation canopy map of study area

4.5 Land Surface Emissivity (LSE)

Mean of Land Surface Emissivity was created using NDVI threshold technique (Figure 16). The LSE of Tulu Moye area ranged between 0.984 and 0.998 with average value 0.988. Highly elevated regions in the area had more vegetative cover, hence LSE was high in these regions. High LSE was found in east to west parts of the study area, whereas low LSE was noticed in northwest and southwest of the study area. Difference of LSE was calculated which is one of important parameter to obtain LST using SW algorithm. In both emissivity results, the highest emissivity is shown in the area where there is dense vegetation.

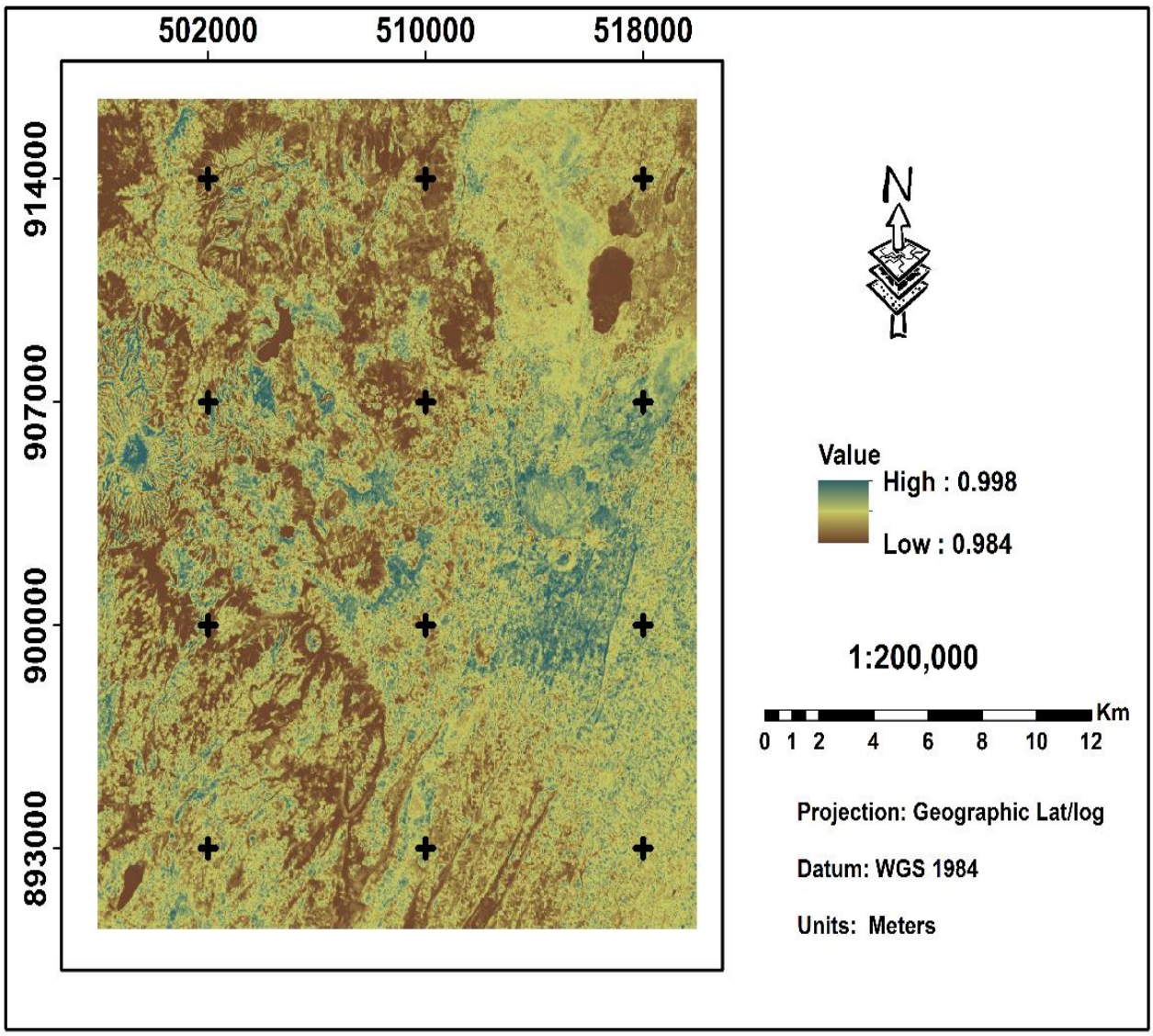

Figure 16: Mean of Land surface emissivity map of study area.

4.6 Sensor Brightness Temperature

The result at satellite temperature ranges from 290.59 to 308.01 ^{o}K with a mean of 299.3 ^{o}K and standard deviation 3.052 ^{o}K for band 10 (Figure 17-A). Value ranges from 289.71 to 304.67 ^{o}K with a mean of 297.19 ^{o}K and standard deviation 5.24 for band 11 (Figure 17-B)

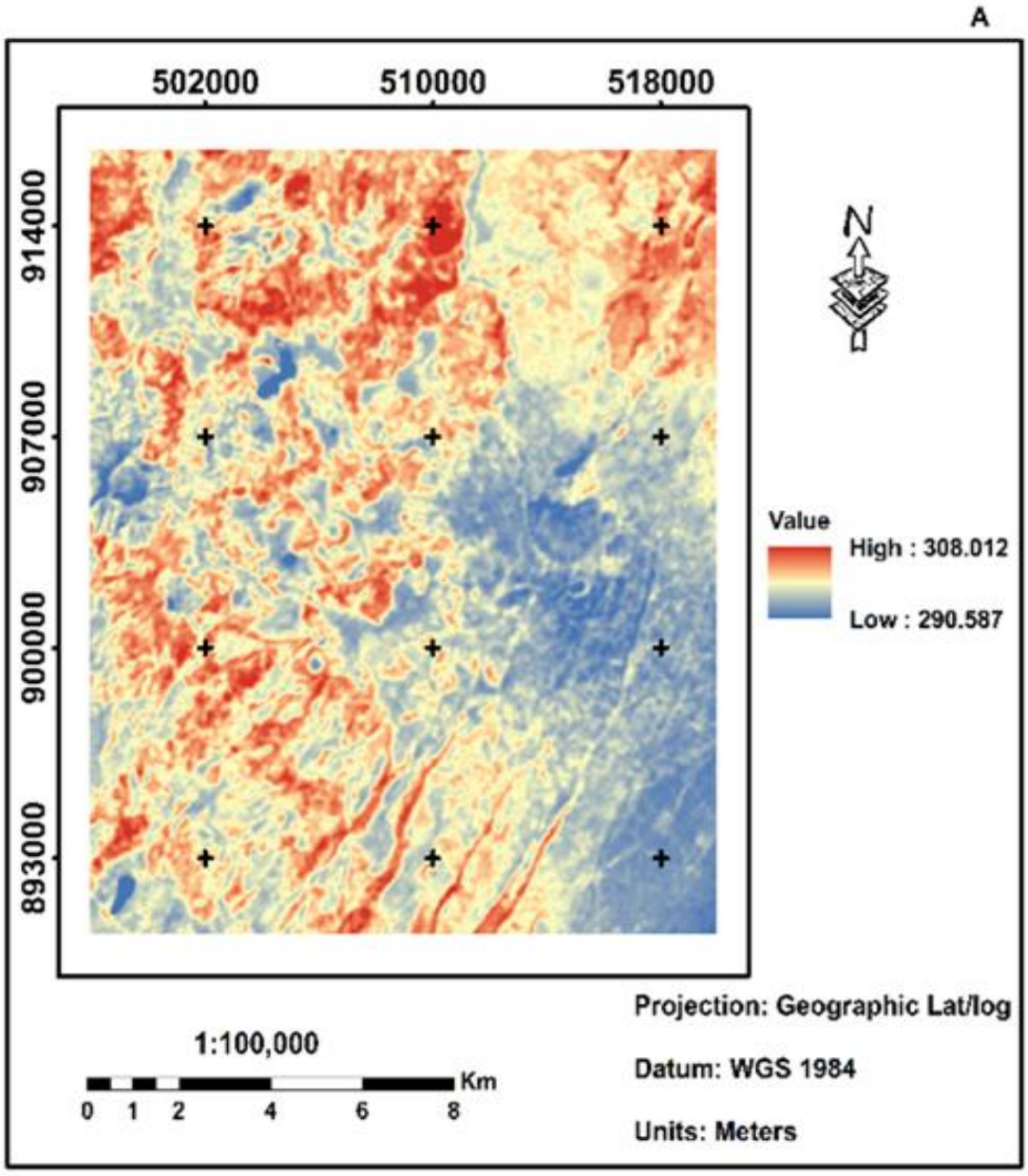

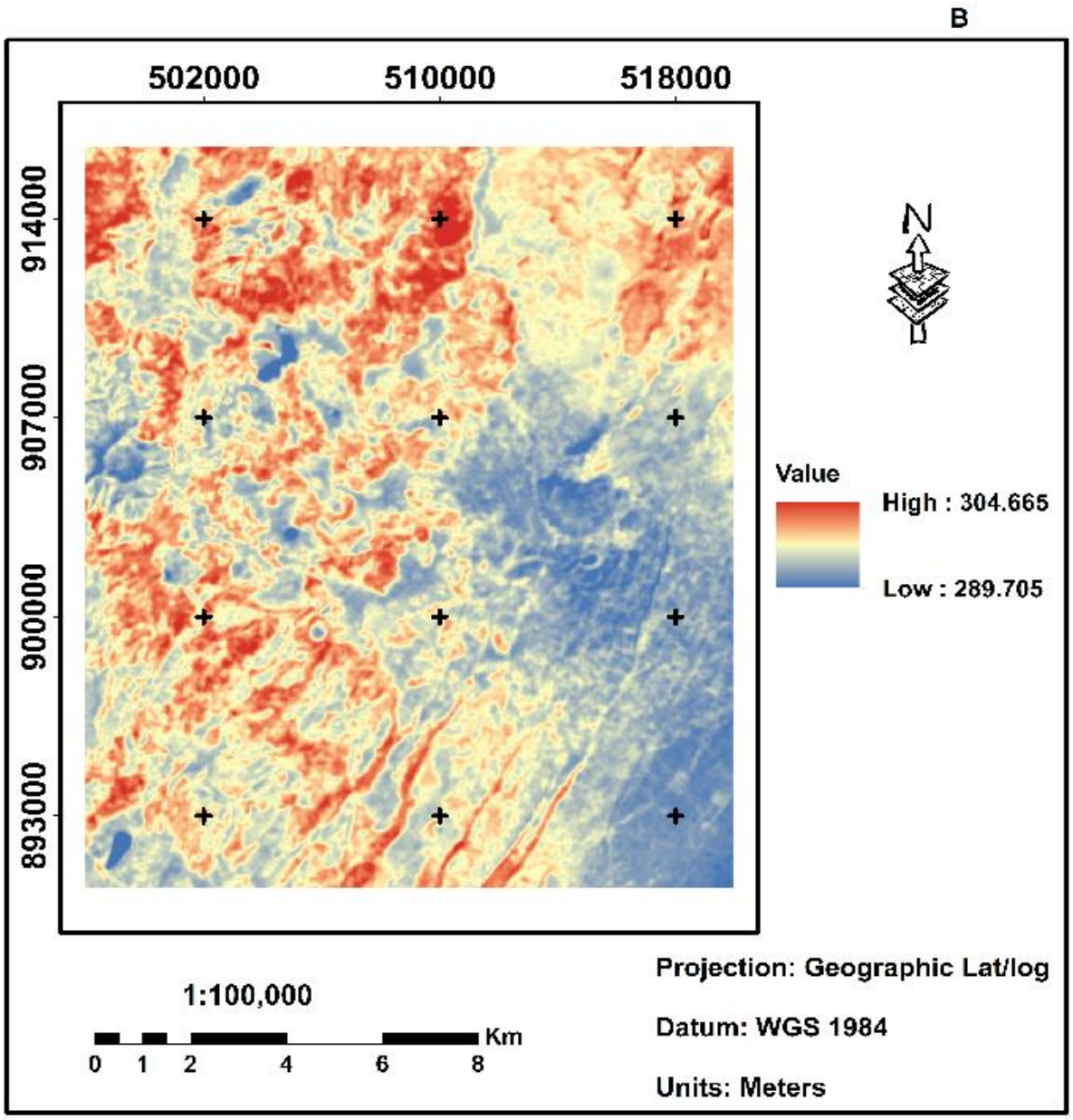

Figure 17: Top of Atmosphere Brightness Temperature map for band 10 (A) and 11 (B).

4.7 Land Surface Temperature (LST)

Figure 18 has been derived from LSE, brightness temperature and emissivity difference between LSE of band 10 and 11 of TIR. LST output portrayed that it varied from 292.23 to 315.885 ^{o}K. The highest Land Surface Temperature of more than 310 ^{o}K was traced in the NE and SW part of the study area, where barren lands and wastelands were mostly found. The 300 to 310 ^{o}K LST was traced in the foothill regions and area under cultivable land in the plains. The lowest category of less than 300 ^{o}K was seen in the highly elevated regions with dense vegetation. From Figure 18 observe that LST is 304.037 ^{o}K in 17th October 2014.

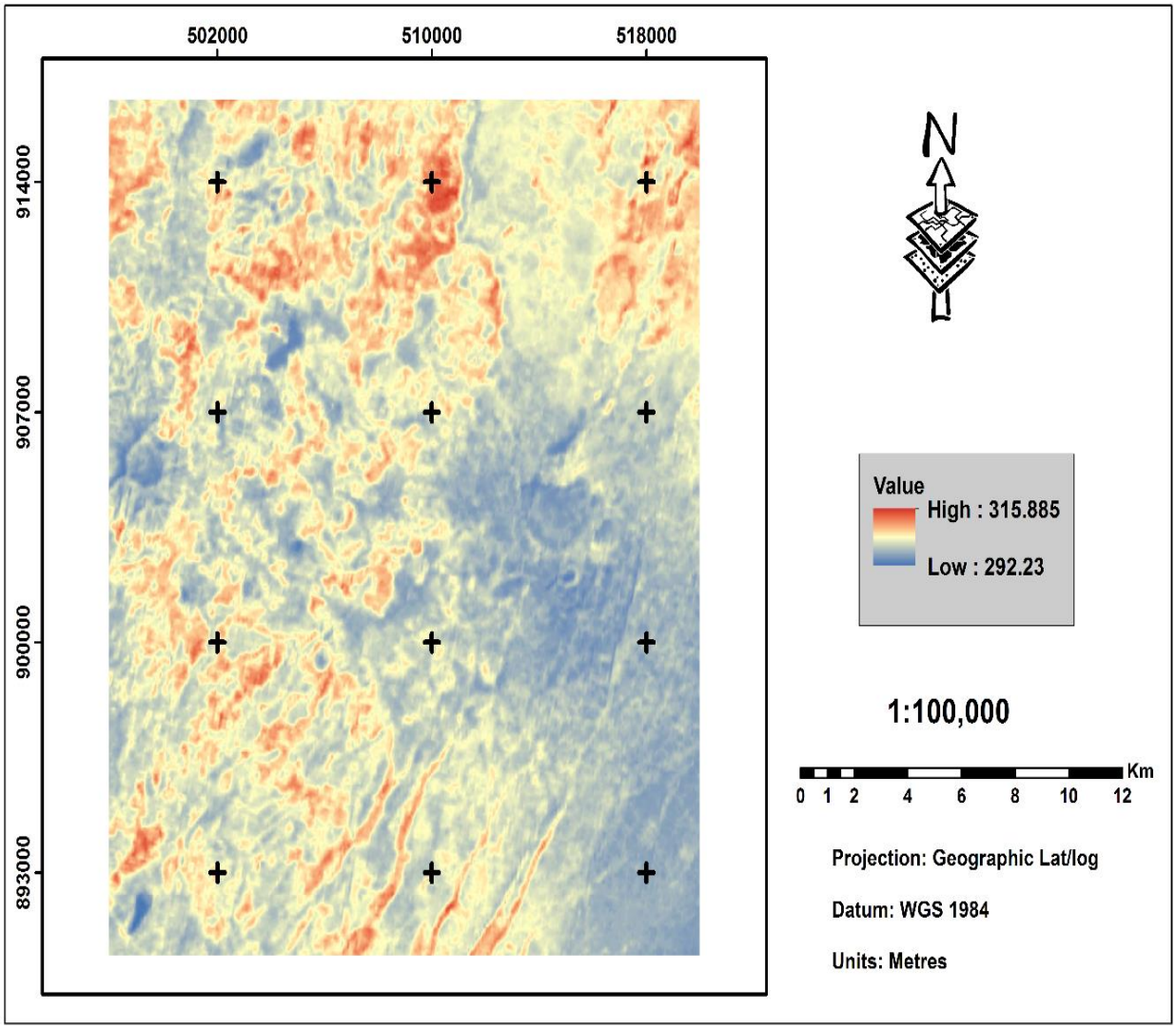

Figure 18: Mean of Land Surface Temperature map of Study area.

4.8 Land Surface Temperature Anomaly Detection

Twelve areas with conspicuous red color are picked out and marked with 1to10, A and B (Figure 19).The statistics reveal that the temperature of 1 to 10, A and B areas are overall 3–9 ^{o}K higher than the background temperature. Anomalies area of the surface have higher land surface temperature value from 299 ^{o}K up to 315 ^{o}K. Most of temperature anomalies are located in NE, Central and NW parts of lowland area of study area. In other research (Qin et al., 2011), the same technique was applied to detect four geothermal anomalies area.

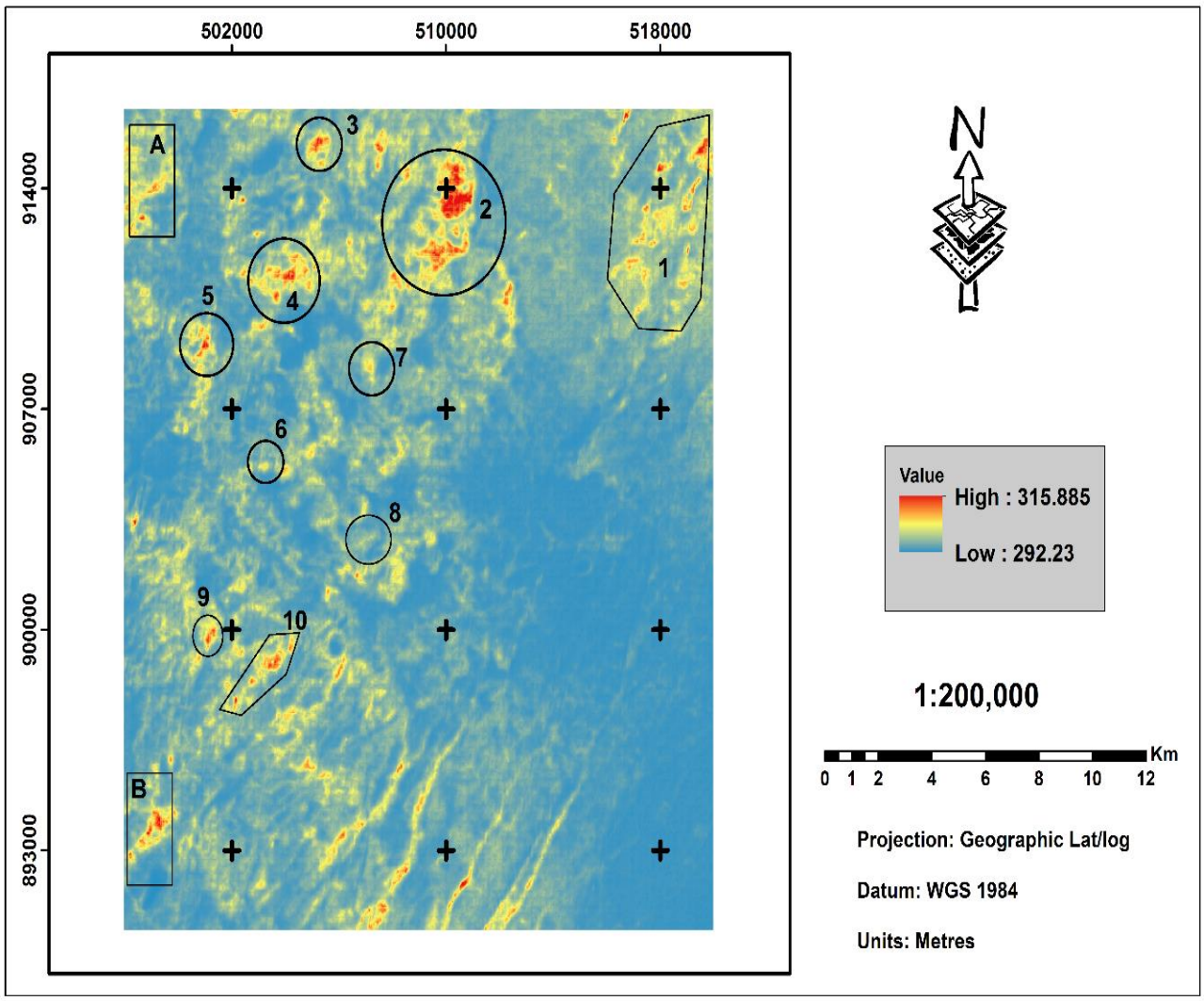

Figure 19: LST Anomaly map of Study area.

4.9 Validation of Land Surface Temperature Anomalies

Reliability of LST results derived from TIRS sensor may not always be possible to validate with ground surface temperature due to non-availability of field data concurrently with satellite overpass. LST of the study area can be retrieved from other TIR sensors and compared on spatial scales with Landsat-8 LST if their overpass time is close to Landsat-8 on a given day. In this study, MODIS TIR sensor data were also used for LST comparison and validation. LST data products of MODIS (MOD11A1) of 1 km spatial resolution on October 17, 2014 which uses split window algorithm (Wan and Dozier, 1996) on bands 31 and 32. The original Landsat 8 LST result (30 m) is resampled to 1 km to match the spatial resolution of MODIS LST product using ArcGIS 10.2 Resampling tool. The results are shown in Figure 20.

The comparison between 30 m Landsat 8 LST and 1 km Landsat 8 LST (Table 11) demonstrates a decrease in the average temperature and a narrow down in the temperature ranges for small latter "a-m" areas of the 1 km Landsat 8 LST. This is the average effect during the resample process. Due to the heterogeneity of thermal anomaly areas (standard deviation from 1.3 to 1.56 ^{o}K), the highest temperature is averaged with the surrounding lower temperature, which in the end yields a narrower temperature range than the original LST range.

The comparison between 1 km Landsat 8 LST and 1-km MODIS LST shows that the average temperature differences are all within 1.47 K for a-m areas. The result is consistent according to a study of Srivastava et al., (2009), that LST comparison between MODIS and Landsat 8 has a maximum difference of 2 ^{0}C. On this account, the accuracy of retrieved Landsat 8 LST in this study is acceptable for geothermal detection (Qin et al., 2011). Therefore, this study consider the thirteen LST anomalous areas (a-m) as the potential geothermal areas where the heat source, geological and influence of artificial manmade objects is required for actual geothermal area identification. The next step is identification of true geothermal area from false anomalies.

Table 11: Statistical comparison between Landsat 8 and MODIS LST

Location	Sensor	Spatial Resolution (RS)	Minimum (k)	Maximum (k)	Average (k)	Standard Deviation (k)	Average MODIS – Average TIRS
a	TIRS	30 m	306.72	314.39	310.56	1.52	
		1 km	308.82	310.29	309.56	0.30	
	MODIS	1 km	309.95	312.02	310.99	0.51	1.43
b	TIRS	30 m	306.16	314.92	310.53	1.56	
		1 km	308.06	310.56	309.31	0.53	
	MODIS	1 km	309.67	311.01	310.39	0.29	1.08
c	TIRS	30 m	307.88	314.73	311.31	1.49	
		1 km	308.62	311.14	309.88	0.29	
	MODIS	1 km	309.04	312.91	310.98	0.71	1.09
d	TIRS	30 m	310.41	315.81	313.11	1.41	
		1 km	311.13	312.73	311.93	0.32	
	MODIS	1 km	312.28	313.61	312.95	0.30	1.07
e	TIRS	30 m	308.53	314.81	311.67	1.45	
		1 km	309.79	311.45	310.62	0.32	
	MODIS	1 km	310.85	313.01	311.93	0.53	1.31
f	TIRS	30 m	308.31	315.87	312.09	1.50	
		1 km	309.57	312.05	310.81	0.57	
	MODIS	1 km	310.86	312.78	311.82	0.50	1.01
g	TIRS	30 m	309.72	314.39	312.06	1.30	
		1 km	308.82	310.29	309.56	0.33	

	MODIS	1 km	310.03	312.02	311.03	0.35	1.47
h	TIRS	30 m	306.01	314.16	310.09	1.50	
		1 km	306.92	310.26	308.59	0.73	
	MODIS	1 km	307.24	312.54	309.89	0.82	1.3
i	TIRS	30 m	307.92	314.77	311.35	1.49	
		1 km	308.84	309.10	308.97	0.21	
	MODIS	1 km	309.21	311.35	310.28	0.39	1.31
j	TIRS	30 m	307.44	314.99	311.22	1.50	
		1 km	308.11	309.21	308.66	0.33	
	MODIS	1 km	309.54	310.57	310.06	0.31	1.4
k	TIRS	30 m	308.32	315.72	312.02	1.41	
		1 km	309.31	311.29	310.30	0.34	
	MODIS	1 km	310.55	312.11	311.33	0.10	1.03
l	TIRS	30 m	308.28	315.13	311.71	1.49	
		1 km	309.02	311.54	310.28	0.32	
	MODIS	1 km	309.44	313.31	311.38	0.33	1.1
m	TIRS	30 m	309.32	313.99	311.66	1.34	
		1 km	308.42	309.89	309.16	0.22	
	MODIS	1 km	309.63	311.15	310.39	0.12	1.23

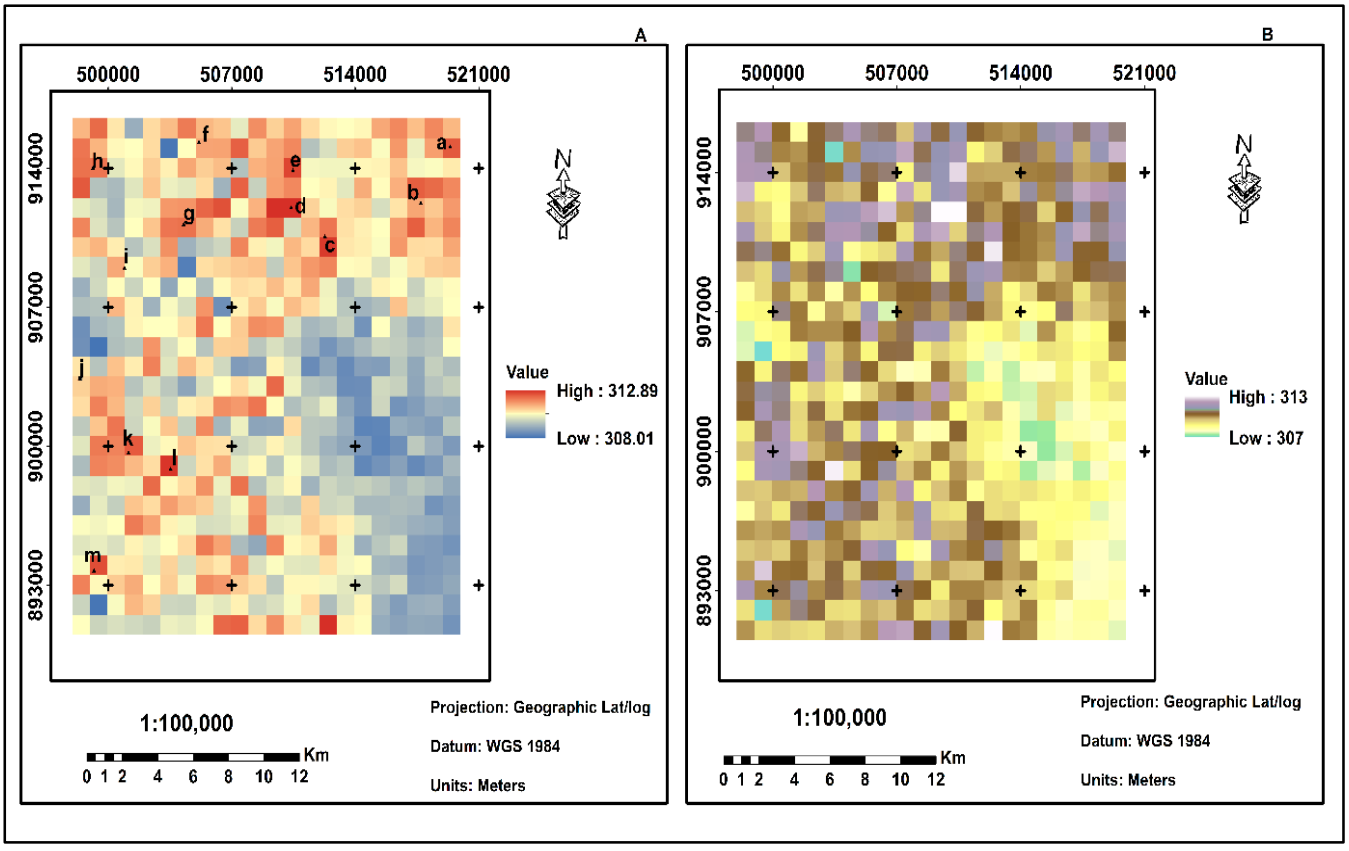

Figure 20: Resampled Landsat 8 LST (A) and Original MODIS (MOD11A1) (B) of 1 km spatial resolution.

4.10 False Geothermal Anomalies Detection

The artificial thermal influences were considered in this study. Therefore, auxiliary data or analysis tools are required to exclude the non-geothermal influences. Considering the human influence is gradually reduced with the increase of distance to urban area, the distance to urban area is calculated with the Buffering Distance function in ArcMap 10.3 (ESRI, 2015). An empirical distance of 1000 m is assigned as the maximum distance to urban areas, assuming that the area more than 1000 m away from urban area is not affected by the thermal effect from human activities. This made it easier to distinguish geothermal activity from false thermal anomalies. Based on this assumption two area are takes as non-geothermal area. Northwest and southwest corner of study area in figure 21. Those are highly thermally anomalies area but these are not the influence of internal heat energy, these are the influence of human activity.

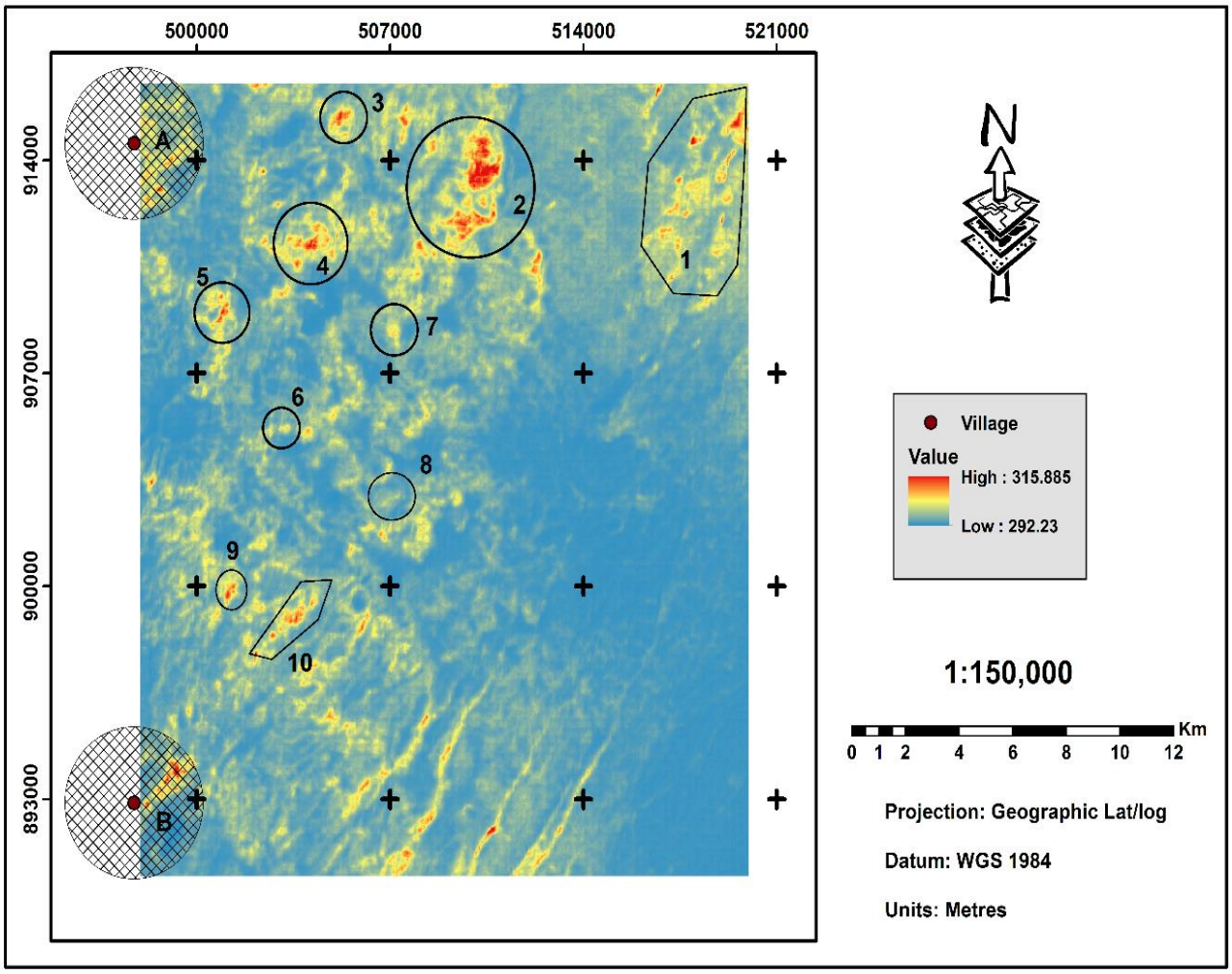

Figure 21: Artificial thermal influences map of Study Area.

4.11 Heat Source Analysis

The Ethiopia and foreign researchers have applied a variety of geophysical and geochemical techniques for geothermal detection in MER area since 1970, especially in Tulu-Moye geothermal field. Some of efforts are listed as below.

Volcanism in the Tulu Moye area involved the extrusion of peralkaline felsic lava associated with young tensional and transverse tectonic features dating from 0.1 to 1.2 million years (Di Paola, 1970). This suggests the existence of a deep seated magma chamber with a long residence time. The study conducted geological and petrochemical study of the Tulu Moye area together with the production of 1:50,000 scale geological map ELC (1987, as cited in Abebe et al., 2002). This study showed the occurrence of abundant thermal manifestation that indicated the existence of deep-seated heat source. The heat source could possibly be related to magmatic intrusion at a relatively shallow depth with highly differentiated products being widely exposed at surface. ELC (1987, as cited in Ayele et al., 2002) has conducted fluid and soil geochemical studies including radon survey in Tulu Moye-Gedemsa prospect areas. The study confirmed the presence of high temperature at depth. Resistivity surveys (Ayele et al., 2002) showed that a conductive core zone existed under Tulu-Moye area, which was suggested to be a magma chamber. The experiments of seismic velocity tomography (Ayele et al., 2002) also indicated the existence of a magma chamber below the Tulu-Moye geothermal field. The evidence from helium/carbon isotope experiments (Ayele et al., 2002) revealed that the emitting gases from the discharges of high geothermal gradient regions at Tulu-Moye area were related to the intruding mantle-derived magma nearby.

On the summary of previous researches, it can be inferred that the intrusive activities of mantle-derived magma exist in the shallow crust of Tulu-Moye geothermal field and are accompanied with the intensive mantle gas emissions. The magmatism serves as a powerful heat source for modern geothermal activities in study area.

4.12 Geological Analysis

In the central, northern and southern part of the study area, which is highly affected by the Wonji Fault Belt (WFB), the rift-in-rift (graben- horst) structures usually run parallel to each other. WFB is an intense zone of normal faulting and volcanism in this area. Each segments of the WFB hosts at least one major felsic central volcanic complex of quaternary age, the likely deep seated magma chambers feeding these centers as heat sources for the widespread hydrothermal activity in the region. Lineaments (faults and associated tensional fissures) are relatively concentrated on the

eastern part of the area closer to the main eastern escarpment of the rift valley. The direction of downthrow of the faults is again variable but more commonly to the west associated with tensional fractures.

This faults extends from eastern shore of lake Ziway up to Gedemisa caldera, consists of faults and open fractures trending NNE-SSE with 0.5-1 km spacing striking generally $N20^0$ E, and form horsts and grabens. Tulu Moye, including Bora, Berricha, and other volcanic complexes are in this segment. These are characterized by NW-SE transverse normal faults. These transverse faults features intersect the NNE-SSW major faults. The eastern part of Tulu Moye is affected by NNE-SSE trending closely spaced normal swarms and open tensional fissures.

The surface geology of Tulu-Moye area was presented in terms of stratigraphy. The stratigraphic units of the area are Obsidians(QTo), Trachytes(QTt), Basalts(QWpb), Pumice Pyroclastics and Poorly Welded Tuffs(QTpu), Rhyolites(QTr) and Older Basalt (QWpb); which belongs to the Wonji Group Volcanics and Rhyolites and Ignimbrites(NQr)/NQn) correlated to the Nazreth Group (Ayele et al., 2002).In Addition to these, there is also sedimentary units.

Further geological investigations reveal a close correlation between the faulted structure and the distribution of geothermal anomalies. With the knowledge of study area in Chapter 3, we can find that most of the volcanoes (Di Paola, 1972; Woldegebriel et al., 1990) and fumaroles (Ayele et al., 2002).

In order to have a direct impression on the tectonic landform of study area, this study achieve a three-dimensional (3-D) topographic map (Figure 22) with the topography simulation function of ArcScene software. Nine LST anomaly areas (1-9) are marked by their center points. A simplified LST image is listed aside for comparison (Figure 23).

Figure 23 is demonstrates that 1 to 9 are all located in the fault valley with an inclined “S” distribution, which is consistent with the “S”-shaped line connecting the thermal anomalous areas. It can be well explained that the faulted structure provides passageways for thermal transmission with which the underground heat can be efficiently transferred to land surface and detected as LST anomalies in thermal infrared images.

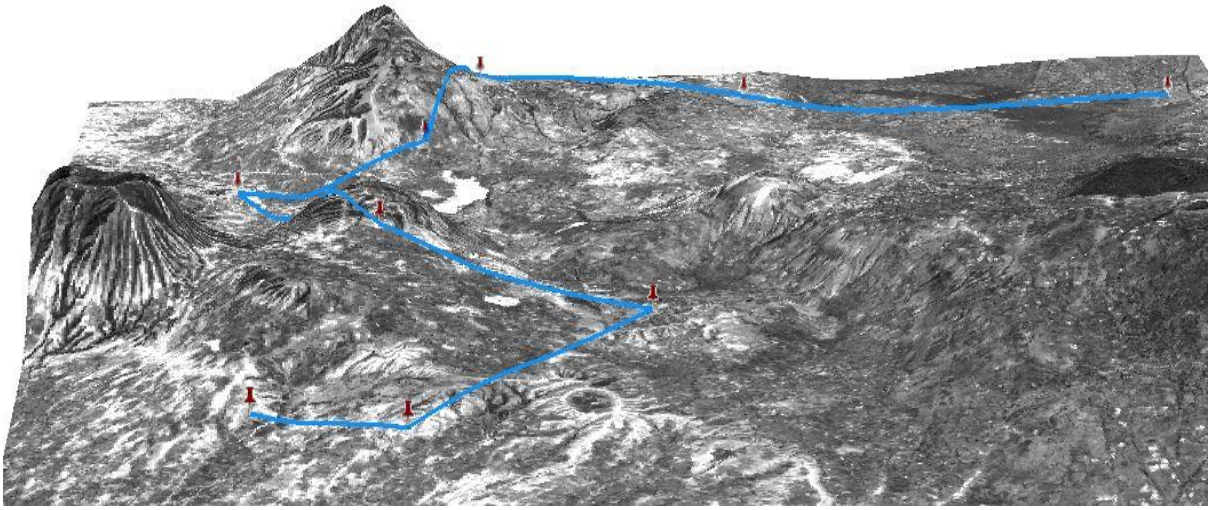

Figure 22: Three dimensional topographic image of study area marked with nine thermal anomalous areas.

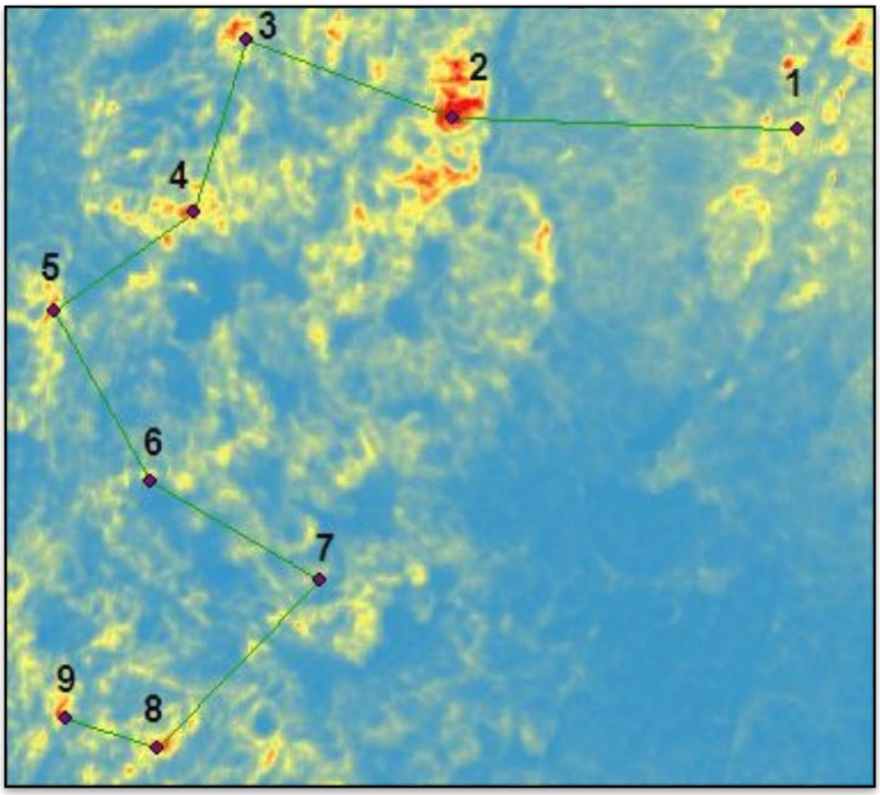

Figure 23: Geothermal anomaly image of study area.

4.13 Identification of Geothermal Areas

Based on the analysis of heat source and geological structure, we conclude that the underground magmatism contributes abundant thermal source for Tulu Moye area, and the faulted structure in study area serves as thermal channel for heat transfer. With the two available prerequisites, underground heat is transferred to land surface and disturbs the surface energy balance, which takes on surface thermal anomalies. Therefore, the LST anomalies (1-9) in this research can be determined as geothermal areas as shown in figure 23.

4.14 Validation

The validation of selected geothermal areas is carried out by previous work and field investigation. The result shown as figure 24. Known hydrothermal manifestation such as Janno Hydrothermal Field (geothermal areas 1), Hamudie Hydrothermal Field (geothermal areas 2), Berecha Volcanic Complex Hydrothermal Field (geothermal area 3), Eleda Hydrothermal Field (geothermal area 4), Jima Hydrothermal Field (geothermal area 6), Dima Hydrothermal Field (geothermal area 7), those six area successfully identified. Those are famous geothermal landscapes in study area and have developed into the tourist attractions integrating sightseeing, spa bath and medical care. Fumaroles and steaming ground are widely distributed in the six geothermal areas.

Hydrothermal Manifestation areas in the center of study area map such as the surrounding Tulu Moye volcanic complex (C), and werdi (D), which are indicated by red circle and rectangular shape in the result as shown in figure 24. Those are not identify by TIRS remotely sensed sensor. And also, unable to map famous hydrothermal field located at Bericha Hydrothermal Field (E), northwest Jima (F) and Dima (G) are not detected by TIRS sensor. In the contrary, it enabled mapping of three previously unidentified geothermal features has been identified in the west (5) and south west (8 and 9) of study area (Figure 24).

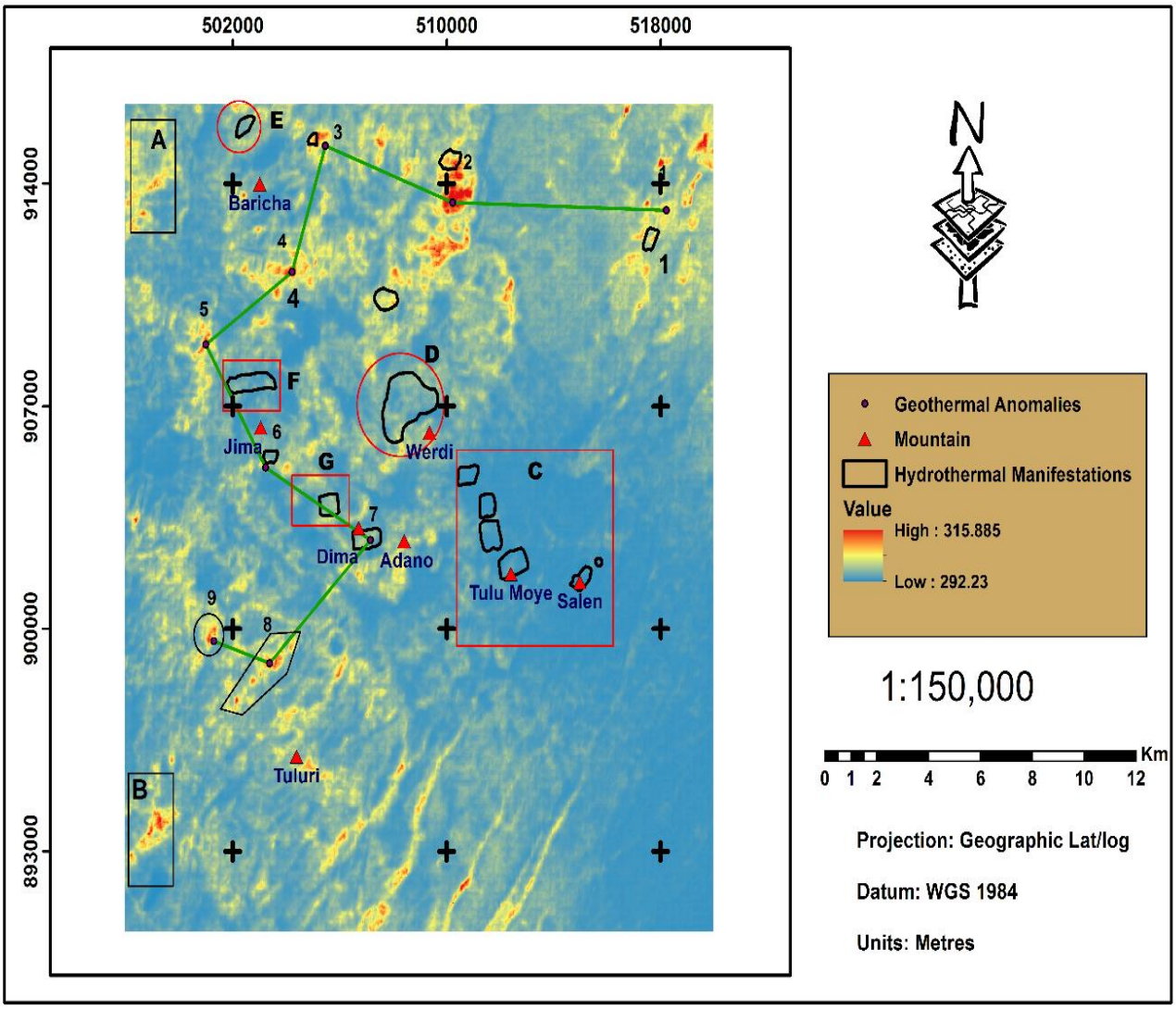

Figure 24: Validation map between known hydrothermal manifestation and LST Anomalies.

4.15 Discussion

The objective of this research is identify geothermal area using Landsat 8 thermal data. In order to achieve the objective of the research, land surface temperature anomaly detection have been applied. There are a number of papers demonstrating this approach to map land surface temperature and correlate that to geothermal heat. In their study, this approach is cost-effective and important tool in the exploration geothermal resource.

In this study, land surface temperature extraction and anomalous areas detection with temperature about 3–9 ^{o}K higher than background area are discovered. Nine geothermal areas are identified.

Those are well known and some previously unidentified geothermal features including fumaroles and steaming ground.

This research clearly outlined that geothermal features at Janno, Hamudie, Berecha, Eleda, Jima and Dima hydrothermal fields. According to Ayele et al., (2002), the hydrothermal activity categorized based on their geographical distribution. That are as follow: the description of identified hydrothermal field adopted from this work.

The janno Hydrothermal Field is extracted at the northeast corner of study area with a random distribution pattern. The area is altered zone with warm ground of temperature up to 40 ^{0}C. Its land surface temperature, measured by TIR sensor is 41.2 ^{o}C (figure 25-1).

Hamudie Hydrothermal Field is found in the south of Hamudie village at the foot of a rhyolite hill. The altered zone is covered relatively large area with weak fumaroles having temperature up to 50 ^{0}C. In this thesis, land surface temperature have 42 ^{0}C.

Berecha Volcanic Complex Hydrothermal Field is found in northeastern berecha mountain. There are weak fumaroles having temperature up to 48 ^{0}C, land surface temperature result extracted by TIR sensors in this location is 41.7 ^{0}C in figure 25 -3.

Eleda Hydrothermal Field is located at Elada area, which mostly follows the NNW trending structure zone. There is a small area of warm ground with land surface temperature value of 42 ^{0}C in figure 25-4.

Jima and Dima hydrothermal field, the area have warm ground with Weak fumaroles, temperature are close to 50 and 45 ^{0}C. From measured TG wells it can be seen that anomalously high temperatures were registered in TG-4 wells near Mt. Dima with 40 ^{0}C/ 100 m thermal gradients. Land surface temperature value are 42 and 39 ^{0}C for Jima and Dima hydrothermal field respectively (Figure 25-6&7).

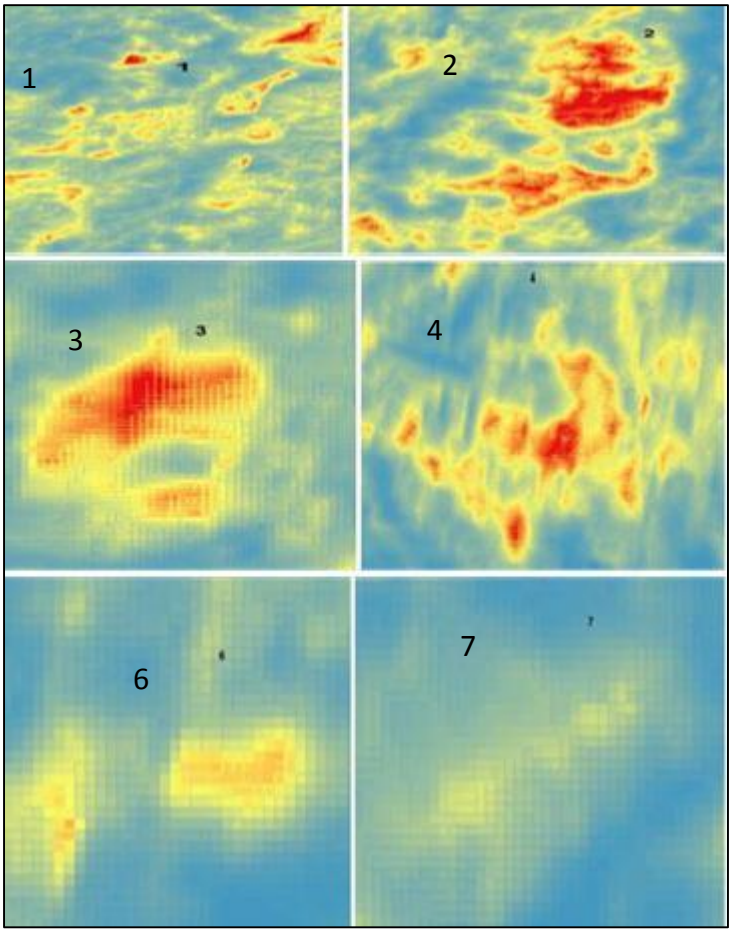

Figure 25: Six known identified geothermal area

These study shows that thermal infrared (TIR) data, could be used to retrieve land surface temperature for large areas and identifying the extent of shallow geothermal resources and geothermal hot springs. In many studies, It has been widely used in geothermal exploration such as Seielstad and Queen, (2009); Kienholz et al., (2009); Coolbaugh et al., (2007).

In other researches work (Qin et al, 2011), four geothermal areas in Yunnan province of China were identified based on ETM+ TIR data. In their study, the artificial thermal influences were not considered as false anomaly of temperature. However, this artificial thermal influences were considered. Because of this, the northwest and southwest corner of study area were excluded form the result as shown in figure 24-A & B.

Mt. Moye Hydrothermal Field (C) have two volcanoes namely Tulu Moye Danise and Tulu Moye Terro. The area is affected by hydrothermal activity and there is an extensive area of thermal manifestation. There are fumaroles having a temperature up to 90 ^{0}C. However, these geothermal temperature anomalies were not detected by TIRS sensor. When examined with a broader review,

area in east is all covered by forest and vegetation with high altitude elevation up to 2212m as shown in figure 26. The presence of vegetation or forest around anomalous area, low resolution like Landsat 8 TIRS sensor record a mixture of emitted radiance from geothermal sources as well as from background non-geothermal surfaces (Claudia and Stefan, 2013). This acts to reduce the measured temperature of pixels corresponding to geothermal sources. As a result, a dominant feature of vegetation and forest are recorded by sensor other than anomalies surface temperature.

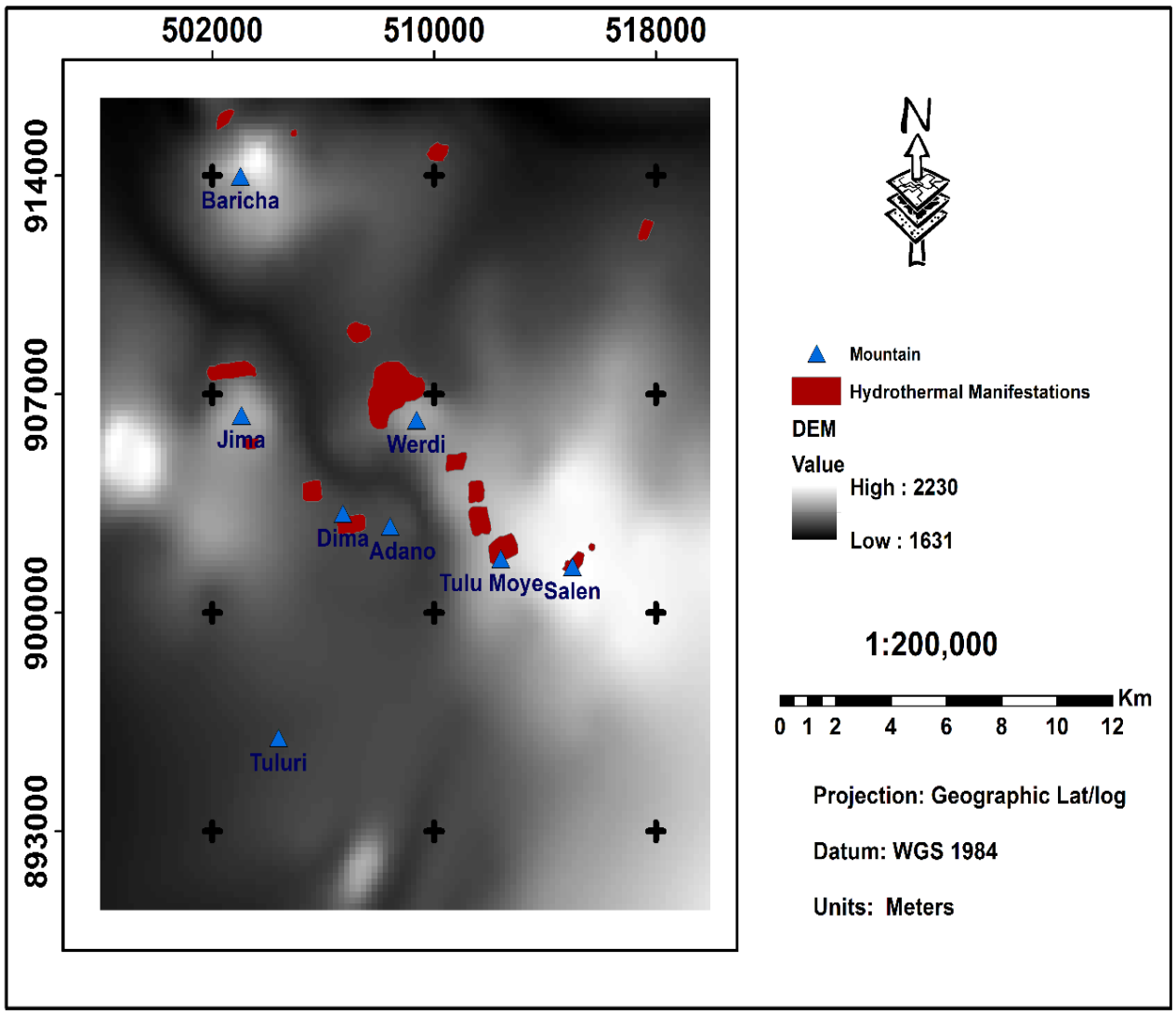

Figure 26: Hydrothermal manifestation map.

Werdi Hydrothermal Field (D) has an extensive area of altered zone with the fumaroles range in temperature from 45 to 60 0C. Its coverage is small in size and it is located at high elevation as shown in figure 26. If the target area is small in size, low resolution like Landsat 8 TIR sensor is

record a mixture of feature with surrounding objects. As a result, it reduce the temperature of pixel that related with geothermal sources. The same reason is applied for north berecha (E) and Kechkechi Hydrothermal Field (F) as shown in figure 24, which are not identify by thermal sensor.

The amount of energy radiated an object depends on its absolute temperature, its emissivity and is a function of the wavelength. In physics, this principle is defined by Stefan-Boltzmann's Low in Equation 4. If objects made by the same material with the same emissivity and tempreture, the amount of energy radiated by an object is the same.

Study area have the volcanic rocks type based on the geological map in figure 7. But from the same rock type, the temperatures are different in three LST anomalies area at northeast Jima (5), 8 and 9 (figure 24). Area at northeast Jima (5) has Alluvium rock type with a temperature 314.77 K/ 41.62 ^{0}C. This value is anomalously high when compared with the same rock type in other location. Remaining two of anomalies area have deposits of pyroclastic and poorly welded pumice breccia rock type. Those are anomalously high when compared with the same rock type in other location with temperature 315.72 K /42.57 ^{0}C and 315.13 K/ 41.98 ^{0}C respectively. From these visual interpretation, it enabled mapping of three new previously unidentified heated ground geothermal features detected by thermal infrared data.

5. Conclusion and Recommendations

5.1 Conclusion

In this thesis, a combination of remote sensing and GIS were used for geothermal area detection. A geothermal area detection is carried out in Tulu-Moye, northwest of Asela, region of Oromia, Ethiopia. To achieve the objective this thesis Landsat 8, topographic map, geological map, ancillary data, GPS and MODIS Tera/LST were used to detect land surface temperature anomaly.
In the pre-processing operation, atmospheric and radiometric calibration is applied by converting Digital Number (DN) recorded by the remote sensor into the at-atmosphere radiance. And then, atmospheric radiance is converted to reflectance using 6S model.

In the major analysis part, Sensor Brightness Temperature, Fractional Vegetation Cover and Land Surface Emissivity were retrieved from the two OLI and TIRS bands. Those are important parameters to get actual land surface temperature. Retrieved the land surface temperature using split window algorism with the result of maximum and minimum value of 315.89 K and 292.23 K respectively. With a technique of visual interpretation nine LST anomalies area is selected. Comparison between Landsat 8 and MODIS LST is applied and the result shows that average temperature difference is less than 2 ^{0}C which is acceptable accuracy for geothermal detection.

GIS (ArcMap 10.3) is applied for distance analysis to exclude false anomaly from urban and village area. Thematic and geological maps were used for detail interpretation of geothermal anomalies. Identified geothermal areas are determined with the geothermal mechanistic analysis and regional geologic investigation. The results demonstrate that the distribution of geothermal areas correlates closely with the development of faulted structure. The magmatism in study area serves as heat source for geothermal anomalies and the faults provide the thermal channels for heat transfer which disturbs the localized balance of surface energy and cause thermal anomalies at land surface.

Finally, six geothermal areas are successfully extracted in east, northeast and west part of study area, while two prospective geothermal areas in the north part are newly explored and deserve further exploration
The results also indicate that thermal infrared remote sensing is an overall effective and accurate method for geothermal exploration. The methodology applied in this work has efficiently reduced the extent for geothermal exploration and locate the promising geothermal areas for further exploration.

However, it can only detect the surfacial thermal anomaly and is sensitive to the geothermal resource covered by vegetation/forest with small in size. Therefore, geologic analysis and the mechanism of geothermal anomaly are required to assist and facilitate the identification of geothermal areas with TIR remote sensing. With the knowledge of geothermal mechanism and the complement from the geological investigation, the accuracy of geothermal detection using TIR remote sensing can be much improved.

5.2 Recommendation

Landsat 8 Thermal infrared (TIR) remote sensing data, which is free from cost has a capability to detect geothermal features such as fumaroles, warm ground and steaming ground, which comes from the subsurface of the area reach the ground by conduction and convection. So that, Governmental, international investor and private organization can use cost effective approaches to find best targets for the first few deep wells.

Although coarse spatial resolution satellite thermal sensors, such as Landsat 8, have limited potential for detailed mapping of discrete geothermal features, these datasets used for broader scale detection of geothermal anomalies. High resolution thermal sensor data is enable detailed mapping of surface geothermal phenomena and can detect subtle surface temperature anomalies. For betterment of geothermal detection, high resolution thermal sensor have a potential than low resolution.

Three previously unidentified heated ground geothermal features need further geological, geophysical and geochemical investigation to decide on the feasibility of a power project.

Reference

Arnórsson, S., Bjarnason, J.Ö., Giroud, N., Gunnarsson, I. and Stefánsson, A. (2006). Sampling and analysis of geothermal fluids. *Geofluids*. **3**: 203-216.

Artis, D.A. and Carnahan, W.H. (1982). Survey of emissivity variability in thermography of urban areas. *Remote Sensing of Environment*. **12**: 313-329.

Asrat, A. (2006). Introduction to Physical Geography. Addis Ababa University, Department of earth sciences, Addis Ababa, Ethiopia, 277 pp.

Ayele, A., Teklemariam, M. and Kebede, S. (2002). Geothermal Resource Exploration in the Abaya and Tulu Moye-Gedemsa Geothermal Prospects, Main Ethiopia Rift. Unpublished technical report, Geological Survey of Ethiopia, Addis Ababa, Ethiopia, 172 pp.

Baldridge, A. M., Hook, S. J., Grove, C. I. and Rivera, G. (2009). The ASTER spectral library version 2.0. *Remote Sensing of Environment*. **113**: 711–715.

Bigazzi, B., Bonadonna, F., Di Paola, G. and Giuliani, A. (1993). K-Ar and fission tracks ages of the last volcano-tectonic phases in the Ethiopian Rift Valley (Tulu Moye area). *Geology and mineral resources of Somalia and Surrounding Regions*. **113**: 311-322.

Carlson, T.N. and Ripley, D.A. (1997). On the relation between NDVI, fractional vegetation cover, and leaf area index. *Remote sensing of Environment*. **62**: 241-252.

Cesar, C. and Vicente, C. (1997). A split-window algorithm for land surface temperature from advanced very high resolution radiometer data: Validation and algorithm comparison. *Journal of Geophysical Research*.**102**: 16,697-16,713.

Claudia, K. and Stefan, D. (2013). *Thermal Infrared Remote Sensing Sensor, Method, Application*, 1st ed., Springer, London, 525 pp.

Coolbaugh, M.F., Kratt, C., Fallacaro, A., Calvin, W.M. and Taranik, J.V. (2007). Detection of geothermal anomalies using advanced spaceborne thermal emission and reflection radiometer (ASTER) thermal infrared images at Bradys Hot Springs, Nevada, USA. *Remote Sensing of Environment*. **106**: 350-359.

CSA (Central Statistics Agency) (2007). Population and Housing Census Report. Retrieved from http://www.csa.gov.et/ accessed on January 30, 2016.

Di Paola, G.M. (1970). Geological, Geothermal Report on Central Part of the Main Ethiopia Rift Valley. Unpublished technical report, Geological Survey of Ethiopia, Addis Ababa, Ethiopia, 167 pp.

Di Paola, G. M. (1972). The Ethiopian Rift Valley (between 7º00' and 8º40' Lat. North). *Bulletin of Volcanology*. **35**: 497-506.

Engdawork, A. (2007). Structural Study and Its Effect on Thermal Activities of Tulu Moye-Gedemsa Area. Unpublished MSc Thesis, Addis Ababa University, Addis Ababa, Ethiopia, 78 pp.

ESRI (Environmental Systems Research Institute) (2015). Using ArcMap 10.3. Retrieved from http://links.esri.com/arcgisdesktop/103/en/documentation/ accessed on March 12, 2016.

Haselwimmer, C.E and Prakash, A. (2011). Geothermal exploration at Pilgrim Hot Springs, Alaska using airborne thermal infrared remote sensing. **In:** proceeding of Geothermal Resource Council annual meeting, pp. 221-231. San Diego, USA.

Henk, J.B. and Jan, G.P. (1993). *Land Observation by Remote Sensing: Theory and Applications*, Gordon and Breach Science, UK, 642 pp.

Hochstein, M. (2005). Heat transfer by hydrothermal systems in the East African Rifts. **In**: Proceedings of the World Geothermal Conference, pp. 1-7. Antalya, Turkey.

Hodder, D.T. (1970). Application of remote sensing to geothermal prospecting. *Geothermics.* **2**: 368-380.

Jiménez-Muñoz, J. C. and Sobrino, J. A. (2003). A generalized single-channel method for retrieving land surface temperature from remote sensing data. *Journal of Geophysical Research.* **108 (D22)**: 121–133.

Jiménez-Muñoz, J. C., José, A. Sobrino., Dražen, Skokovi´c., Cristian, Mattar. and Jordi. C. (2014). Land Surface Temperature Retrieval Methods from Landsat-8 Thermal Infrared Sensor Data. *IEEE Transactions on Geoscience and Remote Sensing*. **11(10)**: 1840-1843.

Kazmin, V., Seif, M.B., Nicoletti, M. and Petrucciani, C. (1980). Evolution of the northern part of the Ethiopian Rift. *Atti Convegni Lincei*. **47**: 275-292.

Kienholz, C., Prakash, A. and Kolker, A. (2009).Geothermal Exploration in Akutan, Alaska, using multitemporal thermal infrared images. Paper presented at the scientific meeting of the American Geophysical Union, pp.1009. San Francisco, USA.

Lee, K. (1978). Analysis of thermal infrared imagery of the Black Rock Desert geothermal area. *Q. Colo. Sch. Mines*. **73(3)**: 31-43.

Lees, J.M. (2007). Seismic tomography of magmatic systems. *Journal of Volcanology and Geothermal Research*. **167**: 37-56.

Lo, C. P. and Yeung, A. K. (2007). *Concepts and techniques of geographic information systems*, 2nd ed., Pearson Prentice Hall, USA, 544 pp.

Mamo, T. (2001), Surface hydrothermal alteration in the Tulu Moye area, lakes district rift, Ethiopia. Unpublished technical report, Geological Survey of Ethiopia, Addis Ababa, Ethiopia, 8 pp.

Manfred, P.H. (2005). Heat Transfer by Hydrothermal Systems in the East African Rifts. **In:** *Proceedings of World Geothermal Congress*, pp.1-7. Antalya, Turkey.

Martin, J., Eugenio, F., Marcello, J., Medina, A., Bermejo, J. A. and Arbelo, M. (2012). Atmospheric correction models for high resolution WorldView-2 multispectral imagery: A case study in Canary Islands, Spain. *SPIE International Society for Optics and photonics*. **8534**: 1-10.

Mongillo, M. (1994). Aerial thermal infrared mapping of the Waimangu Waiotapu geothermal region, New Zealand. *Geothermics*. **23**: 511–526.

MoWE (Minister of Water and Energy) (2011). Power Generation Projects Open for Private Sector Participation. Retrieved from http://ethioembassy.org.uk/new/index.php/documents/ plan- publications/file/22-mowe-power-generattion-projects accessed on December 4, 2015.

Peter, O. and Teklemariam, M. (2010). Overview of Geothermal Resource Utilization in the East African Rift System. Paper presented at the scientific meeting of the African Union Commission, pp.1-11. Addis Ababa, Ethiopia.

Qin, Q., Ning, Z., Peng, N. and Leile, C. (2011). Geothermal area detection using Landsat ETM+ thermal infrared data and its mechanistic analysis-A case study in Tengchong, China. *International Journal of Applied Earth Observation and Geoinformatics.* **13**: 552-559.

Ronald, D. (2005). *Geothermal Power Plants: Principle, Applications and Case Studies*. Elsevier, UK, 512 pp.

Rubio, E., Caselles, V., Coll, C., Valor, E. and Sospedra, F. (2003). Thermal infrared emissivities of natural surfaces: Improvements on the experimental set-up and new measurements. *International Journal of Remote Sensing*. **24**: 5379–5390.

Sabins, F.F. (1996). *Remote sensing*, 3rd ed., Wiley, New York, 450 pp.

Seielstad, C and Queen, L. (2009). Thermal remote monitoring of the Norris Geyser Basin, Yellowstone National Park. Unpublished technical report. Yellowstone National Park, USA, 38 pp.

Siahaan, M., Soebandrio, A. and Wikantika, K. (2011). Geothermal Potential Exploration Using Remote Sensing Technique (Case Study: Patuwa area, West Java). **In**: Proceedings of the 10th Annual Asian Conference, pp. 1–13. Jakarta, Indonesia.

Skokovic, D., Sobrino, J.A., Jimenez-Munoz, J.C., Soria, G., Julien, Y., Mattar, C. and Jordi, C. (2014). Calibration and Validation of Land Surface Temperature for Landsat 8 – TIRS Sensor. Unpublished Technical report, ESA, Italy, 27pp.

Sobrino, J. A., Jimenez-Munoz, J. C. and Paolini, L. (2004). Land surface temperature retrieval from LANDSAT TM 5. *Remote Sensing of Environment*. **90**: 434–440.

Sobrino, J. A., Jimenez-Munoz, J. C., Soria, G., Romaguera, M., Guanter, L., Moreno, J., Plaza, A. and Martincz, P. (2008). Land surface emissivity retrieval from different VNIR and TIR sensors. *IEEE Transactions on Geoscience and Remote Sensing.* **46(2)**: 316–327.

Sobrino, J. A., Li, Z. L., Stoll, M. P. and Becker, F. (1996). Multi-channel and multi-angle algorithms for estimating sea and land surface temperature with ATSR data. *International Journal of Remote Sensing*. **17**: 2089– 2114.

Sobrino, J.A. and Raissouni, N. (2000). Toward remote sensing methods for land cover dynamic monitoring: application to Morocco. *International Journal of Remote Sensing*. **21**: 353-366.

Solomon, k. (2012). Geothermal Exploration and Development in Ethiopia: Status and Future Plan. *Short Course VII on Exploration for Geothermal Resources*, Lake Bogoria and Naivasha, Kenya.

Srivastava, P.K., Majumdar, T.J. and Bhattacharya, A.K. (2009). Surface temperature estimation in Singhbhum Shear Zone of India using Landsat-7 ETM+ thermal infrared data. *Advances in Space Research.* **43 (10)**: 1563–1574.

Teklemariam, M and Kebede, S. (2010). Strategy for Geothermal Resource Exploration and Development in Ethiopia. In: Proceedings World Geothermal Congress, pp.1-9. Bali, Indonesia.

Tesfaye, K. (1992). Lithologic and structural mapping of northeast Lake Ziway area, Ethiopian Rift, using Landsat Digital data. Unpublished MSc Thesis, Addis Ababa University, Addis Ababa, Ethiopia, 156 pp.

Tesfaye, K., Chorowicz, J., Collet, B. and Bonavia, F. F. (1997). Volcanic vents rooted on extension fractures and their geodynamic implications in the Ethiopian Rift. *Journal of Volcanology and Geothermal Research* **79**: 205-222.

Thomas, M. L. and Ralph, W. K. (1994). *Remote Sensing and Image Interpretation*, 3rd ed., John Wiley and Sons, New York, 750 pp.

UNDP (United Nation Development Program) (1973). Investigation of geothermal resource of power development Geology, Geochemistry and Hydrogeology of Hot Spring of the east Africa Rift System within Ethiopia. Unpublished technical report, UNDP, New York, USA, 275 pp.

USGS (United State Geological Survey) (2015). Landsat 8 Data User Handbook. Retrieved from http://landsat.usgs.gov accessed on January 30, 2016.

Valor, E. and Caselles, V. (1996). Mapping land surface emissivity from NDVI: Application to European, African, and South American areas. *Remote sensing of Environment*. **57**: 167-184.

Van de Griend, A.A. and Owe, M. (1993). On the relationship between thermal emissivity and the normalized difference vegetation index for natural surfaces. *International Journal of remote sensing*. **14**: 1119-1131.

Van der Meer, F., Hecker, C., Van Ruitenbeek, F., Can der Werff, H., de Wijkerslooth, C. and Wechsler, C. (2014). *Geologic remote sensing for geothermal exploration: A review. International Journal of Applied Earth Observation and Geoinformation*. **33**: 255-269.

Vermote, E. F., Tanre, D., Deuze, H, M. and Morcrette, J. (1997b). Second Simulation of the Satellite Signal in the Solar Spectrum, 6S: An overview. *IEEE Transactions on Geoscience and Remote Sensing*. **35**: 675-686.

Walker, J. (2008). *Fundamentals of physics*, 8th ed., Wiley, New York, 891 pp.

Wan, Z. and Dozier, J. A. (1996). Generalized split-window algorithm for retrieving land surface temperature from space. *Transactions on Geoscience and Remote Sensing*. **34(4)**:892–905.

Weng, Q., Lu, D. and Schubring, J. (2004). Estimation of land surface temperature – vegetation abundance relationship for urban heat island studies. *Remote sensing of Environment*. **89(4)**: 467-483.

Woldegabriel, G., Aronson, J. L. and Walter, R. C. (1990). Geology, geochronology, and rift basin development in the central sector of the Main Ethiopia Rift. *Geological Society of America Bulletin*. **102**: 439-458.

Yu, Y., Tarpley, D., Privette, J. L., Goldberg, M. D., Raja, M. K. R. V., Vinnikov, K. Y. and Xu, H. (2009). Developing algorithm for operational GOES-R land surface temperature product. *IEEE Transactions on Geoscience and Remote Sensing*. **47**: 936-951.

Appendices

Appendix A: Geological Map of study area in scale 1: 20, 000. Source: Geological Survey of Ethiopa.

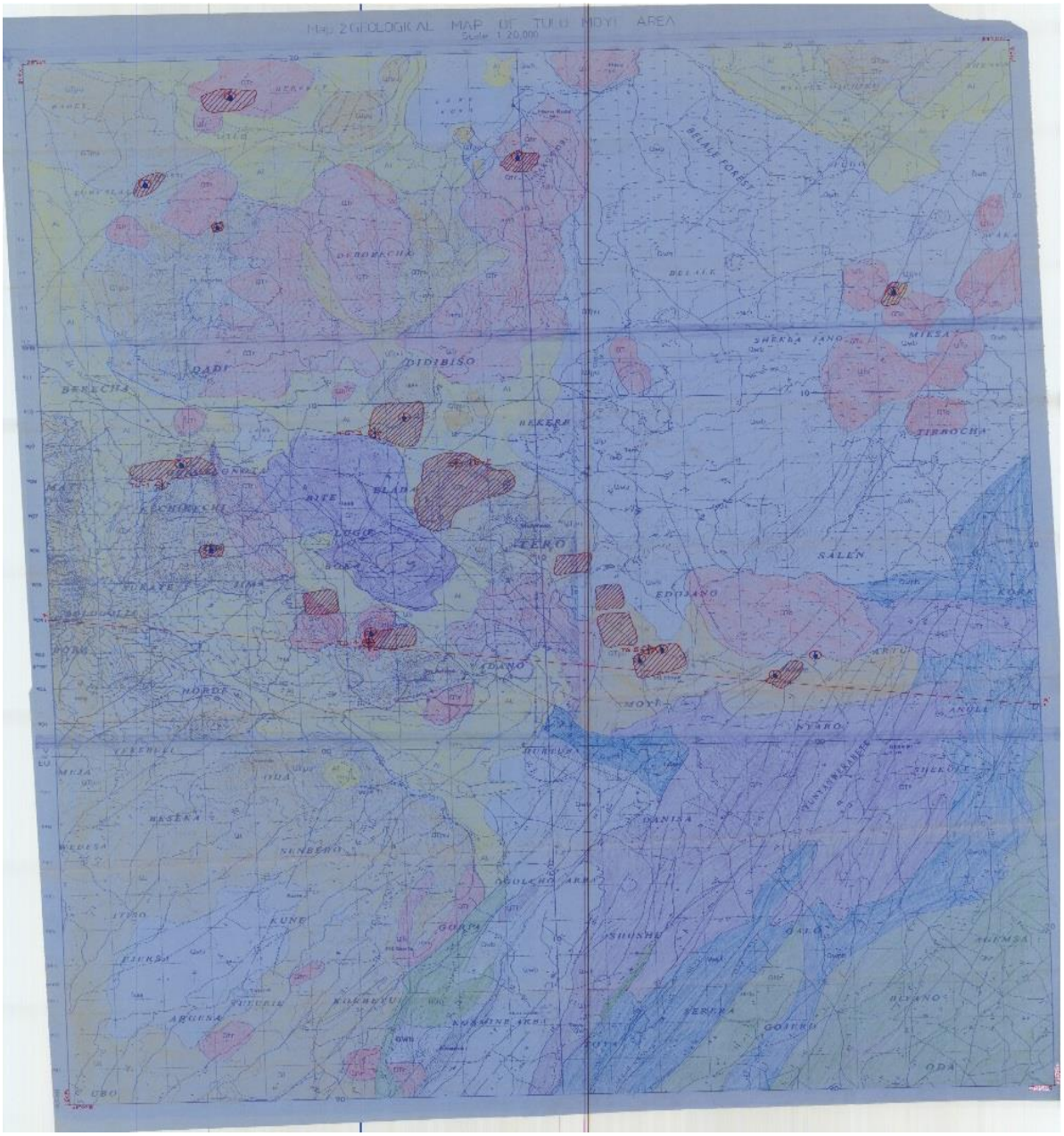

Appendix B: Geological Map of study area in scale 1: 50, 000. Source: Geological Survey of Ethiopia.

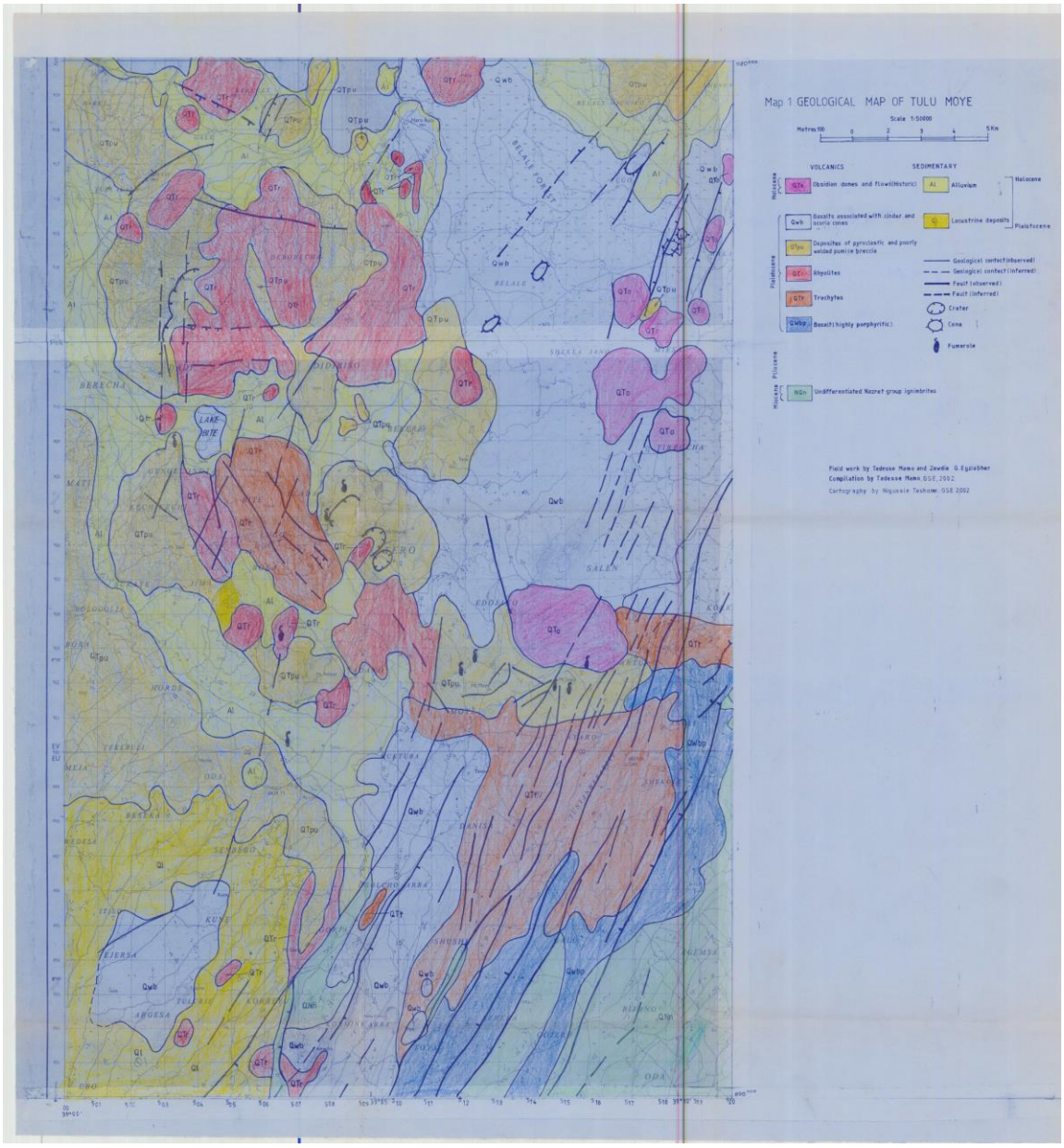

Appendix C: Collected GPS point at hydrothermal Manifestation area for validation.

ID	E	N	Z
1	517709	912896	1772
2	510158	914699	1792
3	504799	915527	1802
4	502607	915673	1819
5	502510	907879	1800
6	503338	905394	1989
7	505433	903787	1824
8	506797	902666	1804
9	507333	908951	1781
10	508794	906856	1968
11	510694	905005	1988
12	514932	901838	2218
13	511619	904128	2044
14	511668	902959	2038
15	512691	902179	2121

Appendix C: Raw Landsat 8 data with path 168 and row 054

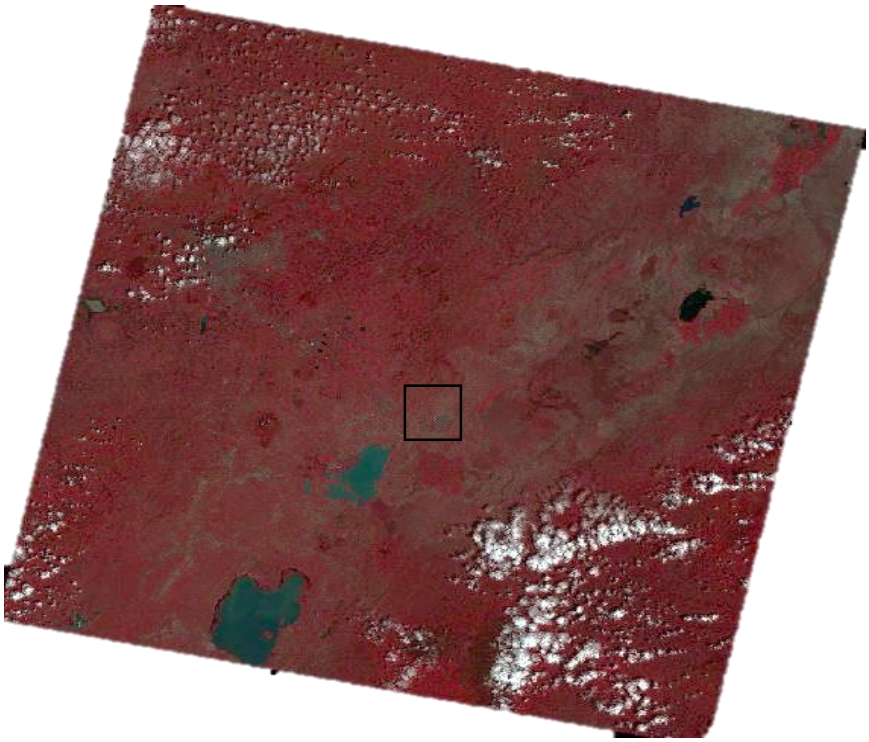

Appendix D: Atmospheric result of band 4

```
*******************************************************************************
*                        atmospheric correction result                        *
*                        -----------------------------                        *
*       input apparent reflectance             :    0.100                     *
*       measured radiance [w/m2/sr/mic]        :   44.288                     *
*       atmospherically corrected reflectance                                 *
*       Lambertian case :       0.08947                                       *
*       BRDF       case :       0.08947                                       *
*       coefficients xa xb xc                  :  0.00266  0.02783  0.07723   *
*       y=xa*(measured radiance)-xb;  acr=y/(1.+xc*y)                         *
*******************************************************************************
```

Appendix E: Atmospheric result of band 5

```
*******************************************************************************
*                        atmospheric correction result                        *
*                        -----------------------------                        *
*       input apparent reflectance             :    0.100                     *
*       measured radiance [w/m2/sr/mic]        :   27.554                     *
*       atmospherically corrected reflectance                                 *
*       Lambertian case :       0.09547                                       *
*       BRDF       case :       0.09547                                       *
*       coefficients xa xb xc                  :  0.00393  0.01242  0.04648   *
*       y=xa*(measured radiance)-xb;  acr=y/(1.+xc*y)                         *
*******************************************************************************
```

Declaration

I, the undersigned, declare that this thesis entitled "DETECTION OF GEOTHERMAL ANOMALIES USING LANDSAT 8 THERMAL INFRARED DATA IN TULU MOYE GEOTHERMAL PROSPECT, MAIN ETHIOPIA RIFT" is my original work and has not been presented for a degree in any other university and that all sources of materials used for this thesis have been interestingly acknowledged.

Yosef Mengistu Darge

Signature _____

Date _____

Addis Ababa University

Addis Ababa

June, 2016